Energy absorption in Ni–Mn–Ga/ polymer composites

by

Jorge Feuchtwanger

Submitted to the Department of Materials Science and Engineering
in partial fulfillment of the requirements for the degree of

Doctor of Philosophy in Materials Science

at the

MASSACHUSETTS INSTITUTE OF TECHNOLOGY

February 2006

Author .....
Department of Materials Science and Engineering
October 13, 2005

Certified by .....
Samuel M. Allen
POSCO Professor of Physical Metallurgy
Thesis Supervisor

Certified by .....
Robert C. O'Handley
Senior Research Scientist
Thesis Supervisor

Accepted by .....
Gerbrand Ceder
R. P. Simmons Professor of Materials Science and Engineering
Chairman, Department Committee on Graduate Students

Energy absorption in Ni–Mn–Ga/ polymer composites

by

Jorge Feuchtwanger

Submitted to the Department of Materials Science and Engineering
on October 13, 2005, in partial fulfillment of the
requirements for the degree of
Doctor of Philosophy in Materials Science

Abstract

In recent years Ni–Mn–Ga has attracted considerable attention as a new kind of actuator material. Off-stoichiometric single crystals of Ni_2MnGa can regularly exhibit 6% strain in tetragonal martensites and orthorhombic martensites have shown up to 10% strain when subjected to a magnetic field. These crystals are brittle and the production of single crystals can be quite costly. Terfenol-D, a commercially available giant-magnetostrictive material, suffers from some of the same drawbacks. It was found that composite materials made from Terfenol-D particles in a polymeric matrix could solve the issue of the brittleness while retaining a large fraction of the strain output of the alloy. At first glance a similar approach could be used to solve the brittleness issue of Ni–Mn–Ga, but the low blocking force of these alloys reduces the chances of achieving a Ni–Mn–Ga/polymer composite actuator. However, the stress-strain loops for Ni–Mn–Ga show a large mechanical hysteresis. This ability to dissipate energy makes this alloys very desirable for damping applications, and by putting particles of Ni–Mn–Ga in a composite, their brittleness becomes less of an issue.

It is shown that by curing Ni–Mn–Ga/polymer composites under a magnetic field it is possible to align the particles in chains and to orient them so they will respond to a uniaxial load. The magnetic measurements show that there are twin boundaries in the particles that can be moved by an external stress. Stress-induced twin boundary motion in the particles is confirmed more directly by x-ray diffraction measurements, transmission electron microscope micrographs, and scanning electron microscope micrographs. Finally we demonstrate the ability of the Ni–Mn–Ga/polymer composites to dissipate mechanical energy when subjected to cyclic loads. The Ni–Mn–Ga/polymer composites can dissipate more than 70% of the energy they are given in every cycle, while pure polymer, Fe-filled and Terfenol-filled control samples dissipate less than 50% of the input energy in every cycle. The additional loss in these composites is shown to be due to the motion of twin boundaries. Simple numerical models reproduce the cyclic stress-strain behavior of the composites and explain non-conventional features observed in the Ni–Mn–Ga composites.

Thesis Supervisor: Samuel M. Allen
Title: POSCO Professor of Physical Metallurgy

Thesis Supervisor: Robert C. O'Handley
Title: Senior Research Scientist

Acknowledgments

First of all I have to thank my parents, it was always important for them to provide me with a good education, because they knew it was the only thing they could give me that I would always have. It is thanks to them I made it this far, and for that I will always be thankful to them.

I owe a lot of gratitude to my two advisors, Sam Allen and Bob O'Handley. It was truly a pleasure working with them. I learned a lot from the both of them, especially because one's advice tended to complement the others.

David Bono help getting things to work made my research a lot simpler, but he was also a friend and that was probably more valuable.

I have to thank the people in the group, both past and present for helping with this work, but more than that for being like a family in the lab. Marc Richard helped with all the XRD measurements; I also have to thank him for making the trip to china more bearable, and made the medallion casting possible. I was going to thank Brad Peterson for helping me with my experiments and the EDM every time it broke, but he asked to be acknowledged for asking me to put him in the acknowledgements. Josh Chambers was very helpful with some of the FE simulations and also for never dropping my experiment. Zil Lyons (now Zil Friend) for the discussions about things other than research and for the time spend studying for the qualifying exam. Miguel Marioni and Chris Henry for showing me how to wok in the lab when I arrived. Ratchatee Techapiesancharoenkij and Jesse Simon should also be acknowledged. Prof. Manu Barandiaran for the help during his stay here. Prof Steve Hall from Aero-Astro for his suggestions.

The UROP students that helped to collect some of the data have to be thanked. They include Samantha Bennet and Jim Pacella but I have to specially thank Kelli Grifin because her work made up more than one of the chapters in this thesis.

I would not have been able to do this without my friends. Juan A. Gonzales was with me in undergrad, we worked in the same lab for our undergrad Theses and came here at the same time I did. Jorge Vieyra was with me in undergrad also and then came here later. I met Jorge Carretero, Raymundo Arroyave, Jorge Martinez, Coddy Friessen, Garry

Maskaley and Karlene Maskaley here, and now they are good friends of mine.

The people in Caroline Ross' group where always helpful, but I have to particularly thank Fernado Castaño for being a good friend (and also for helping to relive the clutter in the lab).

While Debbie Morecroft is also a part of the Ross she deserves a special thank you. I have to thank her for being a good friend, for proofreading most of this thesis, for all the coffee and for everything else that made writing this thesis more bearable.

There are other people I have met at MIT that made my time here a lot more fun, Toby Bashaw is one of the greatest people I have met, and he always made fun things like casting a lot more fun. Fred Cote from the Edgerton center machine shop was a great person to talk to and going to the shop was always a pleasure because he was there to talk to and to guide everyone. Coach Will Hart for putting up with me for too many PE quarters.

I have to thank the rest of my committee, Prof. Robert Rose and Prof. Yet-Ming Chiang for their suggestions that helped make this a better thesis.

I would also like to thank the Office of Naval Research's MURI grant No. N0014-01-0758, for the financial support of this work.

I know I left someone out, and I apologize for that, but thanks for your help.

Contents

1 Introduction **19**

1.1 Ferromagnetic Shape Memory Alloys 19

1.1.1 Physical Properties 21

1.1.2 Actuation 22

1.2 Composites 25

1.2.1 Terfenol-D composites 25

1.2.2 Ni–Mn–Ga composites 26

1.3 Viscoelastic Materials (matrix) 27

1.3.1 Polyurethanes 27

1.3.2 Static mechanical Loading 28

1.3.3 Cyclic loading 29

1.4 Damping 30

1.4.1 Damping Mechanisms 30

1.4.2 Damping relations 32

1.4.3 Ni–Mn–Ga 32

1.4.4 Magnetic Materials 33

1.5 Spark erosion 35

1.6 Thesis layout 36

2 Torque measurements **39**

2.1 Torque magnetometry 39

2.2 Sample preparation 40

2.3 Experimental setup 41

2.4 Results . . . 42
2.5 Discussion . . . 46
2.6 Conclusions . . . 53

3 Vibrating Sample Magnetometry Measurements 55
3.1 Vibrating sample magnetometry . . . 55
3.2 Sample preparation . . . 57
3.3 Experimental details . . . 58
3.3.1 Magnetization versus temperature . . . 58
3.3.2 Magnetization versus field . . . 58
3.4 Results . . . 59
3.4.1 Magnetization versus temperature . . . 59
3.4.2 Magnetization versus field . . . 60
3.5 Discussion . . . 64
3.5.1 Magnetization versus temperature . . . 64
3.5.2 Magnetization versus field . . . 66
3.6 Conclusions . . . 68

4 Direct observations 71
4.1 Experimental techniques and sample preparation . . . 71
4.1.1 Powder x-ray diffraction . . . 71
4.1.2 Scanning electron microscopy . . . 72
4.1.3 Transmission electron microscopy . . . 73
4.2 Results . . . 73
4.2.1 X-ray diffraction . . . 73
4.2.2 Scanning electron microscopy . . . 76
4.2.3 High-resolution transmission electron microscopy . . . 79
4.3 Discussion . . . 80
4.3.1 X-ray diffraction . . . 80
4.3.2 Scanning electron microscopy . . . 81
4.3.3 High-resolution transmission electron microscopy . . . 82

4.4 Conclusions 82

5 Mechanical measurements **85**

5.1 Cyclic testing 85

5.1.1 Custom tester 86

5.1.2 Sample grips 87

5.2 Sample preparation 89

5.3 Experimental setup 90

5.4 Results 90

5.4.1 Room-temperature measurements 90

5.4.2 Temperature dependent measurements. 94

5.5 Discussion 97

5.5.1 Room-temperature measurements 97

5.5.2 Temperature dependent measurements 99

5.6 Conclusions 100

6 Modeling **103**

6.1 Description 103

6.1.1 Finite-element modeling 103

6.1.2 Cyclic stress-strain modeling 104

6.2 Method 104

6.2.1 Finite-element modeling 104

6.2.2 Cyclic stress-strain modeling 106

6.3 Results 107

6.3.1 Finite-element modeling 107

6.3.2 Cyclic stress-strain modeling 109

6.4 Discussion 112

6.4.1 Finite-element modeling 112

6.4.2 Cyclic stress-strain modeling 113

6.5 Conclusions 114

7 Engineering Issues **117**

7.1 Heating 117

7.2 Expected frequency dependence 120

7.3 Damping material selection 123

8 Summary, conclusions and future work **125**

8.1 Summary 125

8.2 Conclusions 128

8.3 Future work 130

A Loss ratio calculation script **133**

B Loss ratio calculation script **135**

List of Figures

1-1 Arrangement of the variants after sliping and twining. 21

1-2 Schematic of the a) cubic (showing how the tetragonal structure is redefined by a 45° rotation) and b) tetragonal structure of Ni–Mn–Ga, (Figures courtesy of Marc Richard). 22

1-3 Schematic stress vs. strain plot for martensitic Ni–Mn–Ga. 23

1-4 Cyclic strain field loops for a single crystal of Ni–Mn–Ga under a 1 Hz magnetic drive, from C.P. Henrry [1]. 24

1-5 Modulus and loss factor as a function of temperature for butyl rubber, form Harris' Shock and Vibration Handbook [2]. 31

1-6 Stiffness-loss map showing different materials, reproduced from Y.C. Wang et al. Materials Science and Engineering A [3]. 34

2-1 Photograph of the torque magnetometer used with key components labeled. 41

2-2 Schematic of a torque magnetometer. 43

2-3 Peak-to-peak torque as a function of the applied strain in two different directions for large strains on 25% volume FSMA in Kalex polyurethane. . . 44

2-4 Peak-to-peak torque as a function of the applied strain on composites based on two matrices having different stifnesses. 45

2-5 Effect of the volume fraction on the peak-to-peak torque as a function of strain for (sample N) 24% by volume of FSMA in Lord 7540 and (sample O) 40% of FSMA in Lord 7540 46

2-6 Effect on the maximum peak to peak torque of repeated strain-and-reset cycles for 25 % in-plane strain. 47

2-7 Maximum peak-to-peak torque for (sample G2) 24 % Ni–Mn–Ga in Lord polyurethane and (sample J) 24 % Terfenol-D powder in Lord Polyurethane. 48

2-8 Schematic of the resulting torque for (a) a particle with the main variant normal to the xy-plane, and (b) a particle with the main variant in the xy-plane 50

3-1 Schematic of a vibrating sample magnetometer. 56

3-2 Magnetization vs. temperature for Ni–Mn–Ga spark eroded in liquid Ar, measured at 500 Oe. 60

3-3 Magnetization vs. field for three different in-plane strains for Ni–Mn–Ga in Lord 7540A/B polyurethane. 62

3-4 Magnetization vs. field for the as-cast and two different in-plane strains for Terfenol-D powder in Lord 7540A/B polyurethane. 63

3-5 Magnetization vs. field for the as-cast and 26.4 % in-plane strain for Ni–Mn–Ga powder in Lord 7540A/B polyurethane up to 10 kOe. 64

3-6 Magnetization vs. field for the as-cast and out-of-plane reset after being strained in-plane for Ni–Mn–Ga powder in Lord 7540A/B polyurethane. . . 65

3-7 Magnetization vs. field for the as-cast, in-plane strained and after being heated to 100° C for Ni–Mn–Ga powder in Lord 7540A/B polyurethane. . . 66

4-1 X-ray diffraction scans for Ni–Mn–Ga randomly sprinkled particles on epoxy with no magnetic field while curing, spark eroded in (a) liquid argon and (b) liquid nitrogen 74

4-2 X-ray diffraction scans for (a) Ni–Mn–Ga particles spark eroded in liquid argon sprinkled on a glass slide with no field applied and (b) 40 vol % FSMA spark eroded in liquid argon oriented with an out-of-plane field in Lord 7540 A/B. 75

4-3 Schematic of the composite sample (rectangle) indicating the direction of the particle-chains and the incident x-rays. 76

4-4 X-ray diffraction scans for (a) a 40 vol. % Ni–Mn–Ga spark eroded in liquid Argon in Lord 7540 A/B polyurethane as cast (no stain applied cured with an in-plane field and (b) the same composite after 12% out-of-plane compressive strain. 77

4-5 Schematic of the composite sample (rectangle) indicating the direction of the particle-chains, the incident x-rays, and the stress applied. 77

4-6 Scanning electron microscope micrograph of Ni–Mn–Ga spark eroded in liquid nitrogen. 78

4-7 Scanning electron microscope micrograph of a Ni–Mn–Ga polymer composite as-cast cured with an out-of-plane field (a) and after being stressed compressibly out-of-plane (b). 78

4-8 High-resolution transmission electron micrograph of Ni–Mn–Ga spark eroded in liquid Argon. Dark lines have been superimposed the image to emphasize the boundaries. 79

5-1 Schematic of the mechanical tester used. 86

5-2 Finite-element simulation of the clamping force on the mechanical testing samples. 88

5-3 Schematic of the sample cast into the aluminium end caps. 89

5-4 Cyclic Stress versus Strain for pure lord 7540 A/B polyurethane at 1 Hz for two different stress levels. 91

5-5 Cyclic Stress versus Strain for 20 vol. % FSMA in lord 7540 A/B polyurethane at 1 Hz for two different stress levels. 92

5-6 Stress vs. time and Strain vs. time plots for the large stress amplitude trace in Figure 5-5. 93

5-7 Cyclic Stress versus Strain for 20 vol. % Fe powder in lord 7540 A/B polyurethane at 1 Hz. 94

5-8 Loss ratio as a function of temperature for a Lord 7540 A/B sample and 20 vol. % FSMA in Lord 7540 A/B. 95

5-9 Loss ratio as a function of stress for a Lord 7540 A/B sample and 20 vol. % FSMA in Lord 7540 A/B at 22°C. 96

5-10 Loss ratio as a function of stress for a Lord 7540 A/B sample and 20 vol. % FSMA in Lord 7540 A/B at 47°C. 97

5-11 Differential scanning calorimeter scan for a pure Lord 7540 A/B sample and 20 vol. % FSMA in Lord 7540 A/B on heating. 98

6-1 Two-dimensional projection for a composite with 25 vol % filler evenly distributed in the matrix. 106

6-2 Two-dimensional projection for a composite with 25 vol % filler aligned in chains in the matrix. 106

6-3 Simulation of the xy shear stress in a composite with 25 vol. % filler evenly distributed subjected to a) 3 % uniaxial compressive strain (strain along the vertical (y) direction), b) 3 % uniaxial tensile strain (strain along the vertical (y) direction). Note the similarity in stress states for both cases. . . 108

6-4 Simulation of the xy shear stress in a composite with 25 vol. % filler aligned in chains subjected to a) 3 % uniaxial compressive strain (strain along the vertical (y) direction), b) 3 % uniaxial tensile strain (strain along the vertical (y) direction). note reversal of stress directions between the two cases. 109

6-5 Simulated stress-strain loops for the constant-stress approximation for (a) the polymer matrix (b) the FSMA and (c) the convolution of (a) and (b) at 25 vol. % FSMA. 111

6-6 Simulated stress-strain loops for the composite under the constant-stress approximation for three maximum stress amplitudes: (a) 2 MPa (b) 2.5 MPa and (c) 3 MPa. 112

6-7 Simulated stress-strain loops for the composite under the constant strain approximation for three maximum strain amplitudes: (a) 0.0005 (b) 0.03 and (c) 0.061. 113

7-1 Calculated temperature increase (ΔT) for 1 Hz, 10 Hz, 30 Hz and 60 Hz. . 119

7-2 Calculated temperature increase (ΔT) at 60 Hz for the particles perfectly insulated, particles with a thin insulation layer transfering heat to the outside with a constant gradient and particles transfering heat to the matrix, but with no heat transfer to the outside 121
7-3 Schematic of the expected loss as a function of frequency for the FSMA, polymer matrix and the composite. 122
7-4 Stress distribution around a circular hole of radius one, subjected to an uniaxial tensile load. 123

List of Tables

3.1 Transformation and Curie Temperatures for the alloys used in the composites. 60

3.2 Composition in atomic % for the alloys used in the composites. 61

5.1 Maximum stress, loss ratio and $\tan\delta$ for the two control samples and the FSMA loaded sample. 95

Chapter 1

Introduction

1.1 Ferromagnetic Shape Memory Alloys

Shape memory alloys (SMAs) are a subset of a class of materials known as "active" or "smart" materials. These materials respond to an external stimulus by changing their dimensions. SMAs strain (3–8%) when the material is heated above a specific temperature. The change in dimensions in these materials is due to a diffusionless phase transformation from a higher symmetry, high-temperature phase to a lower symmetry, low-temperature phase. In addition to the large strain, they also exhibit a "shape memory" effect. These materials can sustain large deformations in the low temperature phase, but unlike conventional metals, if they are heated into the high temperature phase they recover their original shape.

When these materials transform from the high temperature phase into the low temperature phase, the transformation stresses are accommodated by twinning rather than by slip. Figure 1-1 shows the difference between deformation by twinning and slip. In slip (upper half of Figure 1-1) when the material is deformed inelastically, dislocations glide to the edges of the crystal causing a permanent deformation. When a material deforms by twinning, *variants* are formed, these are regions in the crystal where the unique axis of the crystal points in a specific direction. In adjacent variants the unique axis is rotated by an angle related to the difference in length between the longer and shorter axes in the crystal. The planes that separate adjacent variants are called twin-boundaries, and the crystal structure of the variant on one side of the twin-boundaries is the mirror image of the

crystal structure of the adjacent variant. The lower part of Figure 1-1 shows a twinned structure, two different variants at the left and right, each shaded in a different color. The application of a shear stress transforms the single variant arrangement on the left first to a twinned structure in the middle, then to a different single variant arrangement on the right. This mode of deformation is called pseudo-plasticity, becauseif the stress is removed, the defrormationremains, but if a stress is applied in the opposite direction it can restore the material to its initial state. In twinning, even after large deformations, all atoms are connected to the same atoms they were connected to before the crystal was deformed. When the deformed material is heated into the higher symmetry phase the twins disappear and the original shape of the material is restored. In a material that has been "trained", by cycling it repeatedly from one phase to the other while constrained, defects are created that cause twin-boundaries to form in the same place. By forcing the twin-boundaries reform in the same places, the same shape can be obtained every time the material is cooled into the low temperature phase, giving the material its "shape memory".This is usually called "two way shape memmory" [4, 5].

Ferromagnetic shape memory alloys (FSMAs) are a subset of SMAs that are also ferromagnetic. They were studied because it was thought these materials could be used as magneto-elastic materials. It was thought that if they were held at a constant temperature, near the phase transformation temperature, a magnetic field could be used to shift the transition temperature, causing them to transform. This would achieve a large change in their dimensions without having to change the temperature. Since the rate of actuation of bulk SMA actuators is limited by the heat transfer rate of the alloys, it is generally limited to a few Hertz . By using a magnetic field to shift the transformation temperature, the rate of actuation could be increased, because the rate at which a magnetic field can be switched is greater than the rate at which the alloys transfer heat. Unfortunately it was found that fields of several Teslas were needed to shift the transformation temperature a single degree Kelvin, making this mode of actuation impractical. However, in 1996 a strain comparable to the best magneto-elastic materials was observed in a single crystal of off-stoichiometric Ni_2MnGa, for a field of less than one Tesla [6]. The strain output reported in these alloys continued to increase, and by 2001 strains of up to 6% were reported in tetragonal

single crystals of Ni–Mn–Ga [7, 8, 9, 10, 11, 12]. Later 10% magnetically induced strain was reported in orthorhombic Ni–Mn–Ga [13]. This work also found that the mechanism responsible for the large strains was the magnetic field driven motion of twin boundaries.

The large strains observed in FSMAs are accompanied by a low blocking stress $\sim$2 MPa [14]. The strain exhibited by Ni–Mn–Ga is an order of magnitude larger than the strain shown by the best piezoelectric ceramics ($\sim$0.19%) [15], and while the stress output of the FSMAs is lower, their energy densities are comparable. This makes FSMAs attractive replacements for actuation applications where high strain and low force are required since no mechanical strain amplifiers would be needed [16].

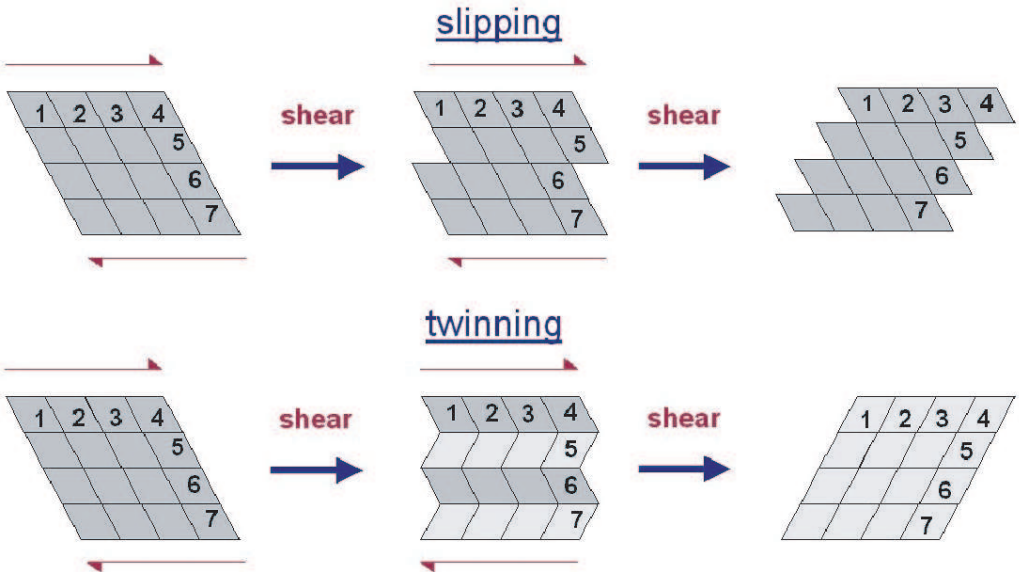

Figure 1-1: Arrangement of the variants after sliping and twining.

1.1.1 Physical Properties

Ni_2MnGa is a Heusler type alloy below 1071 K [17, 18]. The chemically ordered austenite phase of Ni_2MnGa has a point group $Fm\bar{3}m$ (Figure 1-2 a). The lattice constant a_0 in the austenite phase at room temperature is 0.582 nm. On cooling, the cubic phase distorts by a diffusionless martensitic transformation to a lower symmetry martensite phase which can be tetragonal, orthorhombic, or monoclinic [19, 20]. The stoichiometric martensitic phase has point group $I4/mmm$ (Figure 1-2 b), but the more common off-stoichiometry

martensites have more complex structures. The tetragonally distorted martensite has lattice constants $a = b = 0.592$ nm, $c = 0.557$ nm [21]. The maximum strain achievable by twinning is given by $1 - \frac{c}{a} \cong 0.06$. As the material transforms from the cubic austenite to the tetragonal martensite one of the a_0-axes transforms in to the c-axis and the other two transform into the a-axes.

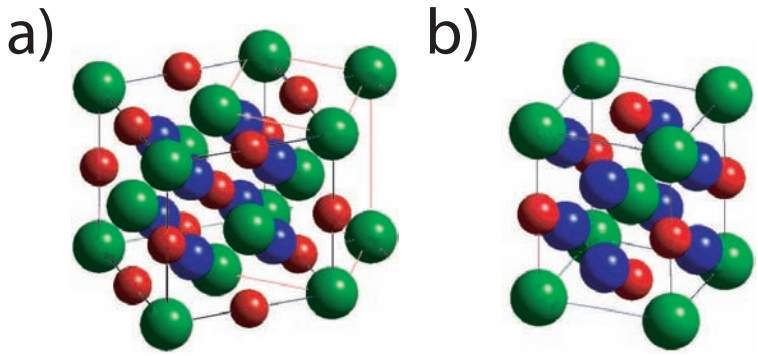

Figure 1-2: Schematic of the a) cubic (showing how the tetragonal structure is re-defined by a 45° rotation) and b) tetragonal structure of Ni–Mn–Ga, (Figures courtesy of Marc Richard).

The mechanical properties of FSMAs in the martensitic (Figure 1-3) state are similar to those of SMAs. When subjected to compression they first exhibit a modulus C_0 of about 10^9Pa. At a critical stress σ_t the twin boundaries become mobile and the material exhibits an apparent modulus C_t (10^6 Pa) lower than C_0. Once all the twin boundaries have been swept and the material is in a new single-variant state, the modulus stiffens again to its initial value of C_0. When the load is removed the material only recovers the elastic strain. A stress normal to the initial compressive load would return the crystal to the original variant state [22]. Figure 1-3 shows that the load and unload paths do not superpose if the stress on the alloy is large enough to change the variant structure in the crystal. This anelastic deformation that can be recovered is the source of the large mechanical hysteresis observed in these alloys.

1.1.2 Actuation

In Ni–Mn–Ga, twin-boundary formation accommodates the stress generated by the diffusionless transformation from the high-symmetry, high-temperature austenitic phase to the low-

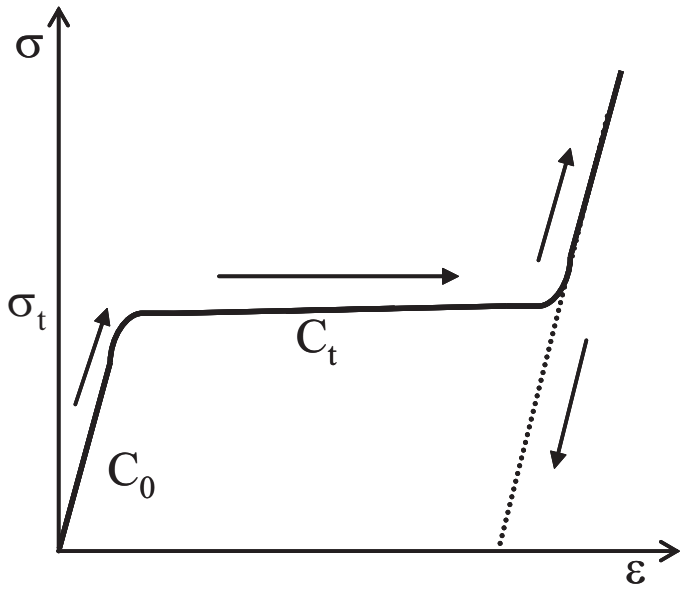

Figure 1-3: Schematic stress vs. strain plot for martensitic Ni–Mn–Ga.

temperature, lower-symmetry martensite. The magnetic moment is strongly coupled to the c-axis of the martensite by the high magnetocrystalline anisotropy. When a magnetic field is applied parallel to the easy axis of magnetization of one of the variants, the energy of the variants with the easy axis parallel to the field will be different than for the variants with the field normal to easy axis. This energy difference provides the driving force for the motion of twin boundaries. If the driving force is larger than the energy needed to move twin boundaries the field will move the twin boundaries, growing the variant with the c-axis parallel to the field at the expense of the other. The maximum field that can be applied to drive twin boundaries is limited by the magnetocrystalline anisotropy of the alloy. A field larger than the anisotropy field will cause the moments to break free from the easy axis of magnetization. If the moments rotate into the field the driving force for twin motion disappears [23, 24]. The macroscopically observed strain is the result of the variants with the c-axis parallel to the field growing at the expense of the other variants. As one variant grows at the expense of the other, the number of the longer a-axes normal to the drive field increases resulting in a net increase in the crystal along that direction.

When used as actuators, single crystals of Ni–Mn–Ga have to start in a single variant configuration with the c-axis along the load path to achieve the full strain. The drive field is

applied normal to the load path. In cyclic actuation, the field is varied as a function of time and a load on the crystal re-sets it to the starting configuration every time the field value crosses zero. This results in an actuation frequency that is double that of the drive field. Figure 1-4 shows a set of strain-field loops for different pre-loads on the crystal. When the external stress is too low, the crystal extends the first time it is subjected to a field, but the stress is not large enough to fully reset the crystal, resulting in a small cyclic strain. As the stress is increased a larger fraction of the crystal is reset, and the cyclic strain output increases. When the external stress is increased past a certain value, the amount of energy the magnetic field can provide to the systems is less than the work needed to push against the external load and the crystals cannot fully extend, resulting in a decrease in the strain output of the system.

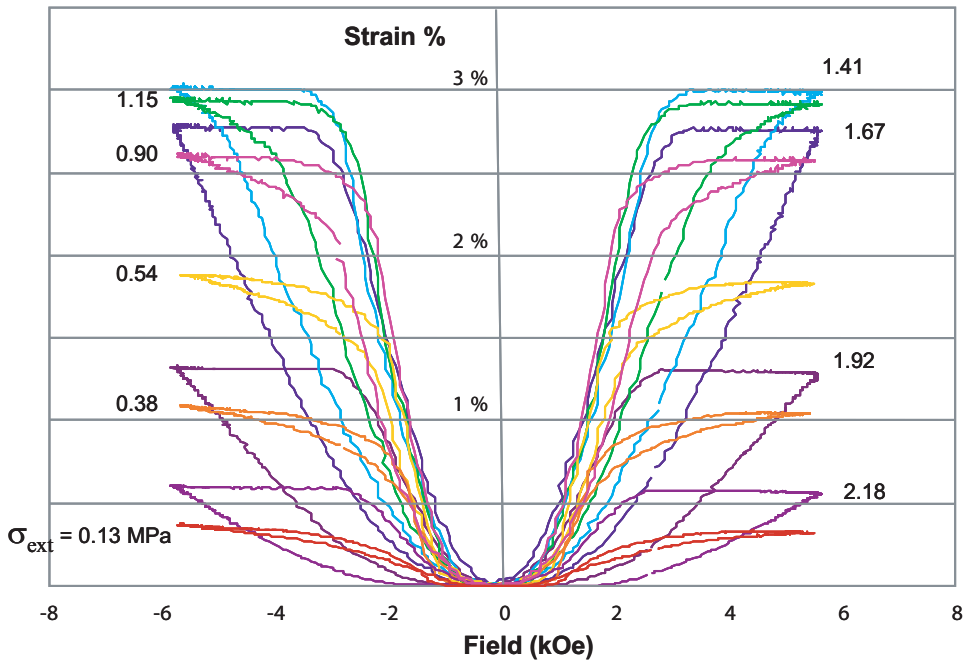

Figure 1-4: Cyclic strain field loops for a single crystal of Ni–Mn–Ga under a 1 Hz magnetic drive, from C.P. Henrry [1].

1.2 Composites

1.2.1 Terfenol-D composites

Terfenol-D (terbium iron Naval Ordinance Lab-dysprosium), a giant-magnetostrictive alloy [25] which is quite brittle, had been proposed as a damping material [26, 27]. Carman's group at the University of California, Los Angeles had developed composite materials that showed magneto-mechanical properties very similar to the single crystals of Terfenol-D, using resin composites loaded with 10–30 vol. % of the active material [28]. By putting the active material in the polymeric matrix the brittleness of Terfenol-D became less of an issue under tensile loading.

Composites made from Terfenol-D powder in a polymeric matrix can exhibit magnetic field induced strains that are a sizable fraction of the strain observed in single crystals. Composites containing 30 vol % of Terfenol-D powder showed field induced strains of about 1000 ppm [28]. The maximum observed strain in single crystals is about 2000 ppm [25]. In recent unpublished work, 50 vol. % Terfenol-D/resin composites have shown strains of up to 1600 ppm and have responded to drive frequencies as high as 100 kHz.

These composites were made by mixing the Terfenol-D with the uncured polymeric matrix. The resulting slurry was loaded into a mold which was then placed in a vacuum furnace fitted with a magnet. A vacuum is drawn around the sample to de-gas the mixture and a field is applied to align the particles in the matrix. The slurry is then heated up to cure the epoxy matrix. The procedure used in making the Ni–Mn–Ga composites presented in this thesis was motivated by the procedure for making Terfenol-D composites.

The application of the field while curing the slurry aligns the particles in chains, giving rise to a pseudo 3:1 composite. In this nomenclature the first number represents the connectivity of the matrix, and the second number is the connectivity of the filler. connectivity means that a point at one end of the sample is connected to to an other point at the opposite end of the sample by an uninterrupted path of material. In a 3:1 composite the matrix fully surrounds the filler and it forms a 3-dimensional structure, the filler is composed of fibers that run the length of the composite and are 1 dimensional structures. Formally these composites are 3:0, since the particles are 0-dimensional structures, but since they are aligned in

chains under compression they behave like chains and mimic a 3:1 composite. Laminated composites in this nomenclature would be called 2:2 composites since both the matrix and the filler form structures are connected in 2-dimensions.

1.2.2 Ni–Mn–Ga composites

In recent years some work has been done on FSMA loaded composites. Hosoda prepared and characterized composites of Ni–Mn–Ga in an epoxy matrix. The composites exhibited thermo-elastic shape memory effect. Phase-transition-related strains in the composite as high as 0.1% were observed [29]. The composites used by Hosoda were made by crushing polycrystals of Ni–Mn–Ga, to obtain particles small enough to be single crystals. The composites were made by mixing the FSMA particles with an epoxy and allowing it to cure under a magnetic field of undisclosed magnitude at 353 K for 130-170 ks [30]. It is reported that the size of the particles used in the composites affected their performance. This work focused on the use of FSMA composites as thermally driven active materials and in early publications the composites reported were not cured under an applied magnetic field [31].

Using FSMAs as composite actuators did not seem feasible, because for FSMA composites to work as actuators the c-axes would have to orient parallel to the curing field and all the twin planes in the particles would have to be parallel to each other, so that an external stress could get all the particles to strain at the same time. The alignment of the c-axes is not difficult since it is the easy axis of magnetization [14], and the magnetic moment is strongly coupled to it. Getting the twin planes to align parallel to each other on the other hand is a difficult task, that might not be possible. Additionally, the field induced strain is blocked by a stress as small as a few MPa; the stress output from the FSMA would mostly be used to deform the matrix, leaving an even smaller blocking stress left over for the composite actuator.

On the other hand, using the FSMA particles in a composite for *damping* showed more promise. The fiber texture that would most likely result from curing the composites under a field would orient the particles so they would respond to a uniaxial mechanical load parallel to the field applied while curing. The large hysteretic loss in the stress-strain loops should

make them good dampers, and the brittleness of Ni–Mn–Ga would be alleviated since the matrix would take most of the load under tension. The composites also have the advantage that the particles can be made from crushing polycrystals or from atomized or spark eroded powders, reducing the cost relative to using single crystals. The low volume fraction of metal in the composites would also bring the cost down.

1.3 Viscoelastic Materials (matrix)

A few basic criteria were important to keep in mind in the initial search for the matrix material. These included the following:

- The matrix should cure at or near room temperature.
- As low a volume change as possible at curing was desired.
- The matrix should be able to sustain large deformations reversibly (at least 10%) .
- The matrix should have a fairly low modulus, close to the modulus of the FSMA when twin-boundaries are mobile.

1.3.1 Polyurethanes

Polyurethanes meet all the characteristics described above: they can be about as stiff as a hard rubber, many can be cured at room temperature with a zero volume change and they can sustain large strains reversibly. Additionally polyurethanes are known for having excellent wear and tear properties, oil resistance and toughness [32]. All these properties made polyurethanes an attractive class of matrix materials. The urethane group is the result of the reaction of an isocyanate and an alcohol group.

Polyurethanes were discovered in the 1930's mostly as the result of research looking to find artificial substitutes for natural rubber. This name is given to a large variety of solid polymers, that have many similar general characteristics, but that can have a range of properties depending on the specific composition of the monomers. [33, 32]. The name

polyurethane comes from the chemical group urethane, which links the monomers that form the polymer.

Work on developing a chemical composition to exactly match the mechanical properties required was outside the scope of this thesis, so it was decided to use a commercially available formulation as the matrix material.

1.3.2 Static mechanical Loading

Solids that are subject to a load respond by changing their dimensions. When the deformation that results is small, the strain that results from the applied stress can be modeled linearly in the simplest way by Hooke's law:

$$\sigma = E\epsilon \tag{1.1}$$

where σ is the applied stress, E is Young's modulus, and ϵ is the resulting strain. Stress and strain are assumed to be in phase and any variation in the applied stress results instantaneously in a proportional variation in the strain. For stiff materials like metals and ceramics this is a good approximation, but for other materials like rubbers or other viscoelastic materials the response is out of phase and the stress-strain phase shift can be quite dramatic. However, this model fails to take into account any non-linear response (the modulus (E) may not be constant) or the time dependence of stress. Simply adding a viscous drag term to equation 1.1 accounts for the phase shift in the strain response, as seen in

$$\sigma(t) = E\epsilon + \eta\frac{d\epsilon}{dt} \tag{1.2}$$

In polymers this extra term accounts for the conformational changes of the polymer molecules in the solids under an applied stress [34]. This simple addition to the model allows it to fit a variety of experimental data on viscoelastic materials well.

1.3.3 Cyclic loading

When viscoelastic materials (VEMs) are subjected to cyclic loading, the response of the material can be out of phase with the applied drive force. The amount of lost energy can be related to the phase shift δ or the tangent of the phase shift, $\tan\delta$. If we take equation 1.1 and replace σ and ϵ with:

$$\sigma = \sigma_0 e^{i\omega t} \tag{1.3}$$

$$\epsilon = \epsilon_0 e^{i\omega t - \delta} \tag{1.4}$$

then E becomes a complex number:

$$E^* = \frac{\sigma}{\epsilon} = \frac{\sigma_0}{\epsilon_0} e^{i\delta} = \frac{\sigma_0}{\epsilon_0}(\cos\delta + i\sin\delta) \tag{1.5}$$

Here E^* is the complex modulus of the material. The real part is given by $Re(E^*) = E' = \frac{\sigma_0}{\epsilon_0}\cos\delta$ and the imaginary part is given by $Im(E^*) = E'' = \frac{\sigma_0}{\epsilon_0}\sin\delta$. The ratio of the imaginary part of the modulus to the real part is a measure of the energy absorption and is sometimes called the *loss coefficient* [34]

$$\tan\delta = \frac{Im(E^*)}{Re(E^*)} \tag{1.6}$$

The larger $\tan\delta$, the greater the energy absorption or dissipation in the material. This can be used to quantify the loss in metals, but the values of $\tan\delta$ for metals or stiffer materials in general are much lower than those reported for polymers (see Figure 1-6).

The amount of energy dissipated by the material can also be quantified by the ratio of the energy dissipated by the system (ΔW) to the energy given to the system (W). This ratio is known as the *loss ratio*. For the case when the stress and the strain are sinusoidal, the *loss ratio* is related to the *loss coefficient* ($\tan\delta$) by [35]:

$$\frac{\Delta W}{W} = 2\pi\tan\delta \tag{1.7}$$

Equations 1.6 and 1.7 describe the two figures of merit most commonly used to describe the energy dissipated by materials. It can also be seen form the equations that while $\tan\delta$ assumes a sinusoidal drive and response, the *loss ratio* is simply the ratio of the energy dissipated by the system to the energy used to drive the system. This makes the *loss ratio* universally valid regardless of the shape of the drive or the material response.

1.4 Damping

1.4.1 Damping Mechanisms

Damping in materials can be divided into two main categories based on the mechanism responsible for the loss and their time (or frequency) dependence: *static hysteresis* and *dynamic hysteresis*[2].

Static hysteresis describes that component of damping that has no frequency dependence within the frequency ranges of interest for damping applications. There are two main sources for *static hysteresis*; magnetoelasticity and plastic deformation.

Loss due to magnetoelasticity is observed in magnetic materials such as structural steels. The loss in these steels, while low compared to viscoelastic materials, is high when compared to other non-magnetic structural metals. The loss is due to the magnetic hysteresis caused by the stress-induced domain wall motion (stress rotates the magnetic moments in the sample, but the loss is due to the motion of the domain walls).

In the case of loss due to plastic deformation, the loss is due to the nucleation and motion of dislocations in the material. This loss mechanism is only observed at stress levels higher than the elastic limit of the material. This loss due to plastic deformation depends on the cyclic history of the material. The loss decreases as the cycle number increases, as a result of the work hardening of the material that decreases the mobility of the dislocations responsible for the additional loss. This variation of the loss with the strain history makes this mechanism impractical for cyclic energy absorption.

Dynamic hysteresis is used to encompass materials that show a loss that has a strong time dependance. Theses materials generally can be described by differential equations that

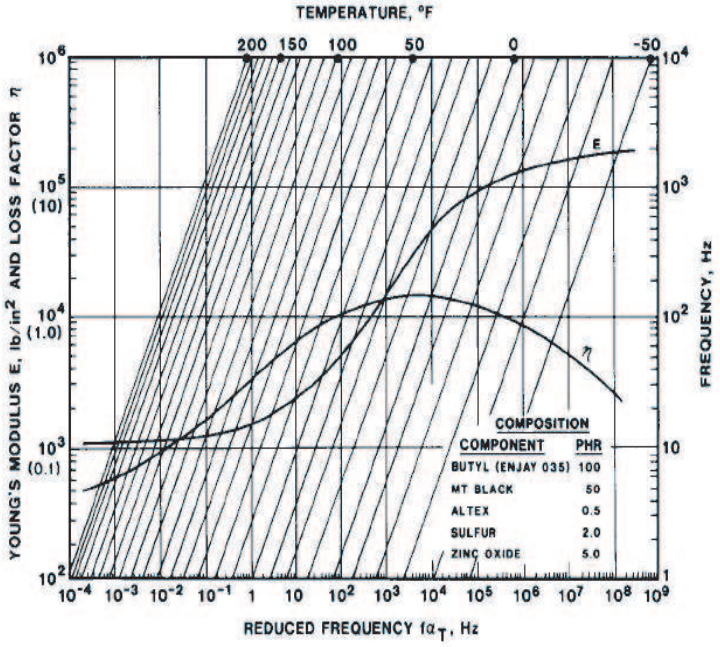

Figure 1-5: Modulus and loss factor as a function of temperature for butyl rubber, form Harris' Shock and Vibration Handbook [2].

have time derivatives of the stress or strain. Viscoelastic materials are a good example of materials that fall within this category since the loss in them is due to relaxation processes of the polymer chains as they are stretched. The frequency dependence of the complex modulus used to describe the material, and hence the loss ratio, are especially frequency dependent near the relaxation peaks. Figure 1-5 show the characteristic loss and modulus dependence of a typical viscoelastic material to the reduced frequency, which is the product of the frequency and a temperature factor. As can be seen, the temperature dependence of the modulus is analogous to its frequency dependence. Frequency dependence of the complex modulus (E^*) is not easily calculated using simple material parameters, but can be fitted by Equation 1.8. The temperature dependence is taken into account by the α_T, and can be obtained from an Arrhenius type expression shown in Equation 1.9, where T is the temperature T_0 is the reference temperature. All other variables in these two equations are fitting parameters, unique to the specific polymer system being modeled.

$$E^* = \sum_{i=0}^{n} \frac{a_n + b_n(if\alpha_T)^{\beta_n}}{1 + c_n(if\alpha_T)^{\beta_n}} \tag{1.8}$$

$$\log \alpha_T = T_A \left(\frac{1}{T} - \frac{1}{T_0} \right) \tag{1.9}$$

1.4.2 Damping relations

One of the most fundamental ways to quantify damping in materials is to characterize their *damping energy*. The damping energy can be defined in three different ways [2]:

D_0= *Total damping energy*, the total amount of energy dissipated per cycle.

D_a= *Average damping energy*, the average amount of energy dissipated per unit volume, per cycle.

D = *Specific damping capacity*,is the energy dissipated per unit volume per cycle at a specific point in the sample.

The *average damping energy* differs from the *specific damping energy* in that it is the result of the average stress distribution on the sample and depends on the sample geometry The *specific damping energy* is independent of the sample geometry, because it only consider the loss at one point in the sample.

The stress dependence of the *Specific damping capacity* varies widely for different materials, and therefore can not be fitted by one equation. However at low to intermediate stress levels it can be approximated by:

$$D = J \left(\frac{\sigma}{\sigma_e} \right)^n \tag{1.10}$$

Where J and n are fitting parameters and σ_e is the fatigue strength of the material. For viscoelastic materials the values of n are between 2 and 3. For materials that show *static hysteresis* the values for n are generally larger than 3, and can even be higher than 30.

1.4.3 Ni–Mn–Ga

The stress-strain loops, measured initially under compression only, suggested that FSMAs would exhibit a large hysteresis if a full tension and compression loop was measured [14]. More recently full tension and compression loops were measured in Ni–Mn–Ga single crystals, and show a large hysteresis [36, 37]. The large hysteresis was not the most desir-

able feature for an actuator material, but could be a useful feature for a damping material. The strain-field loops for the cyclic actuation of Ni–Mn–Ga also show a large apparent "hysteresis". The area within the loops does not correspond to an energy because strain and field are not conjugated pairs, but it indicates that energy is dissipated every cycle. The large cost of the single crystals and the their inherent brittleness prevented their use as dampers, since they are likely to fail under tension.

Figure 1-6 shows a stiffness-loss map that includes several materials commonly used for damping along with some structural metals. In general high stiffness materials tend to have low loss, and high loss materials tend to have low stiffnesses. The figure of merit used to quantify the quality of the materials as dampers is the product of the stiffness and the loss expressed as $\tan\delta$, mainly $(E\tan\delta)$. The higher this product the better the materials work as energy absorbers. It is reported that most materials have an $E\tan\delta$ product lower than 0.6 GPa. In the log-log map a line with an arrow pointing at "best performance" corresponding to $E\tan\delta = 0.6$ is seen on the upper right corner and the region above and to the right is labeled best performance[3]. Materials that can exhibit products comparable or higher than 0.6 are desirable vibration dampers.

1.4.4 Magnetic Materials

Magnetically active materials have been shown to be good passive dampers. Terfenol-D showed a high capacity to dissipate vibrational energy without a magnetic field applied to the sample. The loss in these materials is due to irreversible magnetic domain wall motion and, and in the case of metallic magnetic materials, eddy currents contribute to the loss as well [26, 27].

Damping in Ni–Mn-Ga has been recently studied on single crystals of Ni–Mn–Ga exhibit very large loss when subjected to cyclic loads. The loss was measured using a Dynamic Modulus Analyzer and by then converting the loss ratio to a $\tan\delta$. The $\tan\delta$ reported for the FSMA single crystals showed a loss that was dependent on the strain amplitude imposed on the crystals. The $\tan\delta$ of the materials increased from 0.6 to 1.1 as the strain level went from 1% to 3.7% [36].

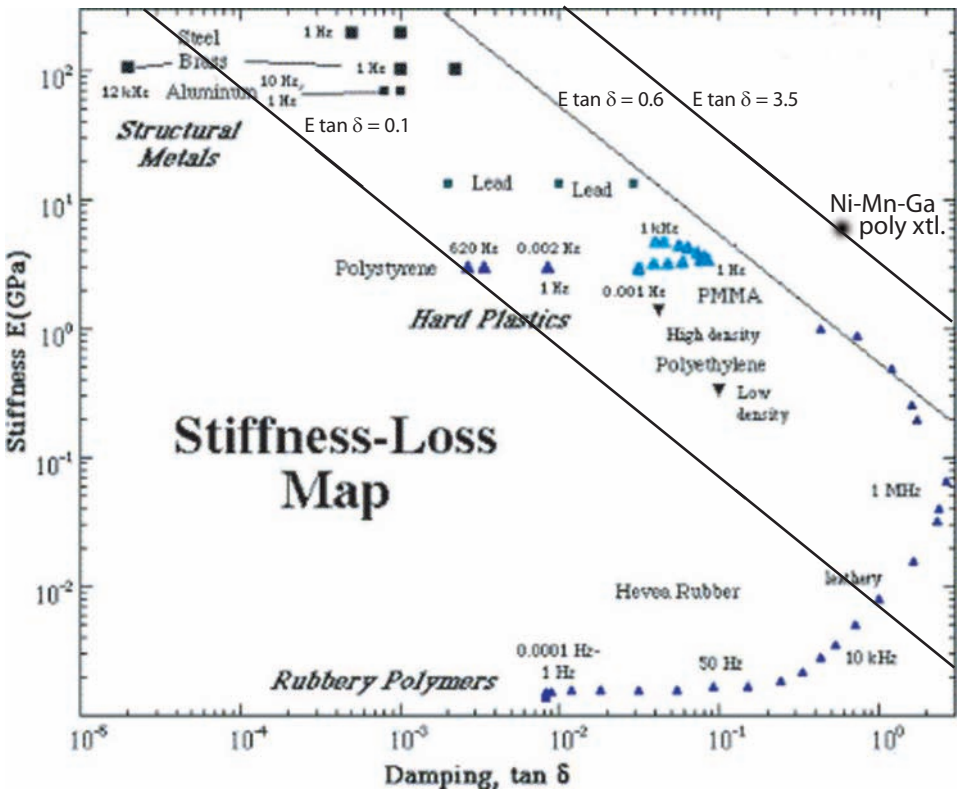

Figure 1-6: Stiffness-loss map showing different materials, reproduced from Y.C. Wang et al. Materials Science and Engineering A [3].

Bulk polycrystals of Ni–Mn–Ga also show a large capacity to dissipate mechanical energy. The data reported shows that polycrystals exhibit loss tangents near 0.5, and stiffnesses of about 7 GPa [38]. This gives a product of the stiffness times the $\tan\delta$ on the order of 3.5 GPa, and puts the material well above most commonly used materials shown in Figure 1-6. The stiffness is not a high as that of the metals shown on the figure, but the loss is much higher.

The first studies on the use of Ni–Mn–Ga/polymer composites as energy absorbers were published by the author and they predate the work on single crystals and polycrystals mentioned above. Those early publications also predate the work on FSMA/polymer composites mentioned in the previous section. This work showed the ability of the composites to dissipate more energy than the matrix material and presented evidence that indicated that the composites had twin boundaries that could be moved by an external stress. This was the result of the proper alignment of the particles in the composite, this had never been

done before and there were doubts that it could be done. The content of those publications [39, 40, 41, 42] is not summarized here because the full research will be presented in the following chapters.

1.5 Spark erosion

As discussed previously, spark erosion can be used as an alternative to grinding to produce spherical particles of Ni–Mn–Ga that are tens of microns in diameter and smaller.

Small spherical metallic particles can be produced by spark erosion [43, 44]. This method consists of placing electrodes of the desired metal in a liquid dielectric bath and pulsing a current across the electrodes. The electric discharge generates a plasma and melts or vaporizes a small amount of the electrode material. The dielectric material quenches the ejected material and spherical particles are formed in the liquid. Two system configurations commonly used for the spark erosion of the FSMA particles used in this study.

The first is the "shaker pot" configuration, which consists of two solid electrodes of the desired material separated by a relatively large distance. The space between the electrodes is filled with chunks of the material to be sparked (the "charge"). The electrodes and the material are placed in a container with a mesh bottom and submerged in the dielectric. The container or "pot" is constantly shaken to generate new gaps between the charge chunks, and to get the newly formed particles to fall to the bottom through the mesh.

The second configuration, the "constant-gap", consists of a large electrode made of the desired metal cast (in the shape of a large disk) and a bar electrode also made of the desired material. The large circular electrode is rotated while the bar electrode is moved by a linear actuator to maintain a constant gap between the two electrodes. The entire assembly is submerged in the dielectric bath. An electric discharge milling machine power supply provides the pulsed current for the erosion. This configuration produces a higher yield [43, 44].

Spark erosion can be used to generate small particles of a variety of conductive materials including Ni–Mn–Ga to be used in the composites. The spherical particles obtained by spark erosion have no shape anisotropy, so their orientation in the matrix will be controlled

only by their magnetocrystalline anisotropy.

1.6 Thesis layout

The work presented in this thesis will show how adding particles of Ni–Mn–Ga to a polyurethane matrix yields composite materials that can dissipate more energy than the matrix with no filler or with an inert filler such as iron or Terfenol-D.It will show that the extra loss observed in the FSMA loaded composites is due to the motion of twin boundaries in the particles embedded in the polymeric matrix. And that the fabrication procedure used to make the composites provides the appropriated texture for the particles to respond to an external stress on the composite.

The thesis can be divided in two parts: the first half shows indirect and direct evidence of the mobility of the twin-boundaries in the composites, the second half shows how the addition of Ni–Mn–Ga to the matrix affects the damping capacity of the composite.

Chapters 2 and 3 use two different magnetic measurement techniques to show that uniaxial compressive stresses applied to the composites can change the distribution of the twin variant distribution in the particles. These chapters rely on the changes in the direction of the easy axis of magnetization to infer changes in the variant distribution.

Chapter 4 presents measurement techniques that directly relate to the crystal structure or the macroscopic shape of the particles. The measurements confirm the conclusions drawn from the magnetic measurements.

This marks the end of the first part. The measurements shown to this point will prove with a high degree of certainty that there are twin boundaries in the composite that can be moved by an external stress and that the changes due to the applied stress can be reversed by another stress applied in a normal direction.

Chapter 5 shows the effect of adding FSMA particles to the composite on the ability of the composites to dissipate mechanical energy. Evidence that the additional loss observed in the composites is due to twin-boundary motion will be presented.

In Chapter 6 simple numeric models are used relate the mechanical response of the individual components of the composites to the overall response. A finite-element model

is used to show the distribution of the stresses on the particles.

Chapter 7 looks at some of the possible uses of Ni–Mn–Ga polymer composites in engineering applications. The heating of the sample as a result of the energy dissipation in the FSMA particles is examined. The expected frequency response of the composites is discussed.

The last chapter summarizes the results and conclusions drawn in the previous chapters and proposes some ares of interest for possible future studies of the composite materials.

Chapter 2

Torque measurements

The torque magnetometer measurements described in this section show the effect on the magnetic anisotropy of applying a mechanical stress to a Ni–Mn–Ga/polymer composite sample. These measurements give insight on the redistribution of twin variants in the composites. Torque magnetometry measurements, while not a direct measure of the twin distribution as provided by x-ray diffraction, are a clear indication of changes in the magnetic anisotropy of the samples due to the re-arrangement in the twin boundary distribution, because the magnetic easy axis and the crystallography c-axis are connected by the magnetocrystalline anisotropy.

2.1 Torque magnetometry

When a magnetic material is placed in a magnetic field it will try to rotate to be parallel with the direction of the applied field. Magnetic compasses are an example that illustrate this effect. The force that makes the needle rotate into the field, on top of being useful for navigation, can be used to determine certain properties of magnetic materials if the magnitude of the torque exerted on the magnetic material can be measured. The torque magnetometer is the most direct measurement of the magnetic anisotropy of a material.

The torque $\vec{\tau}$ experienced by the magnetization of a sample is given by $\vec{\tau} = -\vec{M} \times \vec{H}$, where $\vec{M}$ is the magnetic moment density vector, and $\vec{H}$ is the applied magnetic field vector. If the field is smaller than the anisotropy field of the material, then the magnetization of the

material will not be able to fully rotate into the field. In this case the sample will try to rotate to align its easy magnetization direction with the field. By measuring the torque exerted on the sample as a function of the angle relative to the direction of the field it is possible to determine the direction of the easy axis of magnetization. The value of the magnetic anisotropy constants of the material can also be obtained from the torque vs. angle measurements.

In a torque magnetometer a large laboratory electromagnet provides the uniform magnetic field needed for the measurement. The sample holder doubles as the axis of rotation for the sample and connects to the torque measurement head. The general layout can be seen in Figure 2-1. The torque head serves two functions; it rotates the head in controlled angle increments and it measures the torque on the sample due to the applied field. The torque mechanism uses an optical null detector to measure the relative rotation of the head to the air bearing mounted sample. The relative rotation is suppresed by applying a current across four sets of printed stator wires on a circuit board that has four permanent magnets concentrating a magnetic field perpendicular to the circuit board directly over each stator. The restoring force needed to overcome the torque on the sample is directly proportional to the amount of current applied to the rotation motor stator wires. A precision current measuring resistor generates a voltage drop that is measured by a digital meter with a computer binary coded interface. The torque on the sample is registered by the computer that controls the magnetometer.

In this torque measurement the magnetic field applied to the sample is held constant while the head rotates in specified angle increments. The torque on the sample is then plotted as a function of the angle of rotation and separate plots are generated at each test field.

2.2 Sample preparation

Samples for torque measurements were prepared by weighing out separately the matrix and filler material to yield the desired volume fraction composite. The matrix and filler were then mixed and put in a specially made, two-part Teflon mold to obtain sheets of about

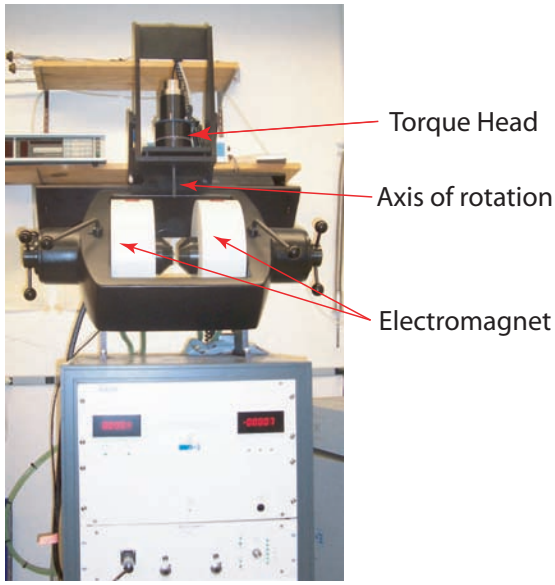

Figure 2-1: Photograph of the torque magnetometer used with key components labeled.

$1\ \mathrm{cm} \times 2\ \mathrm{cm} \times 0.1\ \mathrm{cm}$. Once the slurry was placed in the mold it was cured under a 4 kG magnetic field oriented normal to the plane of the sheet for 30 minutes. This produced samples with particle chains normal to the the sample plane. Samples were then taken out of the field and allowed to fully cure for at least 24 hours. Once fully cured, disks of $0.6\ \mathrm{cm}$ in diameter were punched out of the sheets with the disk axis parallel to the direction of the field applied in the curing step.

For the experiments shown in this chapter two different polyurethanes were used as the matrix materials, a Kalex Tuff Stuff® (part number 04024; shore A-85 hardness) and a Lord Corporation, Lord Adhesive (7540 A/B Urethane adhesive; shore D-85 hardness). Several different filler materials were used; powder obtained from crushing scraps of single crystals of Ni–Mn–Ga, powder spark eroded under liquid nitrogen or under liquid argon, as well as inert fillers iron or Terfenol-D powders. The procedure for the fabrication of the composites was the same for all the matrix and filler materials used.

2.3 Experimental setup

For this set of experiments an ADE Technologies, Digital Measurement Systems Torque/Vibrating Sample Magnetometer model 1660 was used to measure the change of in-plane torque as a

function of prior applied load on the sample. The instrument is configured as follows: a DC magnetic field is applied along the x-direction, the sample is mounted on a holder that rotates about the z-axis, and the torque resulting from the magnetic moments in the xy-plane interacting with the applied field is registered as a function of the angle of rotation about the z-axis. Figure 2-2 shows the configuration of the instrument. A registration mark was drawn on the circular surface of the sample and used as a reference direction for the initial field direction and strain direction applied to the sample. The samples were measured first as cast, with the initial field in the torque magnetometer along the reference line, and this torque curve was taken as the starting condition for the sample. The samples were then removed from the magnetometer and subjected to uniaxial compressive strain increments in the xy-plane. The first set had the strain applied parallel to the reference mark. After each strain increment, the stress was removed and the sample was placed in the magnetometer maintaining the same orientation between the reference mark and the initial field direction for all measurements in a series. At the end of each strain series, the sample was compressed along the direction of the curing field to try to reset the sample to the initial condition, and was then measured in the magnetometer. The strain cycle was then repeated with the strain direction orthogonal to the one used in the previous cycle. The relative orientation of the reference line to the initial direction of the magnetic field was maintained regardless of the orientation of the applied strain to the reference line used in each set of measurements.

2.4 Results

Figure 2-3 shows the maximum peak-to-peak torque vs. applied strain for a composite sample comprised of 25 volume % crushed Ni–Mn–Ga single crystal in the Kalex polyurethane matrix. The trace labeled "in-plain strain" shows the effect on the in-plane torque of an incremental compressive strain along the reference line on the sample. The sample shows initially a very slight decrease in the torque until a threshold value is reached, at which point the torque increases strongly as a function of the applied strain. The point labeled "out of plane strain" shows the maximum torque after the sample is subjected to a reset

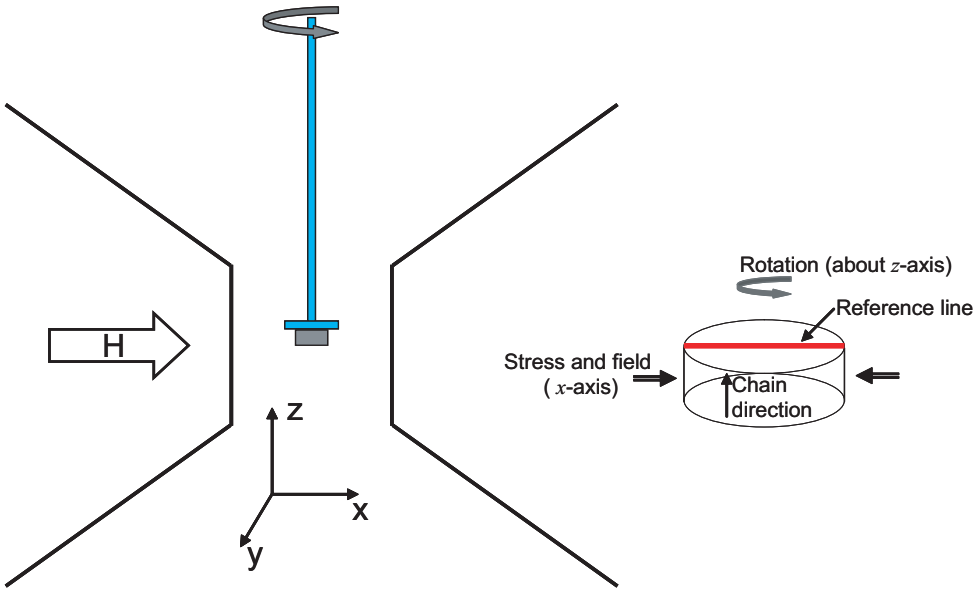

Figure 2-2: Schematic of a torque magnetometer.

strain normal to the sample plane direction.

The Lord 7540 polyurethane has a hardness on the Shore D scale of 85 and the Kalex matrix has a Shore A 85 hardness, making the later far more compliant then the Lord matrix. The effect of the matrix stiffness can be seen in Figure 2-4. The two traces show a similar behavior both showing a slight decrease in the in-plane maximum torque registered and then showing an increase in the torque. The stiffer matrix reaches the initial threshold sooner than the more compliant one. The slope of the curves is also different for the two samples after the threshold has been reached. The stiffer matrix shows a faster increase in the torque as a function of strain than the more compliant matrix. Another difference that can be observed is that the sample with the stiffer matrix shows a change in the slope of the curve at about 13% strain. This decrease in the slope could indicate that the in-plane torque of the sample is reaching its saturation value, implying that application of larger strain produces no more change in the maximum peak-to-peak torque measured.

The effect of the volume fraction of the filler material on the stress-induced torque of

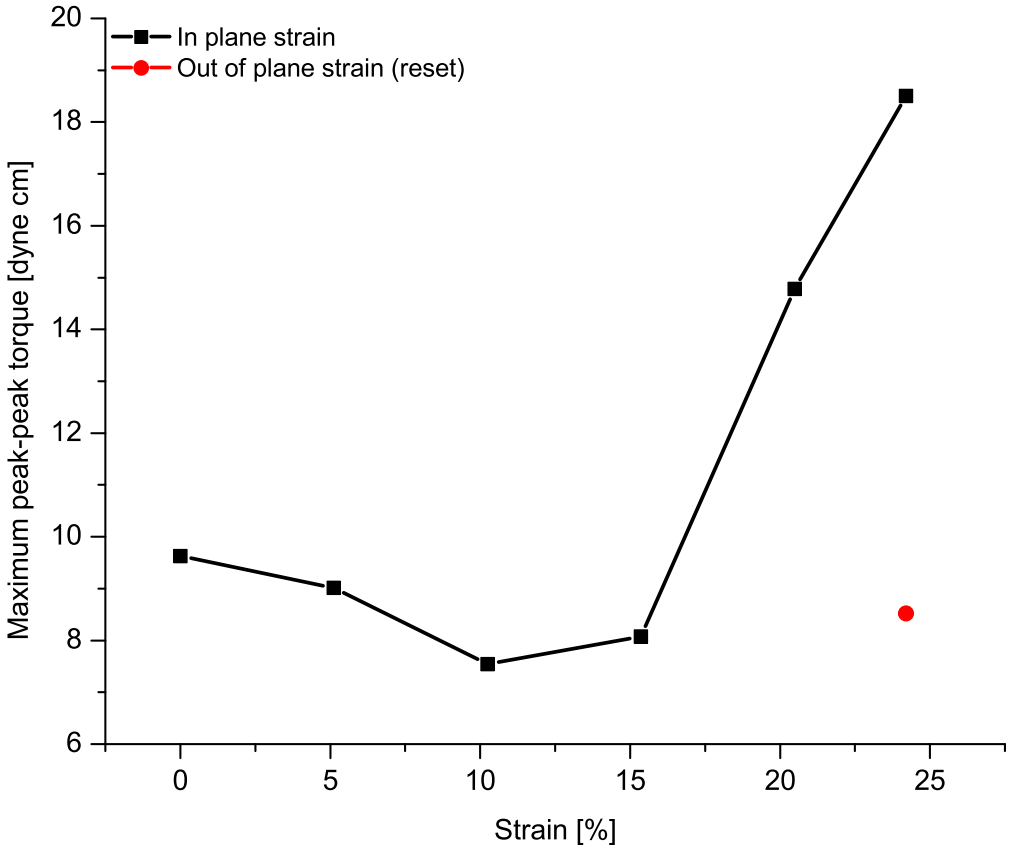

Figure 2-3: Peak-to-peak torque as a function of the applied strain in two different directions for large strains on 25% volume FSMA in Kalex polyurethane.

the composites' load can be seen in Figure 2-5. Both samples show the same general trend; the torque remains mostly constant at low strain values and then starts increasing after a threshold value is reached, at around 8% strain. The initial torque of the 40% sample is higher than the torque of the 24% sample by ratio of 2.7/1; the ratio for the highest strain measured was 2.1/1.

The effect of repeated strain-and-reset cycles is presented in Figure 2-6. For this experiment each cycle consisted of straining the composite sample 25%, measuring the peak-to-peak torque, re-setting the sample by stressing it in the normal direction, and then re-measuring the torque. The graph shows the effect of 28 cycles on the sample, indicating that the maximum torque decreases from its initial value rapidly at first but shows a much

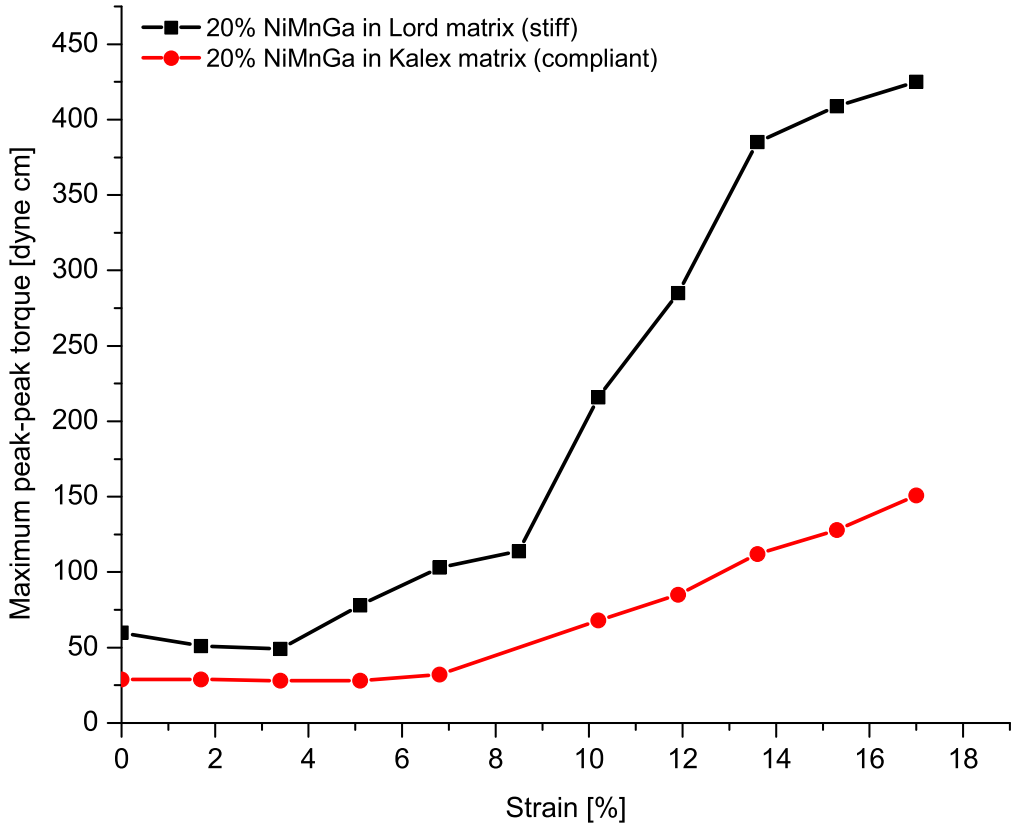

Figure 2-4: Peak-to-peak torque as a function of the applied strain on composites based on two matrices having different stifnesses.

smaller change over consecutive changes after 5 cycles.

The possibility that the increase in the peak-to-peak torque in the Ni–Mn–Ga composites could be the result of the physical rearrangement of the particles in the matrix material had to be explored to validate the results obtained in the FSMA-loaded composites. A control sample was made using Terfenol-D as the filler material following the same procedure as for the Ni–Mn–Ga composites. Terfenol-D is an iron-based magnetostrictive material used in actuator applications; it has been suggested as an energy absorbing filler in damping applications [26, 27, 45]. The Terfenol-D control sample had 24% by volume of the filler, the same volume fraction as the Ni–Mn–Ga samples it is compared to. The results for this sample are shown in Figure 2-7, along with the data for a Ni–Mn–Ga sample of compara-

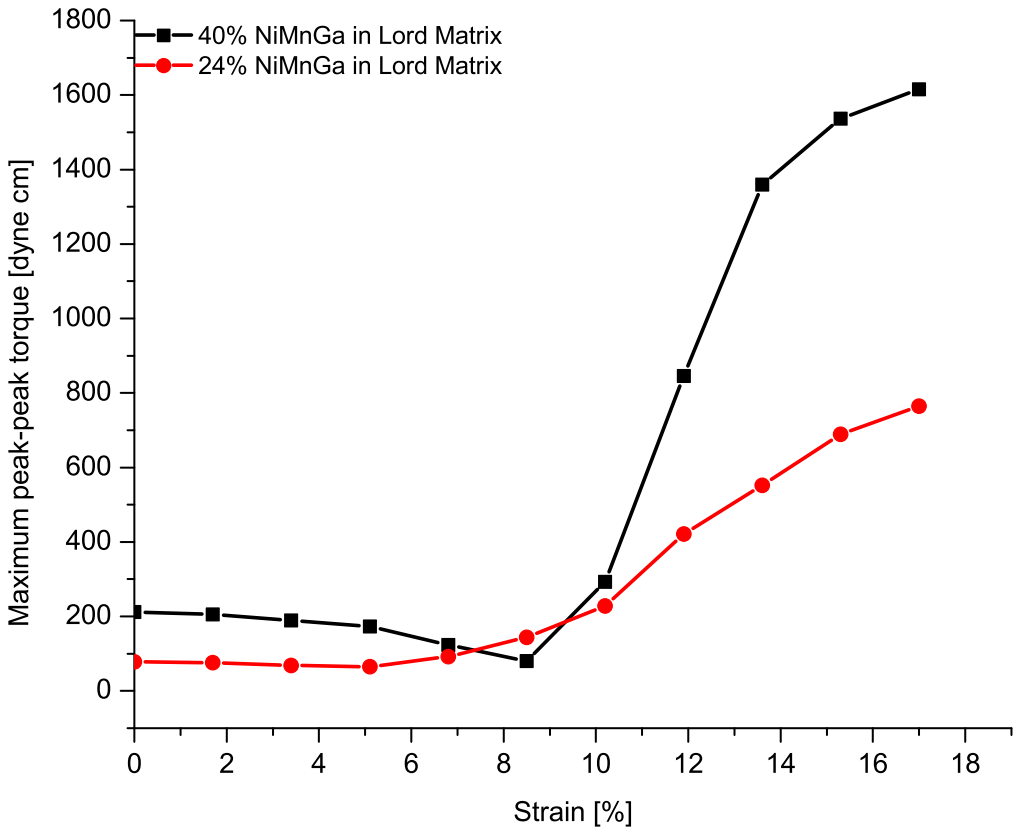

Figure 2-5: Effect of the volume fraction on the peak-to-peak torque as a function of strain for (sample N) 24% by volume of FSMA in Lord 7540 and (sample O) 40% of FSMA in Lord 7540

ble loading. It can be seen from the graph that the Terfenol-D sample initially has a larger torque due to its larger magnetization. However the change in the maximum peak-to-peak torque in the Terfenol-D loaded sample is very small compared with the change shown by the FSMA-loaded sample under the same loading conditions. The control sample also does not show the threshold behavior observed in all the FSMA loaded samples.

2.5 Discussion

The results of the different torque measurements presented in this chapter can be combined to provide very strong evidence that the twin boundaries in the FSMA particles embedded

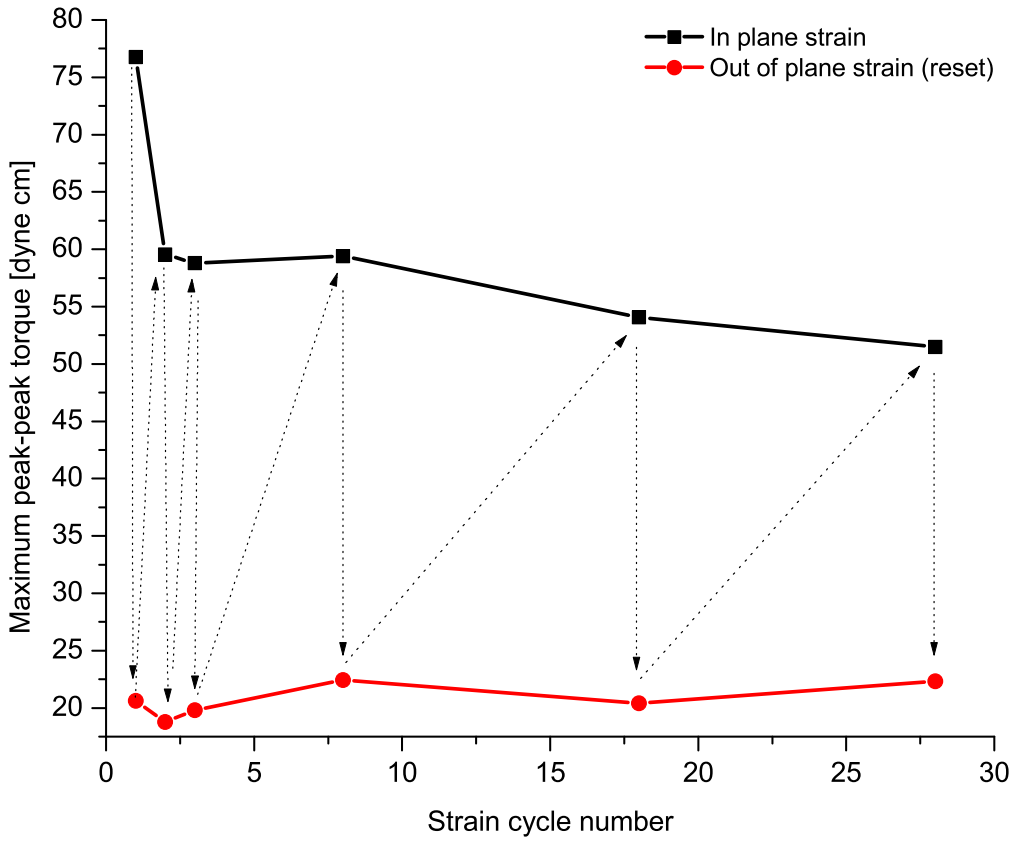

Figure 2-6: Effect on the maximum peak to peak torque of repeated strain-and-reset cycles for 25 % in-plane strain.

in the composites studied can be moved by an external stress. The plots in this section are presented as a function of strain rather than stress. It was possible to apply a controlled strain to the samples, but controlling the load on the composite samples proved difficult because the samples were quite small and the polymer matrix relaxes as the sample was stressed. The viscoelastic nature of the matrix made it quite difficult to load the samples to a fixed stress.

While the total stress on the *composite* sample can easily be estimated from the modulus of the composite and the imposed strain, the actual stress on the *individual particles* could not be measured directly and is not easily calculated analytically due to the complex geometry of the composite. An estimate of the distribution of the stresses on the particles

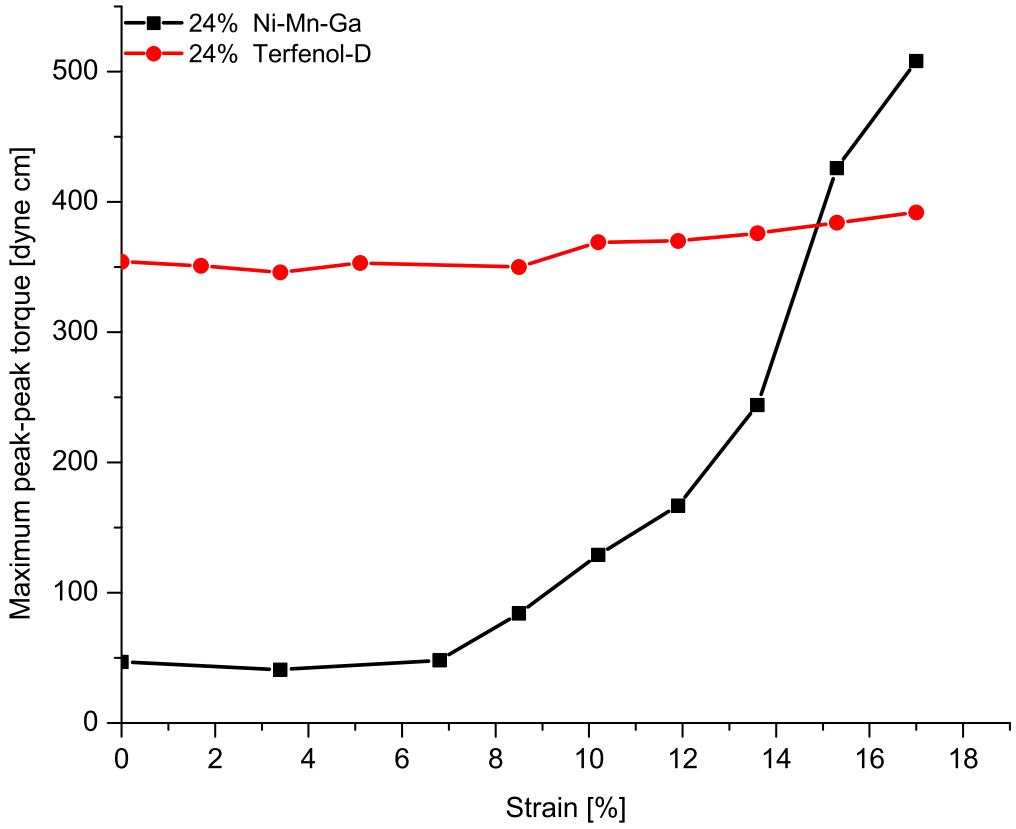

Figure 2-7: Maximum peak-to-peak torque for (sample G2) 24 % Ni–Mn–Ga in Lord polyurethane and (sample J) 24 % Terfenol-D powder in Lord Polyurethane.

and the surrounding matrix can be obtained by simulating the structure with a finite-element method and is presented in Chapter 6.

Even though these experiments do not constitute direct evidence of the motion of twin boundaries, they make up for this in the consistency of the features shown in the various experiments with those expected from a system responding to an applied load by twin boundary motion. These features include easy axis changes under stress that can be largely restored by the application of an orthogonal stress, as well as the threshold and saturation characteristics. Single crystals of Ni–Mn–Ga with mechanically active twin boundaries exhibit pseudo-plasticity, that is they behave elastically, like all other materials, until a threshold stress is reached at which point the modulus of the crystal decreases by up to 3

orders of magnitude [37, 46], but unlike other materials the modulus returns to its initial value after the sample has strained an amount proportional to the difference between the long and short unit cell axes. The deformation in this transition stage, while permanent after the stress is removed, can be reversed by applying a stress of equal magnitude in the opposite direction, returning the sample to its original dimensions. This threshold behavior was observed in all the FSMA composite samples measured and can be clearly seen is Figures 2-3, 2-4, 2-5 and 2-7. Figure 2-3 and 2-6 shows that the effect of the in-plane strain applied can be reversed by an equivalent stress of the same magnitude, but opposite sign.

While a stress-strain curve cannot be measured using torque magnetometry, the results from the torque measurements can be related to the motion of twin boundaries in the sample because the motion of twin boundaries change the orientation of the magnetic easy axis and thus changes the magnetic anisotropy. Figure 2-8 shows schematics for two extreme twin configurations and their corresponding torque curves. In the first case labeled (a), the main variant has its c-axis, and due to the high anisotropy [47, 48] also its magnetic easy axis, pointing along the rotation axis of the magnetometer as depicted in Figure 2-2. As the compressive stress is applied the magnetic easy axis of the particles rotates into the xy-plane as the twins move to accommodate the in plane stress, transforming the particles into the configuration shown in Figure 2-8 (b). Now the moments lie in a fixed direction in the plane where the field can exert a torque on them, measurable by the magnetometer. Particles that have not fully transformed from one variant to the other will show curves that are intermediate to the ones shown in Figure 2-8(a) and (b), making it possible to infer the average twin configuration of the sample based on the torque.

The magnetic moments in the as-cured samples lie along the direction of the field applied while curing, in this case the disk normal, hence they are in a low-torque configuration. The low initial torque measured in all samples is consistent with this interpretation. It also implies that there is no texturing of the sample in the plane that would cause a torque due to shape anisotropy in the samples.

In the composites tested, active twin systems respond to strain applied in the plane of the sample by increasing the fraction of variants having their c-axis parallel to the applied compressive force. Variant re-orientation starts once the threshold for twin motion is ex-

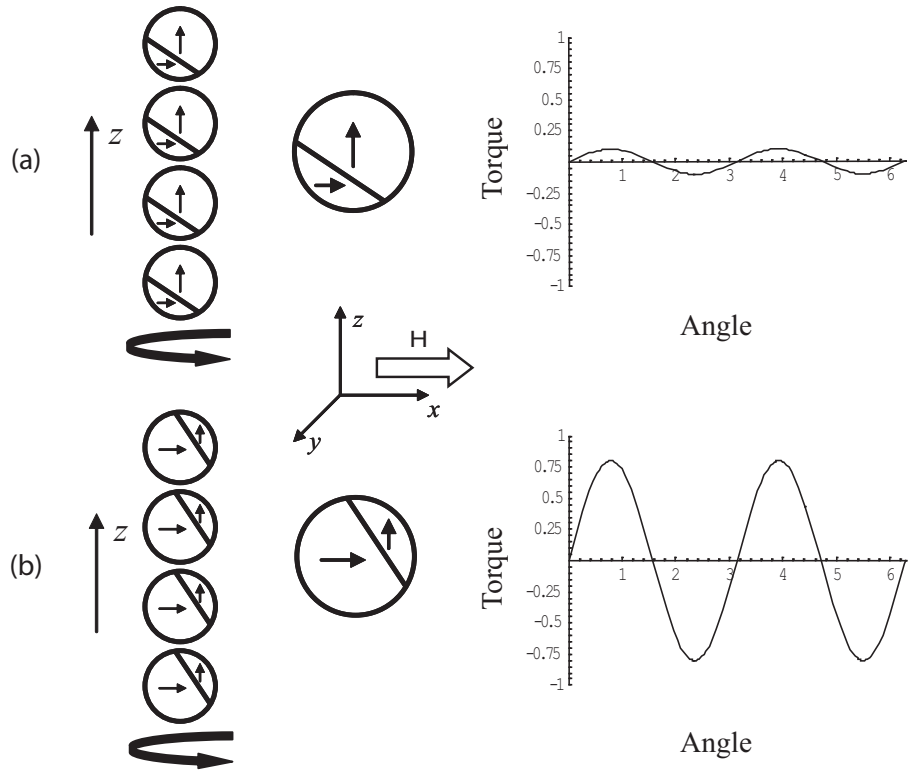

Figure 2-8: Schematic of the resulting torque for (a) a particle with the main variant normal to the xy-plane, and (b) a particle with the main variant in the xy-plane

ceeded. The increase in the variant fraction with an in-plane magnetic easy axis results in a higher measurable torque. All the FSMA-loaded samples measured responded to the increasing strain with an increasing torque after the threshold was reached. This provides evidence that the twin systems in the particles are responsive to applied loads.

For anyone familiar with single crystals of Ni–Mn–Ga it would seem counter-intuitive that a stress applied along any direction in the plane of the composites would increase the measured torque, because they only respond to stresses along the two (100) directions that are not contained in the active twin-plane. By extension in the composite only stresses along one of the two $\{100\}$ directions that did not contain the c-axis at the start of the experiment should respond to a stress. However it must be kept in mind that the samples used here only had texture along the direction of the curing field, normal to the sample plane, thus the composites have a fiber texture. For mostly-single-variant particles the c-

axis of the dominant variant is only a few degrees off from the direction of the net magnetic moment of the entire samples. the net moment is the vector sum of the magnetic moments of the individual variants, resulting in a highly textured sample along that direction. The variants with the lower volume fraction will however have no preferential direction, and they should be distributed uniformly in the plane normal to the main variant easy axis. A direct result of this random distribution of low-volume easy axes along the fiber axis is that the samples should respond to stresses applied along any direction in the plane and not only discrete ones, as would be the case for individual single crystals. The reference line on the composite sample was drawn along a random direction that had no relation to the geometry of the mold used for making the sample. The samples responded to compressive strains along and normal to the reference line, confirming that there was no texture in the plane of the sample. In all the samples the easy axis direction was observed to correspond to the direction of the applied compressive load, providing further corroboration of the twin mobility. The ability to set the easy axis of magnetization along any direction in the plane by first re-setting the sample with an out-of-plane stress and the an in-plane stress along the desired direction, shows the reversibility of the sample. This reversibility is additional evidence of stress-induced twin-boundary motion.

The effect of the matrix stiffness can be seen in Figure 2-4, the stiffer matrix shows a stronger response to the applied strain than the softer one. This is because a stiffer matrix will require a smaller strain to reach the threshold stress of the particles and equal strain increments will result in a stress increment that will be higher by the ratio of the matrix stiffnesses. This shows how the stiffer matrix transfers more of the load to the particles. A more in-depth discussion of the effect of the matrix stiffness and the importance of the proper selection of the matrix will be given in Chapter 8.

The net stress-induced torque is a function of the volume of magnetic moments in a given direction in the plane of the sample; it will be a function of the number of particles in the sample and the fraction of the variants in the particles whose c-axes lie in the plane. It can be seen that this general trend is observed. In Figure 2-5 the sample with 40 volume % loading shows a much higher torque than the sample with 24%. While the ratio of the volume fractions of the two samples is about 1.7/1 the ratios of the measured torques at

the beginning and end of the strain series do not match this ratio. At low strain values they deviate some, showing a ratio of 2.7/1, but at the higher strain values measured the ratio has dropped to 2.1 to 1, coming closer to the expected 1.7/1 ratio.

It is important to explore the possibility that the effects observed in these measurements could be due to factors other than the motion of twin boundaries. Anelasticity in the matrix could be responsible for the increase in the measured torque. That is, particles could be under stress even after the stress on the composite was released. However the evidence is that the residual stress is small because the dimensions of the samples were measured before and after they were subjected to the strains and no noticeable difference in their dimensions was found.

Delamination of the particles is another important concern. If there were any delamination at the particle/polymer interface the particles would be free to rotate to some extent in the matrix and would not show an increase in the torque, because they would shift in their cavities rather than exert a torque on the matrix.

The same experiments were repeated using samples with the same volume fraction of a magnetic filler that would yield the same particle-chain structure but that should not present a change in the direction of the easy axis of magnetization as a function of the applied strain. Terfenol-D particles would form chains to reduce the magneto-static energy of the systems but no specific crystal direction would tend to orient along the field direction applied while curing because of its low magnetic anisotropy. Terfenol-D was chosen as a control filler, because it also exhibits a reversible change in the preferred direction of magnetization in response to an applied stress, but unlike the case of an FSMA this change is only evident as long as the sample remains under stress. Figure 2-7 clearly shows that the response of the Terfenol sample is very different from the FSMA samples, showing a mostly flat torque as a function of applied strain unlike the FSMA response. The higher torque of the Terfenol sample is most likely an effect of its higher magnetic moment.

Plastic deformation of the particles could explain the threshold behavior and subsequent increase in the torque, but this is not observed in the control sample, as the yield stress is much higher for Terfenol-D. A compressive stress on the particles would lead to expansion in the directions normal to the compression due to the Poisson effect. For any

spherical particle the Poisson effect would cause an easy anisotropy plane normal to the compressive stress. In these experiments the opposite was observed, the easy axis direction corresponded with the direction of the applied strain.

Figure 2-5 shows that the value of the measured torque is a function of the amount of magnetic material in the composite. The relation of the torque to the loading fraction is self evident because the torque is a function of the magnetization and the total moment is a function of the amount of magnetic moment present.

Figure 2-6 shows that the stress-induced torque can be reversed by application of an orthogonal stress. Plastic deformation would be very difficult to reverse in the consistent manner shown in the samples. The decay in the maximum torque observed as a function of each cycle is more than likely the result of new incompatible twin systems nucleating in the particles and impeding their further twin boundary motion. Not many studies on the fatigue of Ni–Mn–Ga alloys are available, but a similar effect has been observed by Hezcko in single crystals of Ni–Mn–Ga cyclicly actuated by rotating permanent magnets. He shows that the strain output of these crystals decreases as they are cycled and the ghost marks on the surface of the crystals hint at the formation of incompatible twin systems [49].

2.6 Conclusions

The measurements presented in this section show that the FSMA/polymer composites show all the features that would be expected from a system with active twin boundaries. There is a threshold for the strain-imposed torque (twin variant rearrangement) followed by a gradual increase in torque as a function of increased imposed compressive strain. The direction of the easy axis of magnetization coincides with the direction of the applied compressive strain as it does in Ni–Mn–Ga single crystals, and the stress-induced torque can be reverted as would be expected from a pseudo-plastic system. Composites that do not twin do not show any of these effects. Combining all these results, a strong case can be made for the mobility of twins under stress in these composites. Direct evidence of the motion of twin boundaries in these composites is presented in Chapter 4.

Chapter 3

Vibrating Sample Magnetometry Measurements

The torque measurements presented in Chapter 2 are complemented by the vibrating sample magnetomer (VSM) measurements presented in this Chapter. The direction of the easy axis of magnetization affects the shape of the magnetization-versus-field plots. Changes in the direction of the easy axis of magnetization can be seen from changes in the magnetization plots. VSM measurements provide a convenient way to explore the changes of the variant orientation in the particles in the composite caused by cycling the material above the austenite transformation temperature or subjecting the composite to stress. This technique is also useful for determining materials properties such as the transformation temperatures and the Curie temperature T_c.

3.1 Vibrating sample magnetometry

A vibrating sample magnetometer measures the magnitude of the magnetization in a material induced by a magnetic field. The magnetometer measures the component of the magnetization along the direction of the measuring field. The magnetization is plotted as a function of the applied field.

In a VSM the sample is attached to a non-magnetic sample holder connected to a vibrator. The vibrator makes the sample oscillate vertically at 75 Hz within the gap of the

electromagnet. This electromagnet is used to generate the magnetic field used in the measurement. On the face of each pole piece of the electromagnet there is a set of two coils approximately 0.75 inch in diameter, 0.18 inch thick and with a 1 inch center-to-center separation. The magnetized sample induces a voltage in the coils as it vibrates. The voltage V is proportional to the frequency of the vibration, the magnetization of the sample and the number of wire turns in the coils, N. The voltage induced in the coil is given by $V = -NA\frac{dB}{dt}$, where A is the cross sectional area of the coils. An advantage of the VSM is that it measures the magnetization rather than the flux density in the sample because the applied field is static relative to the pickup coils. A schematic of a VSM is shown in Figure 3-1 [4, 50]

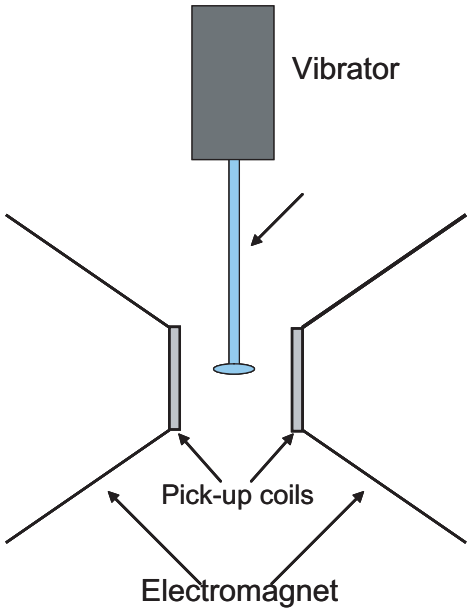

Figure 3-1: Schematic of a vibrating sample magnetometer.

Phase transitions and the Curie temperature of a ferromagnet can be measured by holding the field at a small constant value through the whole measurement and changing the temperature as the magnetization is measured. The saturation moment and susceptibility depend on the crystal structure of the material measured. When a material changes phase, the magnitude of the magnetization measured at constant field generally changes, allowing

the phase-transition temperature to be determined. The phase transitions are seen as peaks in the derivative of the magnetization-versus-field plot. When a ferromagnetic material is heated above its Curie temperature it becomes paramagnetic and the long-range magnetic order vanishes; a large decrease in magnetization is observed. The paramagnetism of the sample accounts for the fact that the field-induced magnetization does not go to zero above the Curie temperature. The magnetometer can also be used determine the direction of the easy axis of magnetization.

3.2 Sample preparation

The same procedure described in Section 2.2 was used to obtain 6 mm diameter disks of the FSMA/polyurethane composite material. These samples were used to study the mobility of twin boundaries and the effect of cycling the composite samples above the austenite transformation temperature. All the composite samples used in the measurements in this section used the Lord 7540A/B polyurethane as the matrix material. A control sample was made with Terfenol-D powder as the filler material to the same 20 vol % fraction as the Ni–Mn–Ga composite samples.

For the determination of the transformation temperatures and the Curie temperature two different types of samples could be used: Ni–Mn–Ga particles attached directly to the sample holder, or the composite disks themselves. For the magnetization-versus-temperature measurements the advantage of using the FSMA particles mounted directly on the sample holder, using double sided tape to hold them, is that the particles reach thermal equilibrium in a short time, eliminating artifacts due to thermal lag. The disadvantage of measuring the magnetization as a function of temperature on the composite disks is they have a low volume of Ni–Mn–Ga. The polymer acts as an insulator, and the temperature has to be changed very slowly ensure that the sample reaches thermal equilibrium.

3.3 Experimental details

3.3.1 Magnetization versus temperature

The temperature dependence of the magnetization of the samples to determine the the Curie temperature as well as the transformation temperatures of the alloy used, martensite start(M_s), martensite finish (M_f), austenite start (A_s) and austenite finish (A_f). The temperature measurements where done at a low field (200–500 Oe) relative to the saturation field of the material. A low field was chosen because the initial susceptibility of the two phases is different enough that the change in magnetization at that field is larger than the change in saturation magnetization from one phase to the other [23].

3.3.2 Magnetization versus field

Magnetization versus field measurements at a constant temperature were made for different in-plane compressive strains on the samples. These measurements were used to look at the changes in the direction of the easy axis of magnetization for a series of thermal and mechanical treatments on the sample.

The first series of measurements looked at the change in magnetization as a function of an incremental strain applied to the composite. The samples were set to a reproducible initial condition by first subjecting them to a compressive out-of-plane strain; the sample in this state was called "zero in-plane strain." The sample was then placed in the magnetometer and the magnetization was measured as a function of the field applied. The sample was removed and a in-plane strain larger than the previous one was applied to the sample before it was re-measured. This sequence was repeated for increasing in-plane compressive strains applied to the sample.

The second set of experiments looked at how the composites respond to stress followed by heating into the austenite phase. The composite disk samples with the particles aligned normal to the disk plane were attached to transverse Pyrex sample holders (sample disk normal parallel to the direction of the vibration) with double sided tape. The sample was first measured as-cured to establish a base line. It was then strained in-plane parallel to

a reference line drawn on the surface an then re-measured with the field parallel to the reference line. The sample was then removed and stressed along the disk axis, to reset the sample, and to compare to the as-cast state. The sample was then heated to $100°$C for twenty minutes by placing the sample in boiling water. After the sample cooled to room temperature it was re-attached to the sample holder and measured, again with the field parallel to the reference line.

3.4 Results

3.4.1 Magnetization versus temperature

Figure 3-2 shows a typical magnetization versus temperature graph for a Ni–Mn–Ga sample measured at a low magnetic field. For the temperature range shown in the graph a hysteretic (first-order) transformation can be seen between $30°$C and $60°$C and then a non-hysteretic (second-order) transition at $94°$C. The hysteretic transformation corresponds to the martensite/austenite transformation, and the non-hysteretic transition corresponds to the Curie temperature. The martensite start (M_s), martensite finish (M_f), austenite start (A_s), austenite finish (A_f) and Curie temperature (T_c) are indicated in the graph. The cooling and heating rate was slow enough to avoid artifacts in the measurement due to thermal lag, as shown by the absence of hysteresis at T_c.

Table 3.1 summarizes the transition temperatures for the alloys used to fabricate the composites. Three kinds of powder were used to fabricate the composites; two were made by spark erosion in liquid argon (SE liq. Ar) and liquid nitrogen (SE liq. N_2) as the dielectric, and the third powder was made by mechanically crushing scraps of a single crystal of Ni–Mn–Ga made with high purity manganese (TL-10 powder). All the spark eroded powders used were made at the University of California San Diego.

Table 3.2 shows the composition of the of the alloys used in the composite samples.

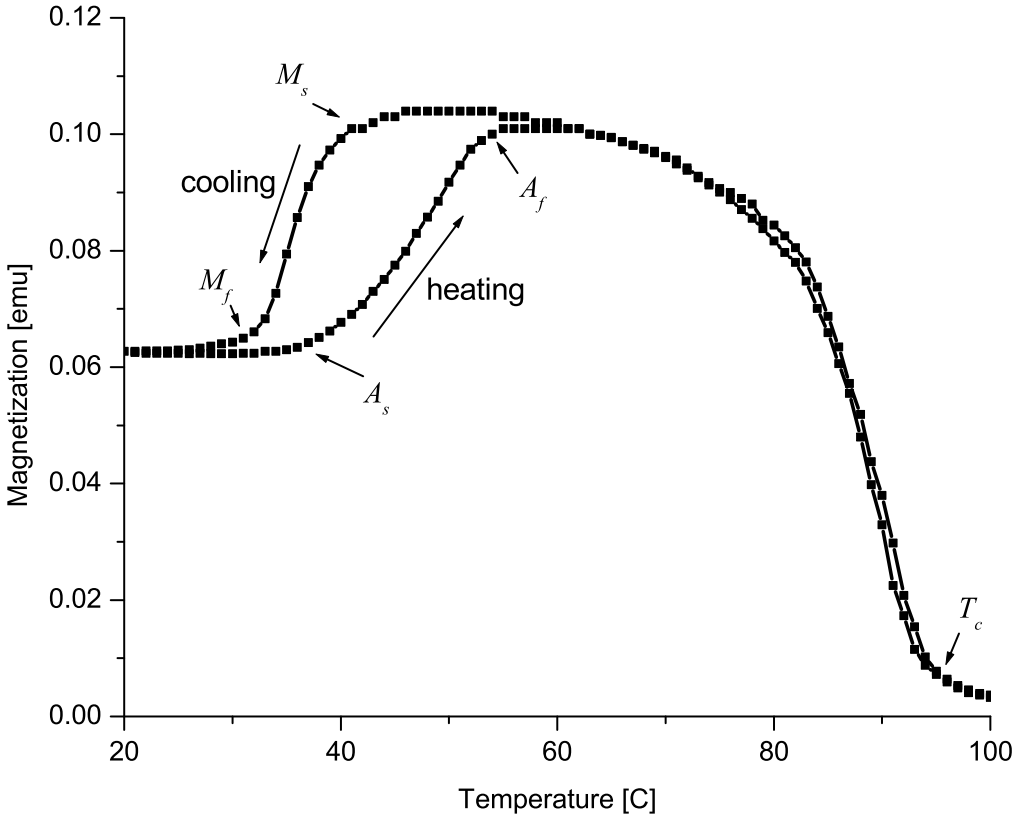

Figure 3-2: Magnetization vs. temperature for Ni–Mn–Ga spark eroded in liquid Ar, measured at 500 Oe.

Table 3.1: Transformation and Curie Temperatures for the alloys used in the composites.

Sample	$M_s(^\circ$ C)	$M_f(^\circ$ C)	$A_s(^\circ$ C)	$A_f(^\circ$ C)	$T_c(^\circ$ C)
SE liq. Ar	41	31	36	54	94
SE liq. N_2	40	24	26	36	80
TL-10 powder	33	29	38	44	100

3.4.2 Magnetization versus field

Figure 3-3 shows the change in the magnetization as a function of applied field for a 24 vol % Ni–Mn–Ga/polyurethane sample, for different prior in-plane strains. The field was applied parallel to the direction of the compressive stress. This figure only shows the positive quadrant of the graph, because the plot is symmetric about the origin and by only

Table 3.2: Composition in atomic % for the alloys used in the composites.

Sample	Ni at. %	Mn at. %	Ga at. %
SE liq. Ar	50.4	29.9	19.7
SE liq. N_2	48.6	30.2	21.2
TL-10 powder	50.2	29.0	20.8

showing a half loop the features can be seen more clearly. The trace labeled "FSMA 0 % in-plane strain" shows behavior corresponding to magnetization along the hard axis, it has the lowest susceptibility of all the loops shown in the plot. As the amount of strain on the sample is increased the initial susceptibility of the loops increases. The trace labeled "FSMA 26.4 % in-plane strain" has a noticeable higher susceptibility, and resembles more an easy-axis-of-magnetization behavior. The fact that the 26.4 %-strained sample does not show a more square loop with a higher susceptibility, reflects the demagnetizing effect of the spherical particles; $N = \frac{1}{3}$, $H_{int} = H_{ext} - NM$. The magnetization values at the highest magnetic field shown in the graph vary as a function of the strain on the composite, because the sample is not saturated at that field. This large susceptibility and magnetization at 3 kOe imply that the compressive stress increases the net fraction of variants having their c-axes parallel to the direction of the compressive stress. the fact that the stress-induced change in the sample shows up in the magnetization vs. field curve after the removal of the stress implies a magneto-plastic phenomenon. This is a hallmark of twin boundary motion.

Figure 3-4 shows the magnetization versus field for a 24 vol. % Terfenol-D composite control sample. Three different strains are presented: as cast (no strain applied), after being stressed out-of-plane, and after 26.4 % in-plane strain. The magnetization was measured along the same direction as the in-plane strain applied to to the sample. The three traces presented for this sample are essentially identical to each other. The maximum strain applied to the control sample is the same as the maximum strain applied to the composite sample in Figure 3-3. Terfenol-D is a material with a very large magnetostriction. Because magnetostriction is an elastic phenomenon any stress-induced changes are reprised upon removing the stress.

Figures 3-5, 3-6 and 3-7 are presented as a series, and they display the results of a sequence of stressing and heating cycles on a single sample. Figure 3-5 shows a half

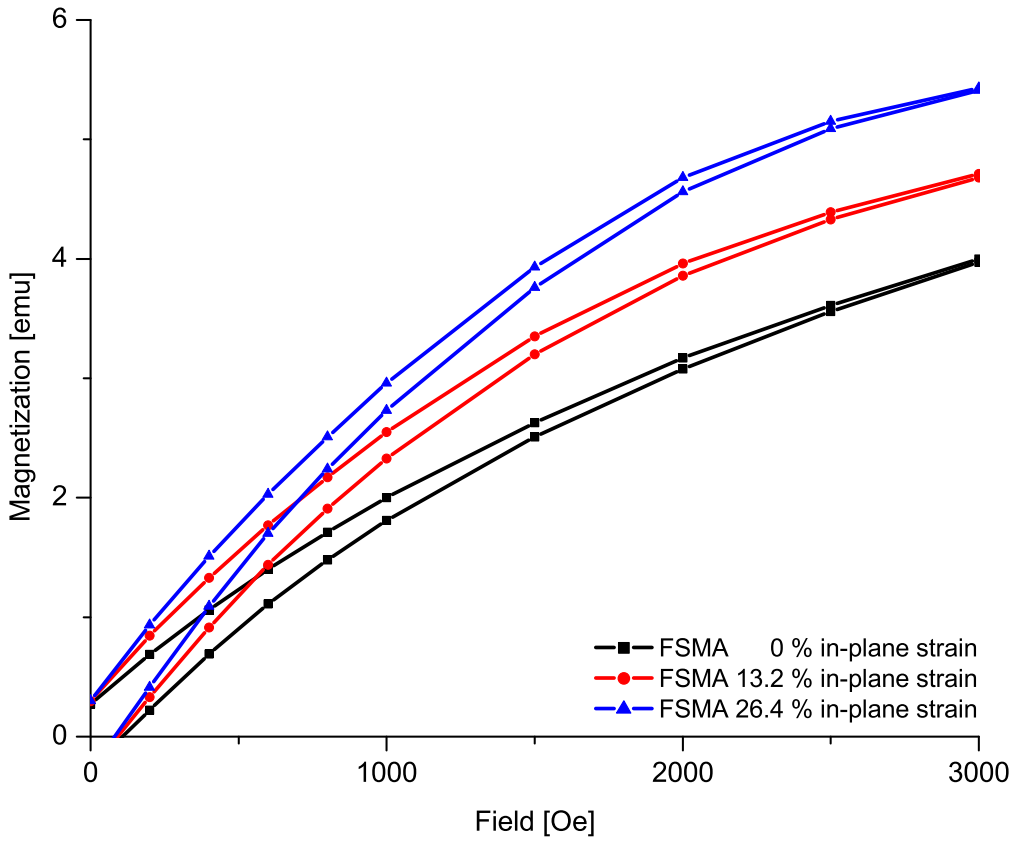

Figure 3-3: Magnetization vs. field for three different in-plane strains for Ni–Mn–Ga in Lord 7540A/B polyurethane.

magnetization loop for an FSMA/polymer composite measured with an in-plane magnetic field up to 10 kOe. The trace labeled “As cast” shows the composite sample before it was subjected to any stress treatment. The trace labeled “Stressed in-plane” shows the the same composite after being strained 26.4 % in the plane of the sample, along the same direction as the applied magnetic field used in the measurement. The graphs are similar to Figure 3-3, except the maximum field used here is larger. In this case the magnetization at 10 kOe is the same for the two traces. The as-cast composite again shows a hard-axis magnetization behavior that transitions into an easy axis type loop, as strain is applied along the direction of the measuring field.

Figure 3-6 shows the sample in the as-cast state and then after first being strained in-

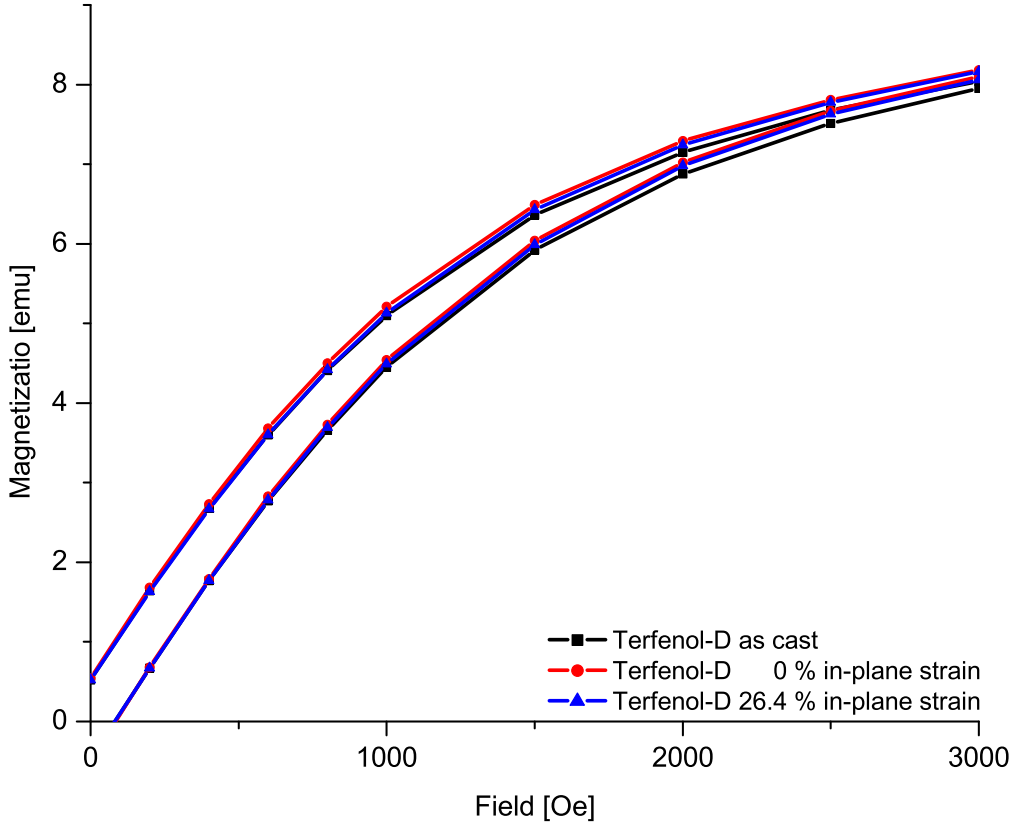

Figure 3-4: Magnetization vs. field for the as-cast and two different in-plane strains for Terfenol-D powder in Lord 7540A/B polyurethane.

plane to 26.4 % (as in Figure 3-5 and then stressed out-of-plane to reset the sample. The trace for the out of plane stress lies exactly over the trace for the as-cast sample, indicating the sample was fully reset from the higher susceptibility, stress induced state to the as-cast state.

Figure 3-7 shows the same two traces shown in Figure 3-5, and a third trace labeled " Self-accommodated variants." The extra loop corresponds to the composite sample measured after heating up to $100°C$, held at that temperature for 20 minutes and then cooled down to room temperature ($18°C$), before being measured in-plane along the same direction as when it was measured after an in-plane strain. The magnetization vs. field of the sample after heating lies half way between the sample as-cast and the sample strained in-

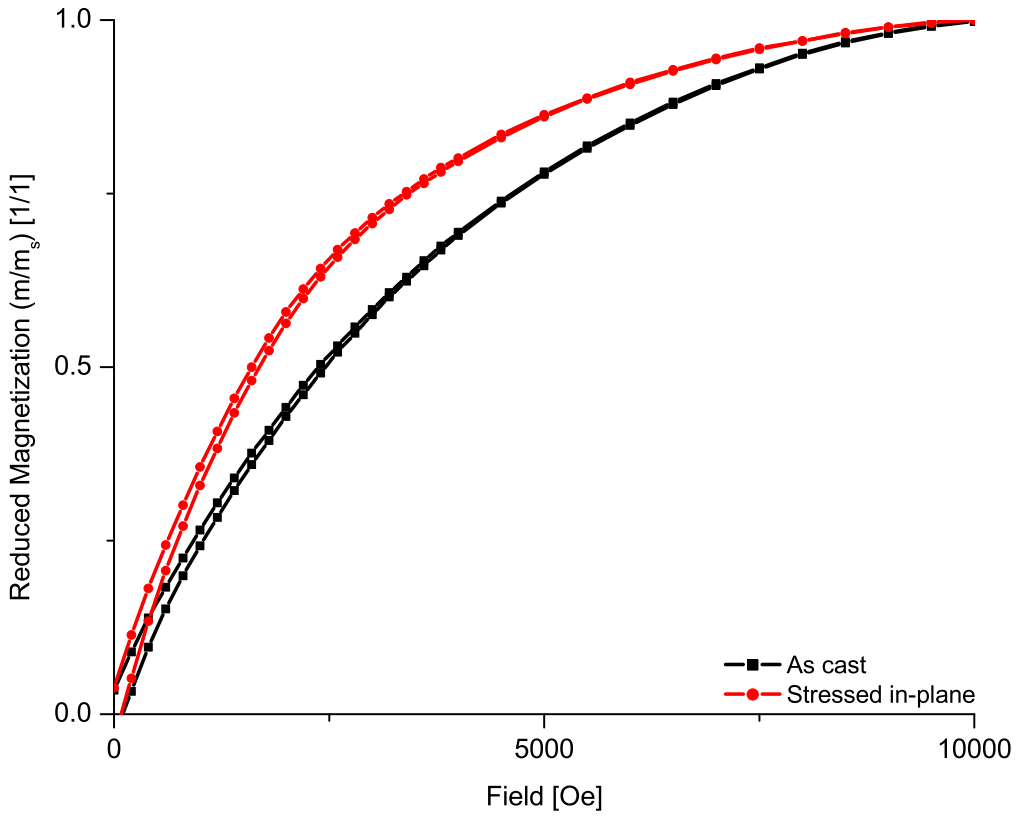

Figure 3-5: Magnetization vs. field for the as-cast and 26.4 % in-plane strain for Ni–Mn–Ga powder in Lord 7540A/B polyurethane up to 10 kOe.

plane. At 10 kOe the magnetization value for the sample in the three cases was the same. The composite, after being heated and measured, was stressed out of plane. This result is not shown, because it essentially duplicated Figure 3-6.

3.5 Discussion

3.5.1 Magnetization versus temperature

For the composites to exhibit stress-induced twin-variant reorientation, the Ni–Mn–Ga particles used in the composites must be martensitic at the test temperature. The results summarized in Table 3.1 show that the all the alloys used to make composite samples have

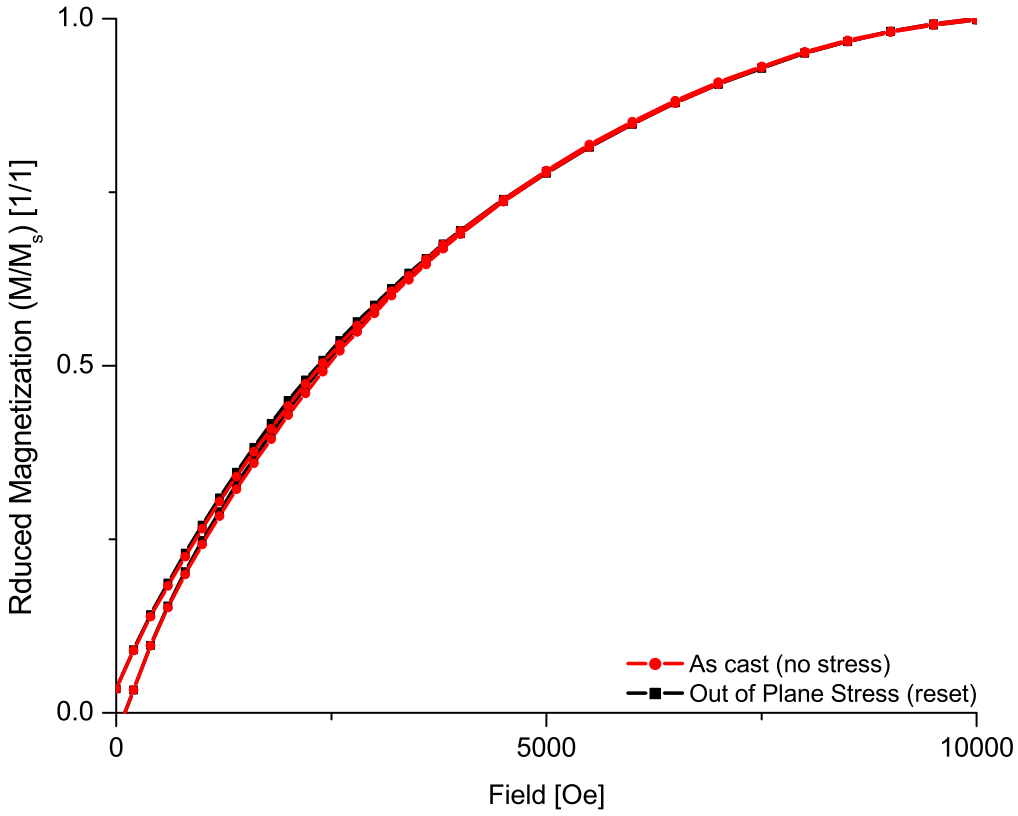

Figure 3-6: Magnetization vs. field for the as-cast and out-of-plane reset after being strained in-plane for Ni–Mn–Ga powder in Lord 7540A/B polyurethane.

martensite finish temperatures higher than room temperature ($20°\mathrm{C}$) This ensures that the alloys used had fully transformed into martensite at the test conditions.

The transformation temperatures and the Curie temperature play a very important role in the selection of the matrix material. Composites made of Terfenol-D, like the ones described in Chapter 1 use a heat cured-epoxy, that cures at at temperatures between $40°\mathrm{C}$ and $80°\mathrm{C}$, because of the ability to de-gas the slurry before curing and the stiffness of the epoxy after curing. At a first glance it would seem possible to use this type of matrix for the FSMA composites. Ni–Mn–Ga is still magnetic at the curing temperatures the epoxy requires, but is totaly or largely austenitic depending on the composition (see A_f) in Table 3.1. The magnetic field would align the particles in the composite and form chains. Particle chains parallel to the field minimize the magneto-static energy of the system, but because

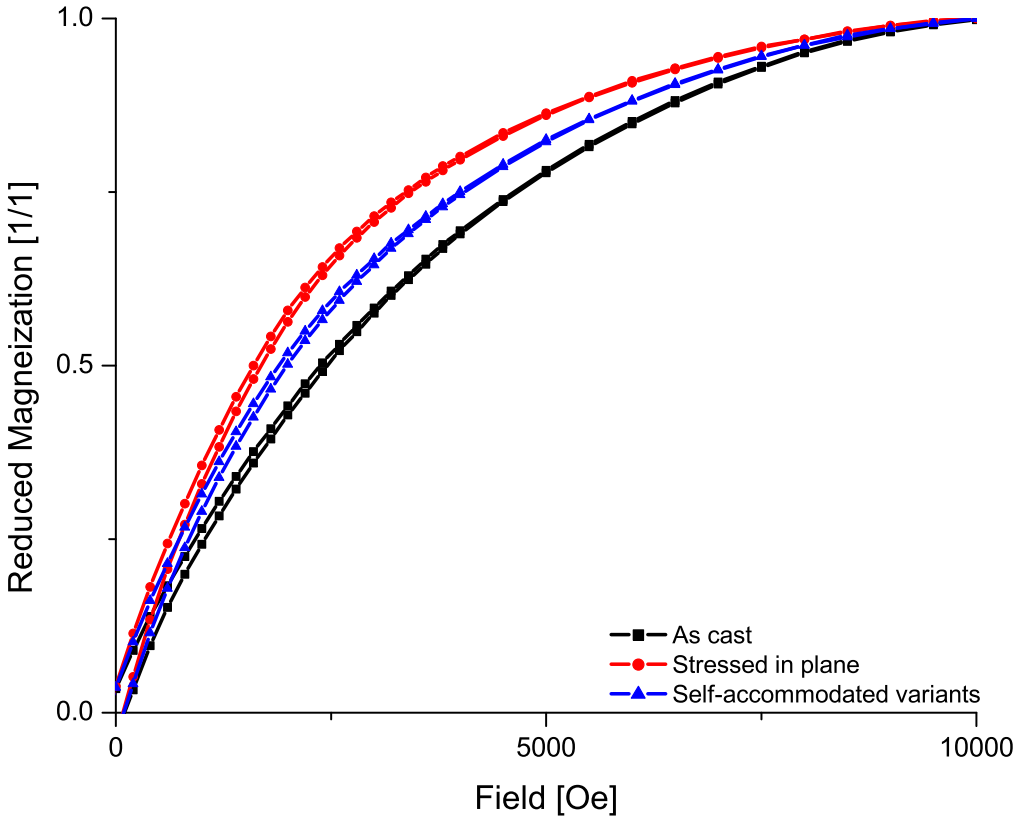

Figure 3-7: Magnetization vs. field for the as-cast, in-plane strained and after being heated to 100° C for Ni–Mn–Ga powder in Lord 7540A/B polyurethane.

the austenite does not have a unique crystallographic axis, the individual particles, though alligned in chains, would not orient with their easy axis parallel the field to yield a textured composite. The polymer matrix used has to cure below the austenite start temperature to obtain a textured composite with twin planes properly oriented to respond to an external stress.

3.5.2 Magnetization versus field

Figure 3-3 shows that an in-plane strain applied to the composites can re-orient the easy axis of magnetization from out-of-plane to in-plane. When the sample is measured in the as-cast state the easy axis of magnetization is along the particle-chain direction, pointing out of

plane. Since the measuring field is normal to the direction of the easy axis of magnetization, the loop has a relatively low initial slope, indicating a hard-axis direction. As the in-plane strain is applied to the composite, the initial susceptibility increases indicating that the easy axis of magnetization is rotating into the direction of the field. This occurs not by changing the alignment of the chains or physically rotating individual particles, because the polymer has cured and is solid. It occurs because in each individual particle, the variant whose c-axis (magnetic easy axis and compression-favored axis) is nearly parallel to the compression direction grows. The maximum field applied for these measurement was chosen to be lower than the field needed to cause the twin variant re-arrangement in single crystals of Ni–Mn–Ga, because of this, the value of the magnetization at 3000 Oe is an indication that the applied strain and not the applied field is rotating the easy axis into the plane. The fiber texture of the composite causes a high shape anisotropy along the particle-chain direction. The shape anisotropy of the composites is responsible for all the loops being sheared: the highest in-plane strain loop does not show the textbook square loop associated with an easy axis [4] for this reason. The very rounded approach to saturation is due to the large number of particles, with varying small degrees of misalignment with respect to the particle-chain axis.

The Terfenol-D composite control sample in Figure 3-4 shows no change in the susceptibility as a function of the applied strain. The control sample was loaded to the same volume fraction of filler as the Ni–Mn–Ga loaded sample. This shows that the effects observed are not due to anelasitc behavior of the matrix.

The data in Figures 3-3 and 3-4 support the data presented in Chapter 2 strongly suggesting that the direction of the easy axis of magnetization rotates into the direction of the applied compressive strain, indicating that the c-axis in the particles has rotated to coincide with the direction of the stress.

Figures 3-5, 3-6 and 3-7 together provide additional insight into the behavior of the as-cast composite sample. The data show that the composite as-cast in a field has a high degree of texturing. The application of an out-of-plane stress does not increase the initial susceptibility. The sample has twin variants that can be rearranged by the stress because the in-plane strain causes a significant change in the magnetization loop of the composite.

Figure 3-6 shows that the plastic change in the easy-axis direction can be fully reversed by application of an orthogonal reset stress. The loop for the as-cast composite and the loop for the composite first stressed in-plane and then out-of plane line up perfectly.

When the sample is heated above its austenite finish temperature and allowed to cool down below the martensite finish temperature, the magnetization loop of the composite falls halfway between the out-of-plane stressed sample and the in-plane stressed sample (Figure 3-7). The difference between the magnetization of the sample heated above its transformation temperature and the out-of-plane stressed sample is close to half (55%) of the magnetization difference between the out-of-plane and the in-plane strained composite. As the sample is heated above the transformation temperature and then allowed to cool and fully re-transform into martensite the transformation stresses in the particles are accommodated by forming roughly equal fractions of each variant. An equal number of variants in the particles in the composite would yield a net easy axis 45° away from the c-axis of either variant. This is consistent with the data observed in Figure 3-7. The difference in the magnetization loop as-cast and after being allowed to self accommodate shows that the Ni–Mn–Ga particles mixed with the polymer to form the composite were mostly single variant to begin with. Had the particles been equivariant when placed in the polymer the loop after heating would have fallen on top of the as-cast measurement. Also the matrix is not stiff enough to influence the distribution of variants in the composite as the particles accommodate the transformation stresses.

3.6 Conclusions

The results in this section show that the Ni–Mn–Ga powders used in the composites are in the right crystallographic phase at room temperature to yield active twin systems. The phase transition temperatures play an important role in the selection of the matrix material, because the matrix has to cure below the austenite start temperature. The transition temperatures also set the upper bound for the temperature range over which the composites can be used and still show the effects of twin-boundary motion under an applied stress. This will be discussed again in Chapter 5

The VSM measurements are consistent with the results obtained from torque measurements shown in Chapter 2. There is evidence of an anelastic re-arrangement of the easy axis of magnetization as a result of an applied stress. The change in the direction of the easy axis of magnetization is reversible and the magnetic easy axis tends to correspond to the axis of the applied compressive stress.

There is evidence that the particles in the composite are mostly single variant when the composite was cured. The initial texture in the composite is lost if the material is heated above the austenite finish temperature and the particles self-accommodate into an equivariant configuration.

Twin rearrangement is plastic under applied compressive strain (i.e. removal of the stress does not allow the twin structure to revert to its original form). However twin rearrangement can be essentially fully reversed by application of a compressive stress orthogonal to the prior stress.

In summary, no direct evidence of stress-induced or field-induced twin boundary motions has been shown here. However, every characteristic of plastic twin boundary motion, its threshold behavior, its erasure on entering the austenite and returning to the martensite phase is evident in the magnetic behavior of these composites. These characteristics of twin boundary motion would not be observed from magnetostriction, particle rotation or any other mechanism the investigator is aware of.

Chapter 4

Direct observations

The previous two Chapters presented indirect evidence of the mobility of twin boundaries in small Ni–Mn–Ga particles embedded in a polymer matrix. The techniques used in this Chapter give direct insight into the crystal structure, its orientation, and the morphology of the particles used in the composites. Powder x-ray diffraction patterns are directly related to the structure of the material, and can also give information about the sample texture. The scanning electron microscope (SEM) can image directly the particles used.

4.1 Experimental techniques and sample preparation

4.1.1 Powder x-ray diffraction

Powder x-ray diffraction (XRD) is a technique commonly used to determine the structure of solids and liquids. This measurement relies on scattering from a large number of crystallites at the same time. By having a large number of particles with a random orientation, the x-rays will reflect from all the crystal planes. If the sample is textured (i.e. certain crystallographic orientations occur more often than in the random case), peak-intensity differences with respect to the non-textured case will be observed and indicate which crystallite orientation is preferred in the composite.

The powder x-ray diffractometer measures the intensity of the x-rays reflected at different angles by the sample. The sample is rotated through an angle θ relative to the x-ray

beam and at the same time the detector rotates by twice the angle of the sample (2θ). The x-ray source generates monochromatic radiation by a high energy electron beam that excites characteristic core level transitions in the metal target. For the measurements described here, a Rigaku diffractometer with a copper target was used. The copper K_α line $\lambda = 1.54$ Å was selected using a silicon crystal monochromator.

Composite samples used for XRD were prepared by pre-weighing the Ni–Mn–Ga powder and the two parts of the polyurethane, Lord 7540 A/B. The weights were calculated to yield the desired volume fraction of filler in the composite. The filler and the two parts of the polymer were mixed at the same time. The fully mixed slurry was loaded into a two-part polytetrafluorethylene mold to form 1 mm thick sheets. The mold was placed in a 4 kG field while the polymer cured to texture the samples. Two different field orientations were used to make samples described in this section; some samples were cured the with the field out-of-plane, and others with the field in-plane. Once the polymer had fully cured, squares 1 cm on side were cut out of the sheets.

Samples used to determine the crystal structure of the Ni–Mn–Ga particles were made by covering the surface of a $1\ \mathrm{cm} \times 1\ \mathrm{cm}$ square section of a glass slide with a thin layer of epoxy adhesive. The epoxy on the surface was then randomly coated with Ni–Mn–Ga particles in the absence of a magnetic field. The epoxy was allowed to cure and the excess loose powder was cleaned form the surface.

4.1.2 Scanning electron microscopy

In a scanning electron microscope an electron beam is used to image the sample. The beam is rastered over the surface and the back-scattered or the secondary-emission electrons are detected. Back-scattered electrons contain information about the sample chemistry and the secondary electrons generate an image of the sample topography. The LEO 438VP SEM used for this experiments allows the measurements to be done in low vacuum mode (9 Pa) as opposed to the more conventional SEM pressure of 10^{-5} Pa. In low vacuum mode, the non-conductive composite samples could be measured without having to coat them, because the small amount of air in the chamber prevents the accumulation of surface

charges.

SEM was used to observe both composite samples and loose powders. The composite samples consisted of small slivers cut from the same composite sheets used for the XRD measurements, the small slivers were attached to the aluminum sample holder using double-sided conducting-graphite tape.

A section of a composite sheet was measured as-cast. The rest of the sheet was strained by the application of a compressive stress normal to the sheet plane. A thin section of the sheet was cut out of the middle. The freshly cut section of the sheet, containing the direction of the applied strain, was mounted so that it could be observed in the microscope.

The loose powders observed were simply sprinkled on the exposed surface of a piece of double-sided conducting-graphite tape that had been placed on the SEM aluminum sample holders.

4.1.3 Transmission electron microscopy

The high-resolution transmission electron micrograph images shown in this Chapter were taken at Arizona State University by Virgil Solomon and David Smith. The procedure used for preparing the samples and the measurement technique are detailed by Solomon [51, 52]

4.2 Results

4.2.1 X-ray diffraction

Figure 4-1 shows the x-ray diffraction pattern for the random distribution of two kinds of Ni–Mn–Ga spark eroded powders used to make composites. The particles are made by spark erosion using liquid argon as a dielectric (Figure 4-1 (a)) and liquid nitrogen (Figure 4-1 (b)). The peaks in the patterns are indexed in reference to the austenite unit cell. It can be seen that the patterns for both types of powders show peaks at the same angles. The relative intensities of the major peaks in the plot are the same for the two different alloys presented in Figure 4-1. Both patterns show a tetragonal splitting of the peaks for which h k and l are all even and $h + k + l = 4n$; this can be seen the clearest for the 220 peaks.

The pattern for the particles spark eroded in liquid nitrogen shows a small third peak labeled (220a) in the middle of the 220 peaks split peaks can be seen, convoluted with the (202) and (022) peak.

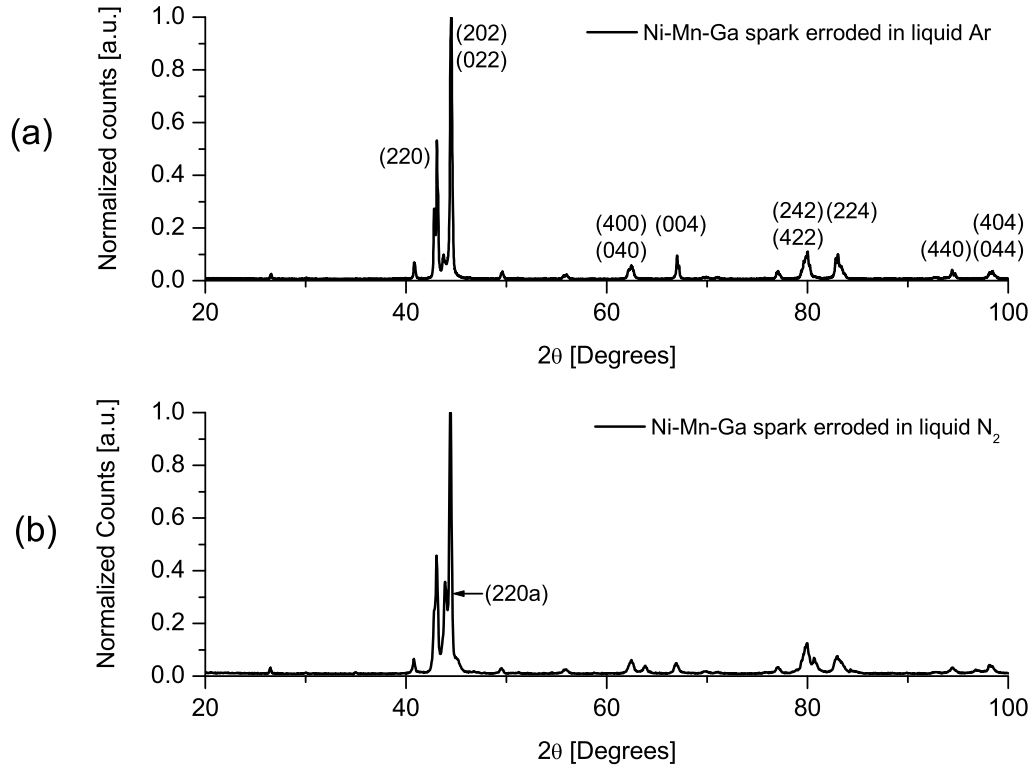

Figure 4-1: X-ray diffraction scans for Ni–Mn–Ga randomly sprinkled particles on epoxy with no magnetic field while curing, spark eroded in (a) liquid argon and (b) liquid nitrogen .

Figure 4-2 (a) shows the same diffraction pattern for particles of Ni–Mn–Ga spark eroded in liquid argon randomly oriented seen in Figure 4-1 (a) for comparison. Figure 4-2 (b) shows a 40 vol % composite of the same particles in Lord 7540 A/B, the composite was cured with the magnetic field applied *normal to the plane* of the sample. Figure 4-3 shows a schematic representation of the experimental geometry used for Figure 4-1. The composite sample (Figure 4-1 (b)) shows peaks at the same angles as the particles sprinkled on the glass slide (Figure 4-1 (a)), and does not show any additional peaks. On the other hand, a large difference is seen in the relative peak intensities when the two samples are compared.

The intensity of the (220) peak relative to the (202) and (022) peak in the composite is lower than in the randomly oriented particles. The difference in intensities is the most evident for the (400) peaks; the (004) peak shows a very drastic increase in intensity in the composite sample, showing an increase in intensity of about a factor of 6. The application of a magnetic field perpendicular to the sheet during curing is seen to increase the intensity of scattering from (*h k l*)crystal planes that intersect the sample normal ($l \neq 0$)

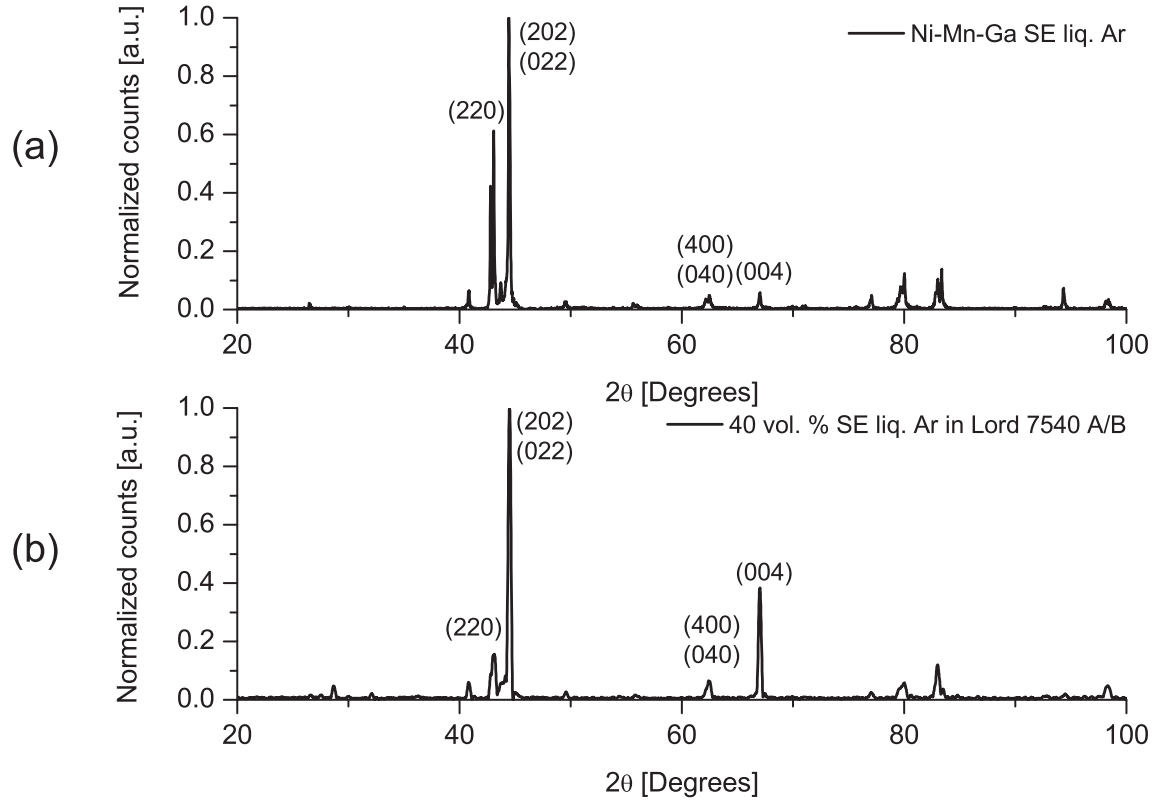

Figure 4-2: X-ray diffraction scans for (a) Ni–Mn–Ga particles spark eroded in liquid argon sprinkled on a glass slide with no field applied and (b) 40 vol % FSMA spark eroded in liquid argon oriented with an out-of-plane field in Lord 7540 A/B.

Figure 4-4 shows two diffraction patterns between $2\theta = 60^\circ \text{ and } 70^\circ$ for a 40 vol. % composite containing particles of Ni–Mn–Ga spark eroded in liquid Argon . This small range only covers the region where the 400 peaks are found. This sample was cured with the magnetic field *in the plane* of the sample. Figure 4-5 shows a schematic of the experimental geometry.

Figure 4-4 (a) shows the pattern for the composite as-cast; Figure 4-4 (b) shows the same sample after a large compressive strain normal to the particle-chain direction and

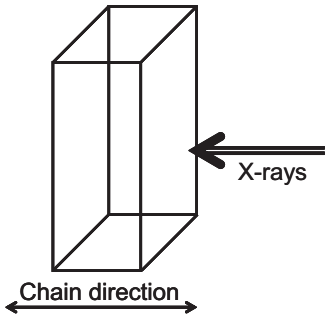

Figure 4-3: Schematic of the composite sample (rectangle) indicating the direction of the particle-chains and the incident x-rays.

parallel to the direction of the incident x-rays. The intensities of both plots were normalized to the intensity of the (400) and (040) peak. After the composite is stressed it shows an increase in the relative intensity of the (004) peak. The intensity of the (004) peak increases from about 50% to 70% of the (400) and (040) peak intensity. This indicates that compressive stress favors growth of twin variants having c-axes parallel to the stress axis.

4.2.2 Scanning electron microscopy

Figure 4-6 shows an SEM micrograph of Ni–Mn–Ga particles made by spark erosion in liquid nitrogen. In the image it can be seen that some of the particles are are hollow shells with very thin walls. This can be seen very clearly on the large particle on the right. The smaller particles around the large particle show openings too, revealing they are hollow. This type of hollow particles was mostly observed when liquid nitrogen was used as the dielectric. Only a very few particles made using liquid argon as the dielectric appeared hollow, while a large fraction were hollow when liquid nitrogen was used.

Figure 4-7 shows two scanning electron micrograph cross sections of a 40 vol. % Ni–Mn–Ga sample in Lord 7540 A/B polyurethane. Figure 4-7 (a) shows the composite as cured in a magnetic field applied in the plane of view, and shows the initial shape of the particles in the composite. Figure 4-7 (b) shows a cross section of the same composite after it was subjected to a compressive stress in the plane of the image, parallel to the field applied while curing. After the sample was stressed, a section of the composite was cut out

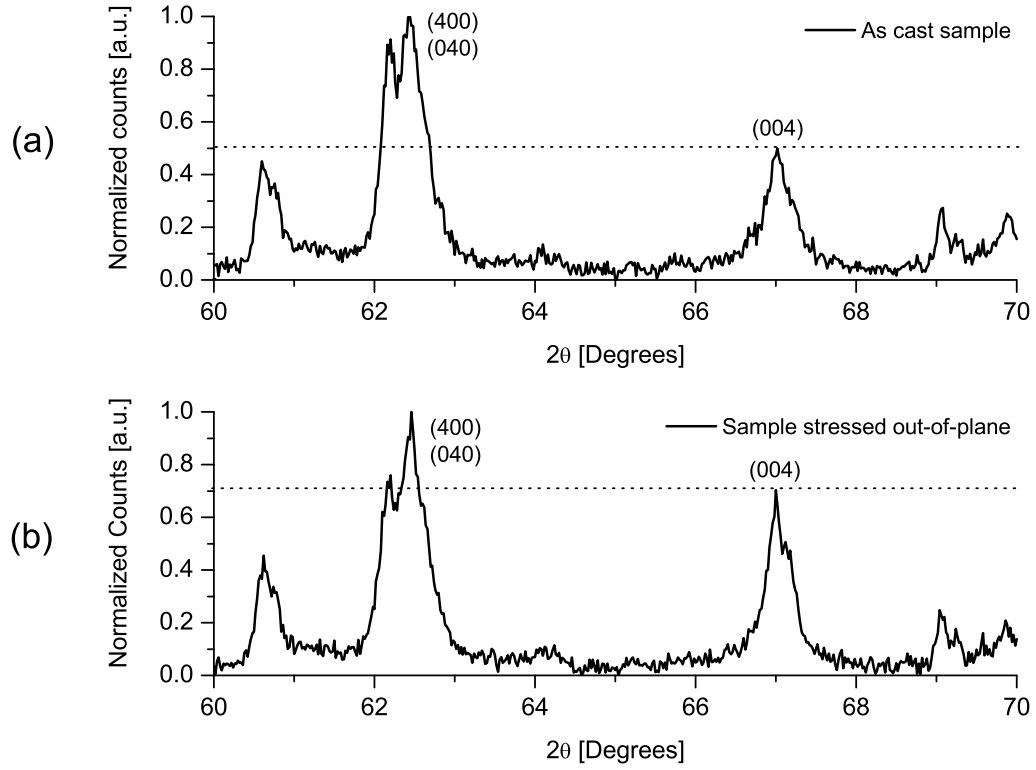

Figure 4-4: X-ray diffraction scans for (a) a 40 vol. % Ni–Mn–Ga spark eroded in liquid Argon in Lord 7540 A/B polyurethane as cast (no stain applied cured with an in-plane field and (b) the same composite after 12% out-of-plane compressive strain.

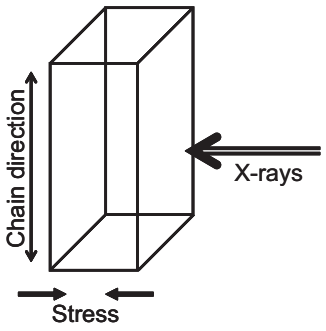

Figure 4-5: Schematic of the composite sample (rectangle) indicating the direction of the particle-chains, the incident x-rays, and the stress applied.

of the middle of the sample, with the thin section parallel to the particle chains. The image in 4-7 (b) corresponds to that center cut. Both images shown in the figure are very similar

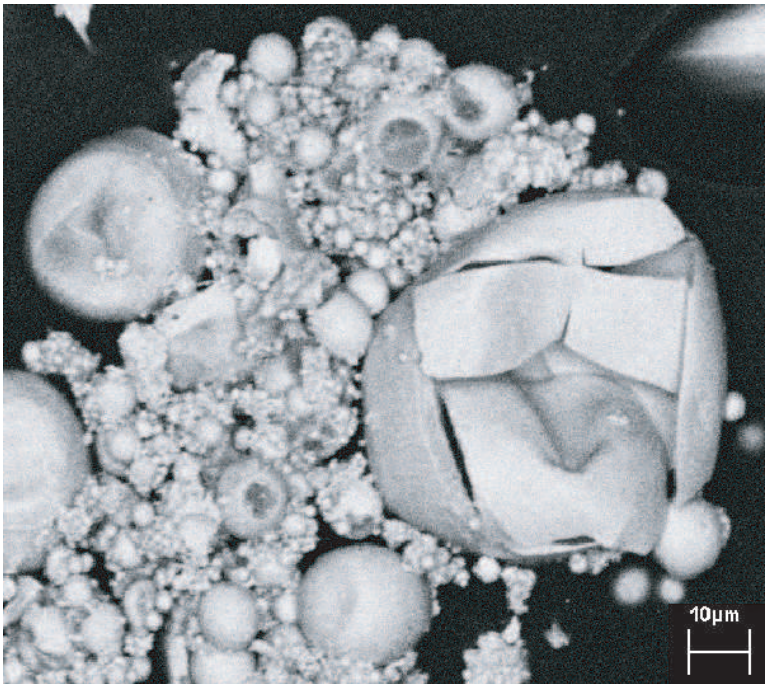

Figure 4-6: Scanning electron microscope micrograph of Ni–Mn–Ga spark eroded in liquid nitrogen.

and there does not seem to be any significant difference in the shape of the particles, or any gross displacement or delamination of the particles relative to the matrix. Thus, any changes due to the application of an external stress are probably due to changes inside the particles.

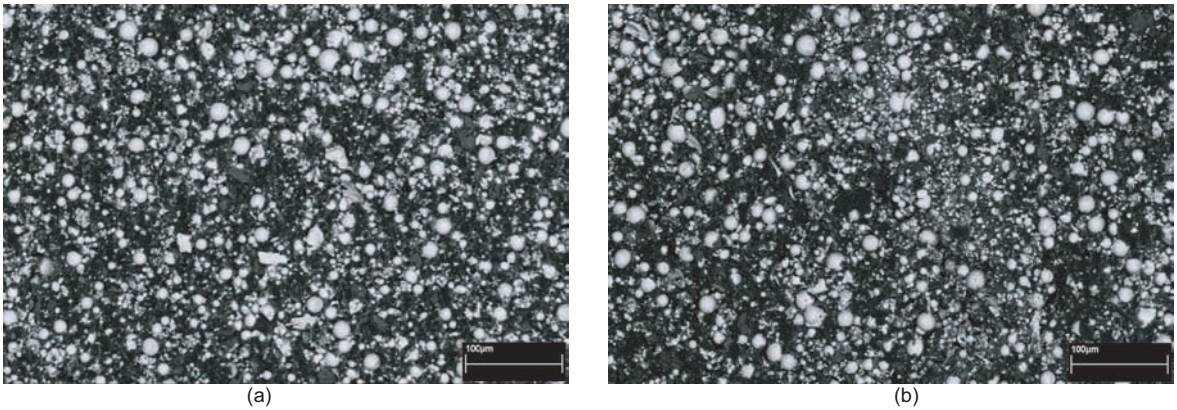

Figure 4-7: Scanning electron microscope micrograph of a Ni–Mn–Ga polymer composite as-cast cured with an out-of-plane field (a) and after being stressed compressibly out-of-plane (b).

4.2.3 High-resolution transmission electron microscopy

Figure 4-8 shows a high-resolution transmission electron micrograph of a particle of Ni–Mn–Ga spark eroded in liquid argon. The picture was taken at Arizona State University. There is no scale shown in the micrograph but the lattice fringes can be seen in the image. In the image a boundary can be seen crossing the middle of the frame horizontally. Black lines are superposed on the image to make the features easier to observe. Above and below that a herring-bone pattern can be seen, with light and dark fringes alternating from left to right in the image; the light and dark regions from a chevron pattern about the center line. The same change in direction observed across the center line is visible across the boundaries between lighter and darker regions. On the right of the image the edge of the particle is visible. Clearly the particles made by spark erosion in liquid argon are twinned and within the twins there is evidence of layering.

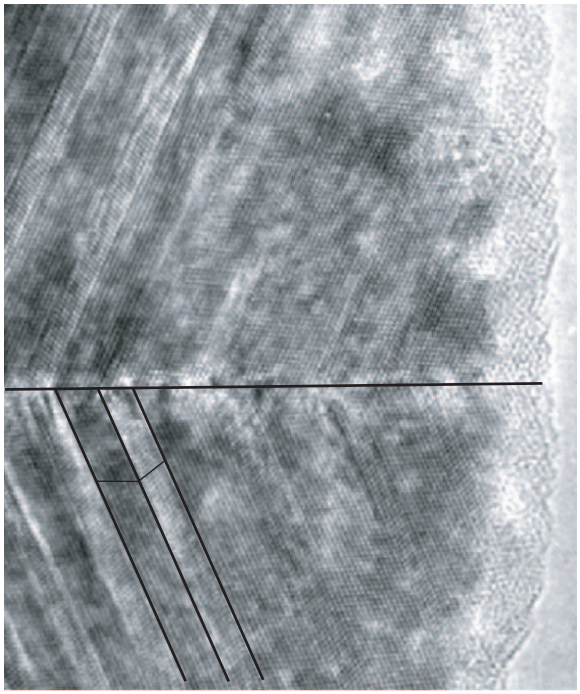

Figure 4-8: High-resolution transmission electron micrograph of Ni–Mn–Ga spark eroded in liquid Argon. Dark lines have been superimposed the image to emphasize the boundaries.

4.3 Discussion

4.3.1 X-ray diffraction

From figure 4-1 it can be seen that the particles sparked in liquid nitrogen and liquid argon have essentially the same crystal structure, because their diffraction patterns are nearly identical in terms of the peaks present or absent. However, the relative intensities of the peaks, particularly the $\{400\}$ set, show minor differences. These intensity differences may be due to differences in the texture or different chemical ordering in the particles. These diffraction patterns also show that the alloys used are martensitic at the temperature the samples were measured ($20°$C). The splitting in the $\{220\}$ and $\{400\}$ peaks shows that in these sets one of the axes is smaller than the other two, this is the case in the tetragonal martensite but not the cubic austenite.

The third peak seen in the liquid nitrogen powder pattern (e.g. 220a) corresponds to the austenite phase. There are two possible explanations for the austenite peaks; they could be due to retained austenite, or the composition variation from particle to particle could mean some of the particles are austenitic.

Figure 4-2 shows how a magnetic field applied to the sample as it is cured causes the particles to orient with their c-axis along the direction of the applied magnetic field: this can be seen most clearly in the dramatic increase in the intensity of the (004) peak. The relative amplitudes of the $\{220\}$ peaks also varies, the (202)/(022) peak shows a higher relative intensity in the composite sample than in the randomly oriented particles shown in Figure 4-2 (a). It is more obvious to interpret the $\{400\}$ peaks, because they correspond directly to the a-axes and the c-axis of the tetragonal Ni–Mn–Ga. The shorter c-axis has its reflection at the higher angle, and this is the peak that shows the marked increase in intensity. This inicates a high fraction of the c-axes pointing out of the plane of the sample in the composites. in the case of the $\{220\}$ set, the planes that intersect the c-axis (202) and (022) are spaced closer to the c-axis length than the planes that are parallel to the c-axes (220). Thus the intensities of diffraction lines from planes more nearly perpendicular to the c-axis scales more strongly.

The lack of additional peaks in Figure 4-2 (b) relative to Figure 4-2 (a) indicates that

the matrix did not add additional peaks to that would interfere with the measurement of the Ni–Mn–Ga particles.

Figure 4-4 shows a narrow scan over the region where the [400] peaks are found. The clear increase in the intensity of the (004) after the sample was stressed shows that the variant distribution of the particles was changed and the c-axes of the particles rotated into the direction of the applied stress. Plastic deformation of the particles or anelastic effects of the matrix that might have seemed like the plausible explanation for the results in the previous chapters do not explain the results observed in this figure. The as-cast sample (Figure 4-4 (a))does not show the large difference observed in Figure 4-2 (b), because the sample used in this measurement was cured with a field in the plane of the sample, and was measured with the scattering plane x-rays normal to that plane. This direction of field curing had to be used to ensure that the composite could be stressed normal to the direction of the c axis of the particles in the composite. (The samples were thin sheets and if one attempts to strain them in-plane they buckle and the load is not transferred to the particles.) In this sample geometry, the area over which the load is applied is much larger than in all the previous experiments, requiring a much larger force to obtain the same stress.

4.3.2 Scanning electron microscopy

Figure 4-6 shows something that was quite unexpected; Ni–Mn–Ga tends to form hollow spheres when spark eroded in liquid nitrogen. There is no clear explanation why the hollow particles form, Prof. Berkowitz form UCSD, who makes the particles, believes that they may be formed through some sort of self-assembly process, but there is no definitive mechanism for their formation. For vibrational energy absorption applications using composites. The solid particles obtained by spark erosion in liquid argon are a better choice.

In the previous two chapters it was suggested that the change in the magnetic anisotropy of the composite samples could be due to mechanical deformation of the particles. In those chapters this explanation was ruled out because if a sphere was plastically deformed by an uniaxial stress it would deform into an oblate spheroid. The resulting increase in anisotropy due to the shape change of the particles would be in the direction normal to the

applied compressive stress, but the increase in anisotropy was observed to be parallel to the direction of the stress. The incongruence between the expected direction of the easy axis of magnetization and the observed one, served as the main argument. The change in anisotropy observed in Figure 3-5 is approximately 22.5%. In order to account for that change the length-to-diameter ratio of the spherical ratio would have to change from 1 to nearly 2 [4]. Figure 4-7 shows a micrograph of the particles before and after a stress is applied to the composite. This micrographs shows that there is no deformation large enough on the particles to account for the change in magnetic anisotropy observed. They mostly maintain their spherical shape. This rules out deformation of the particles as the cause for the change in the anisotropy of the composites.

4.3.3 High-resolution transmission electron microscopy

The high-resolution transmission electron micrograph shown in Figure 4-8 shows the nano-scale structure of a particle like the ones used in the composites. The image shows the herringbone structure typical of twinned Ni–Mn–Ga [46]. This image helps lay to rest one of the key questions for this work. It shows there are twin boundaries in the particles used to make the composites. Twin boundaries have a surface energy associated to them. If the particles become small enough, the strain energy stored in the particle from the phase transformation will be smaller than that needed to form the twin boundary and the particle will not twin. This image shows that the particles are larger than this critical size.

The horizontal line in the image is a macro twin, while the other lines correspond to nano-twins. The nano-twins observed arise from the stacking of the atomic planes in the layered martensite, and apparently cannot be moved by a stress. Macro twins can be shifted by an applied stress. A description of the nano-twins is given by Pons [53].

4.4 Conclusions

The results in this Chapter confirm that the alloys used were martensitic at room temperature, consistent with the magnetization versus temperature measurement results shown in Chapter 3. This means that the material is in the right phase to exhibit twin boundaries.

Further the martensitic particles are twinned, as seen in the HRTEM images.

The texture due to the field applied during curing of the composites was directly observed via x-ray diffraction. This confirms the indirect observation of texture shown in Chapters 2 and 3. The texture of the samples is key for them to work as mechanical energy absorbers, because a large fraction of the twin boundaries in the composite will be properly oriented with respect to the load direction of the composite.

Direct XRD observations confirm the rearrangement of the crystal structure of the particles when a stress is applied to them. The short axis of the crystal rotates into the direction of the applied stress, as occures in single crystals of Ni–Mn–Ga, and confirms the torque and VSM measurements shown in the previous Chapters.

The SEM images show that the particles remain mostly spherical after the composites are stressed. The change in anisotropy is not a shape effect of the particles being plastically deformed. This increases the likelihood that stress is moving twin boundaries. Stress induced twin-boundary motion is confirmed here by XRD.

Chapter 5

Mechanical measurements

The data presented in this chapter marks a change in the pace of the thesis, up to this point the main focus was to prove that twin-boundaries in the particles embedded in the polymeric matrix could be moved by an applied load. This chapter focuses on the possibility of using FSMA/polymer composites as damping materials, because the motion of twin boundaries in the composite should dissipate a large amount of energy. This is done by quantifying the amount of energy dissipated by a composite subjected to a cyclic load. A custom test apparatus built for these measurements will be described and the results obtained with it will be presented.

5.1 Cyclic testing

Cyclic mechanical testing consists of subjecting a sample to a stress that is periodic in time, and recording the resulting strain. The response of the samples is characterized as a function of the frequency of the applied load. The temperature at which the test is conducted can be varied to determine how that parameter affects the sample response. Dynamic mechanical analyzers (DMAs) are commercially available instruments designed to do these measurements. A custom tester was built because the stress and strain range needed for these experiments was greater than what the available DMAs could cover.

5.1.1 Custom tester

The tester consists of a rigid aluminium test frame that holds the setup together and serves as a reference frame. The load on the sample is provided by an electromagnetic linear motor. The linear motor connects to the bottom grip assembly through a brass flexure, that ensures the load is uniaxial. The top of the sample is fixed to the reference frame, and the load on the sample is measured by a Transducer Techniques DSM–500 load cell. The load cell used is configured to work in tension and compression. The displacement of the bottom of the sample is measured at the bottom grip with an ADE 3800 capacitance gauge. The output of the the load cell conditioner and the capacitance gauge are connected to a National Instruments high-speed data acquisition card (DAQ) and a LabView program records the data out of the DAQ. Figure 5-1 shows the tester that was built.

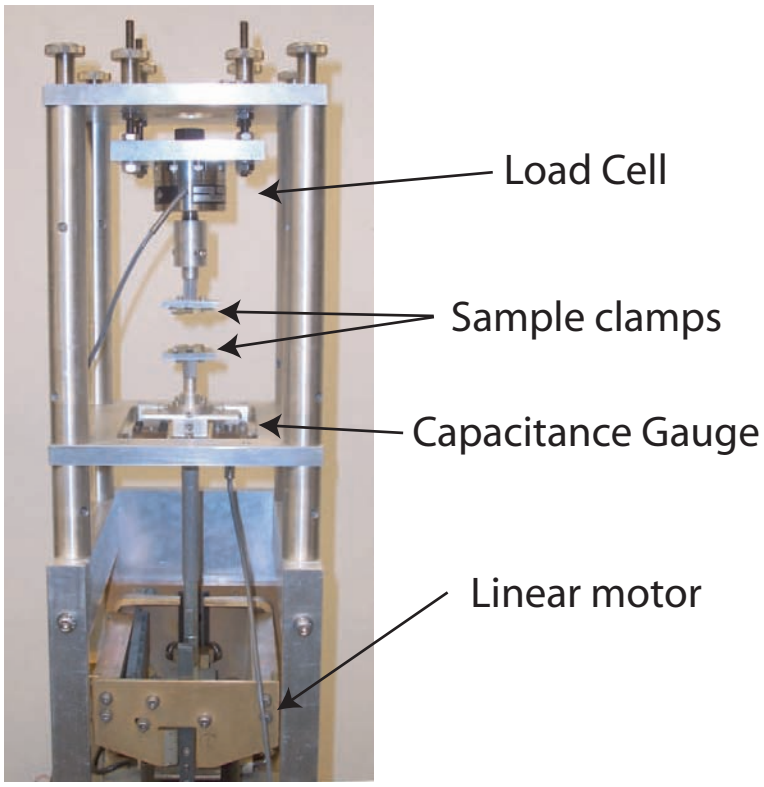

Figure 5-1: Schematic of the mechanical tester used.

The linear motor is driven by a Stanford Research Systems D345 signal generator, amplified by custom-built linear amplifier designed to drive inductive loads. In this configuration the tester is operated under load control. A cycle counter circuit box is connected

between the function generator and the power amplifier. The counter circuit box only allows a fixed number of cycles to pass, up to 16, in order to avoid overheating of the linear motor.

A temperature chamber was built to control the temperature of the sample. The chamber allowed the temperature to be controlled from room temperature to $55°\mathrm{C}$. The temperature chamber consists of an aluminium box with an open top and bottom. Two power resistors were attached to each of the sides of the box. The resistors were wired to match the impedance output of the power supply used. The output of the power supply was controlled by an Omega i Series temperature controller. The temperature was measured at the surface of the box by a thermocouple connected to the temperature controller. The surface temperature was used to control the chamber temperature. A fan inside the box ensured that the air temperature was uniform. The temperature chamber was separated from the test rig by insulating material and the top of the chamber was covered with a styrofoam cap. The temperature of the sample was monitored with a separate thermocouple.

5.1.2 Sample grips

One of the main problems encountered in this work was holding the composite samples in place in the tester. In its first iteration the samples were glued to an aluminium disk which was held in place with four screws pinching it from the side. By using glue the sample would not be subjected to any stresses other than the uniaxial load used to excite the sample for the measurement.

Several glues were tested to attach the samples to the aluminium disks, ranging from common cyanoacrylate to specialty acrylic adhesives. It was not possible to achieve a consistent bond between the samples and the aluminium, and the bond would sometimes break at very low loads. Given the the lack of consistency holding the samples an alternative to the attachment method had to be found.

The next attempt at holding the samples involved the use of a mechanical clamping force, which proved to be more successful than the use of an adhesive to hold the sample. Miniature clamps were made to secure the samples to the tester. The clamps were designed

so that the clamping area would be minimal; the clamp faces gripping the sample ends extended only 1 mm along the sample length. The first clamps used were made of steel. The high stiffness of the steel compared to the sample ensures the deformation registered is on the sample and not the clamps. It was later found that the steel used was magnetic and would interfere with some of the planed experiments. The second set of clamps used was made of brass so they would be non-magnetic.

The clamping force used could cause a stress state on the sample which would interfere with the measurement. To better understand the effect of the clamping forces on the stress state of the sample, the system was modeled using the ProEngineer® finite-element package. Figure 5-2 shows one of the results of the modeling. As can be seen, the region affected by the clamps was was more than 25% of the sample length at the ends. The uniform color in the middle section shows that the stress in 40–50% of the sample is uniform.

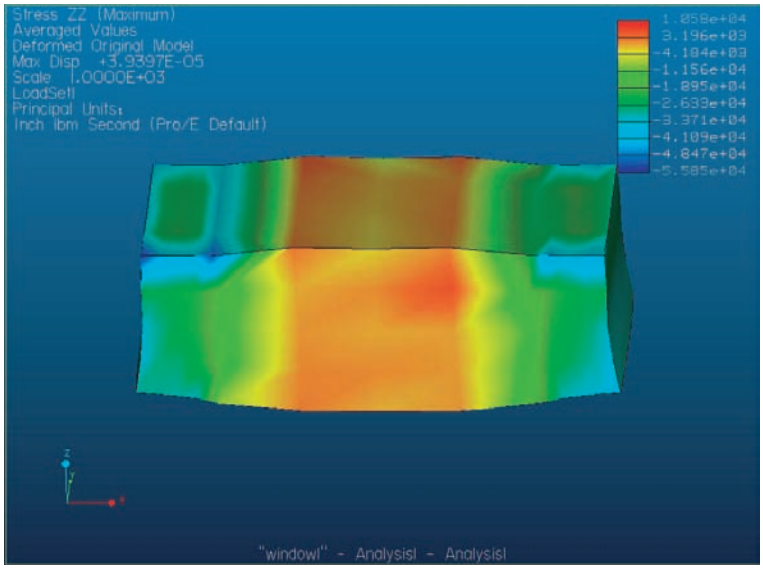

Figure 5-2: Finite-element simulation of the clamping force on the mechanical testing samples.

Clamping the sample directly proved not to be an ideal solution. When the sample was subjected to a tensile strain the sample cross section would contract, enough that the clamping force would be reduced to the point it could no longer hold the sample. The solution to this problem was to cast the samples with dovetail fittings into two end pieces of aluminium (Figure 5-3). In this way the sample could be gripped at the aluminium

rather than the polymer. The polymer would mechanically lock into the aluminium end caps preventing it from slipping out.

5.2 Sample preparation

The samples used for mechanical testing were made by mixing the filler material and the two parts of the polymer matrix in the desired proportions. A mold was then filled with the slurry and allowed to cure under a 4 kOe field applied parallel to the sample length.

Two types of molds were used to make the samples. The initial samples were made in a three-part teflon mold. The samples were rectangular prisms 5 mm$\times$5 mm$\times$15 mm. The samples used in the later experiments were made by placing the two aluminium end caps in a teflon mold. The central cavity of the mold was 5 mm$\times$5 mm$\times$15 mm. Figure 5-3 shows an image of the samples.

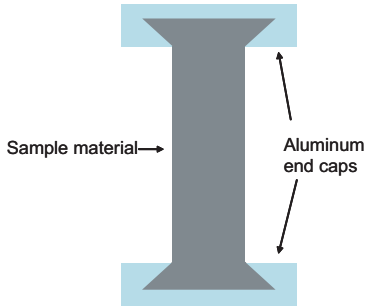

Figure 5-3: Schematic of the sample cast into the aluminium end caps.

Three kinds of samples were made for this experiments: 1) Ni–Mn–Ga particles in Lord 7540 A/B, 2) a control sample made of Iron particles in Lord 7540 A/B, and 3) a control sample of the Lord 7540 A/B with no filler. For the FSMA and the iron-loaded samples, the magnetic field was applied along the long direction of the rectangular section while the polymer cured.

5.3 Experimental setup

The procedure used to measure the samples was the following; the sample was first secured to the lower clamp. The upper clamp was then lowered on to the top of the sample and secured to ensure that the sample was directly in-line with the load path. If the sample was not straight, the upper clamp position was adjusted using the four screws on the top. After securing the sample, all screws in the system were tightened, to eliminate any slack in the system that could interfere with the measurement. The position of the capacitance gauge was then adjusted so that the output would be zero at the start of the test.

The desired number of cycles to be measured was selected on the counter box. The frequency and amplitude were selected on the function generator. The data acquisition program that records the data from the DAQ was started and the function generator was triggered.

For the temperature-dependent measurements the same procedure was followed as before, but before the data were acquired the temperature chamber was placed around the sample. The desired temperature was programmed on the controller. Once the controller indicated that the temperature had been reached, the sample was allowed to soak for half an hour at temperature to ensure the sample had reached thermal equilibrium. At that point the sample temperature was recorded with the thermocouple placed inside the chamber next to the sample.

In all cases, once the data were collected, a Mathematica script was used to analyze the data and calculate the loss ratio. The script numerically integrated the load and unload paths and the loss ratio was calculated from that. The full script used is presented in Appendix B. The definition of the loss ratio can be found in Chapter 1.

5.4 Results

5.4.1 Room-temperature measurements

Figure 5-4 shows a cyclic stress-versus-strain plot for the Lord 7540 A/B polyurethane with no additional fillers. Two different maximum applied loads are presented on the graph; the

shape of the loops does not vary with the maximum stress applied to the samples. The loops are elliptical and the area contained in them is fairly small. No unique features are evident in the loops. The slope of the loop indicates that the modulus of the Lord 7540 polyurethane is 1.6 GPa.

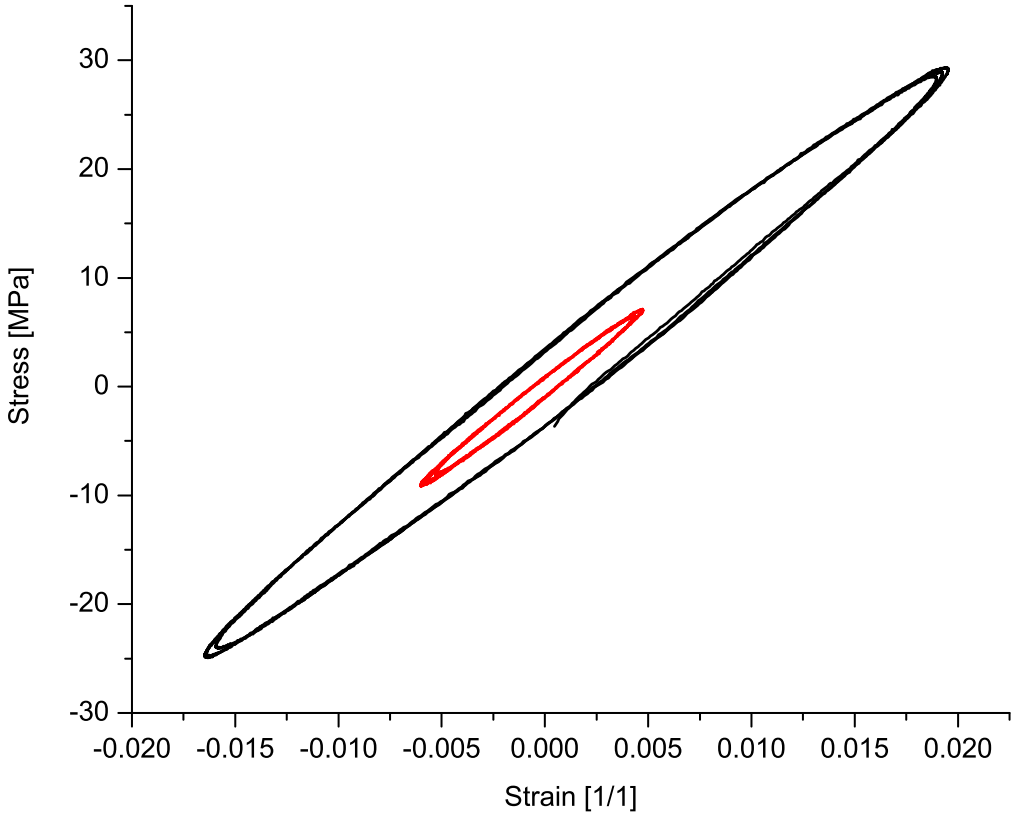

Figure 5-4: Cyclic Stress versus Strain for pure lord 7540 A/B polyurethane at 1 Hz for two different stress levels.

Figure 5-5 shows the cyclic stress versus strain behavior for a 20 vol. % FSMA in Lord 7540 A/B polyurethane matrix, for two different stress levels. Unlike the matrix material by itself, there is a marked difference in the shape of the loops as a function of the applied stress. When the composite is subjected to the lower stress the shape of the loop is elliptical, but shows quite a large hysteresis. At the larger stress amplitudes the loop departs significantly from the ellipticity seen at lower stresses. A flat region develops at the top of the graph and a marked inflection is seen at the central bottom part of the loop. In

the plot six full tension and compression cycles are presented. All six cycles superimpose each other on the graph within experimental error. The Slope of the major axis suggests an average modulus of 1.5 GPa without the flat portions and 0.67 if the flat portions are included.

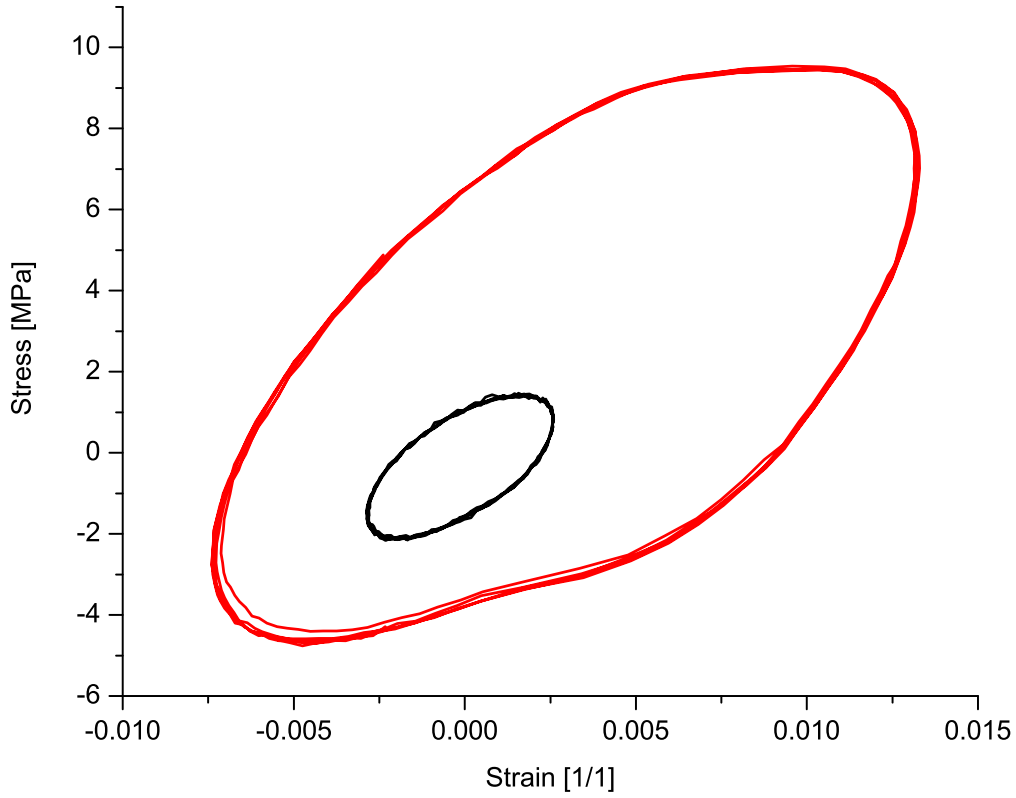

Figure 5-5: Cyclic Stress versus Strain for 20 vol. % FSMA in lord 7540 A/B polyurethane at 1 Hz for two different stress levels.

Figure 5-6 shows the strain and the stress traces as a function of time for the higher amplitude plot shown in Figure 5-5. The trace for the stress is sinusoidal, while the trace for the strain is a distorted sinusoid. It can be seen that the strain lags the stress in the plot.

The shape of the loops for the iron powder loaded samples (Figure 5-7) showed the same stress dependence as the polyurethane samples. The loops remained elliptical for all the stress amplitudes. The loops showed an intermediate hysteresis when compared to the Ni–Mn–Ga loaded samples and the pure matrix material.

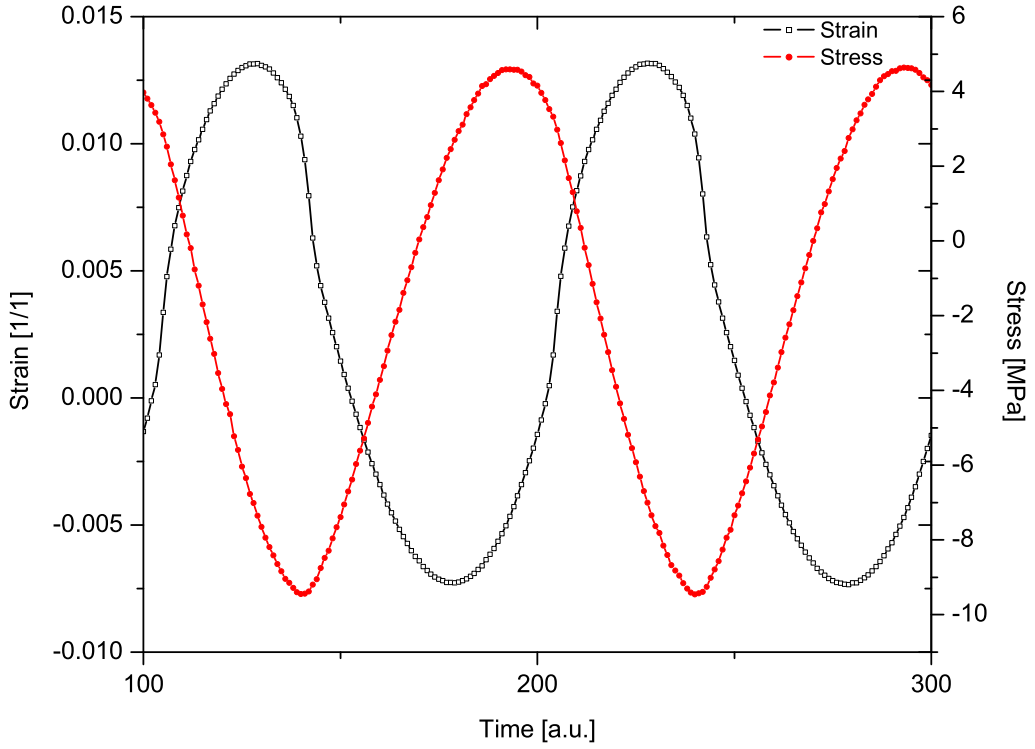

Figure 5-6: Stress vs. time and Strain vs. time plots for the large stress amplitude trace in Figure 5-5.

Table 5.1 shows a comparison of the loss ratios for the three kinds of samples used: the two control samples and the FSMA loaded samples. The table includes the loss ratio for all the materials, the value of the $\tan\delta$ and the maximum applied stress. The values reported for $\tan\delta$ are obtained by fitting the data obtained to Equations 1.3 and 1.4 and with the value of from the fit, $\tan\delta$ was calculated. It can bee seen that even though the polyurethane was taken to the highest peak-to-peak stress it also showed the lowest loss ratio. The lowest loss ratio reported for the FSMA loaded composites is higher than the loss in all the control samples.

For the non-elliptical FSMA composites, the value of $\tan\delta$ corresponds to the best fitting ellipse, but the area of the loop did not match the area of the ellipse. This implies that the value of the $\tan\delta$ reported has a large associated error .

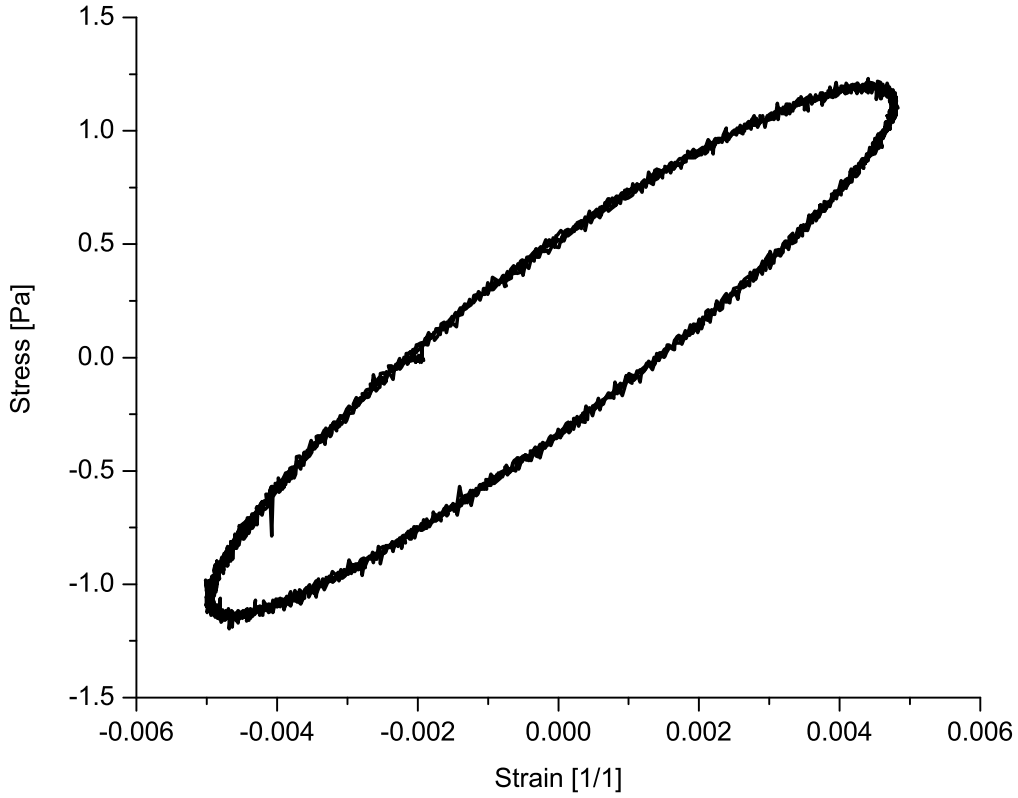

Figure 5-7: Cyclic Stress versus Strain for 20 vol. % Fe powder in lord 7540 A/B polyurethane at 1 Hz.

5.4.2 Temperature dependent measurements.

Figure 5-8 presents the loss ratio for a 20 vol. % sample of Ni–Mn–Ga and a pure Lord 7540 A/B polyurethane sample as a function of temperature. The peak-to-peak stress on the samples was constant at 6.6 MPa for all temperatures presented on the plot. The behavior of the two samples is quite different. The FSMA-loaded sample starts at a high value and as the temperature is increased the loss ratio decreases. The pure matrix material on the other hand has a loss ratio that initially increases as the temperature is increased, but peaks at about 35°C. As the temperature is increased beyond the peak the loss ratio for the polyurethane matrix decreases.

Figure 5-9 shows the loss ratio as a function of the stress amplitude for the pure polyurethane and for the FSMA-loaded composite at 22°C. The loss ratio for the pure

Table 5.1: Maximum stress, loss ratio and $\tan\delta$ for the two control samples and the FSMA loaded sample.

Sample	Max. stress [MPa]	Loss ratio [%]	$\tan\delta$
Polyurethane (Lord 7540 A/B)	17	17	0.1196
Fe 20 vol. %/Lord 7540 A/B	10	43	0.7376
FSMA 20 vol. %/Lord 7540 A/B	1.5	63	1.0296
FSMA 20 vol. %/Lord 7540 A/B	10	67	1.1383
FSMA 20 vol. %/Lord 7540 A/B	16	77	1.1616

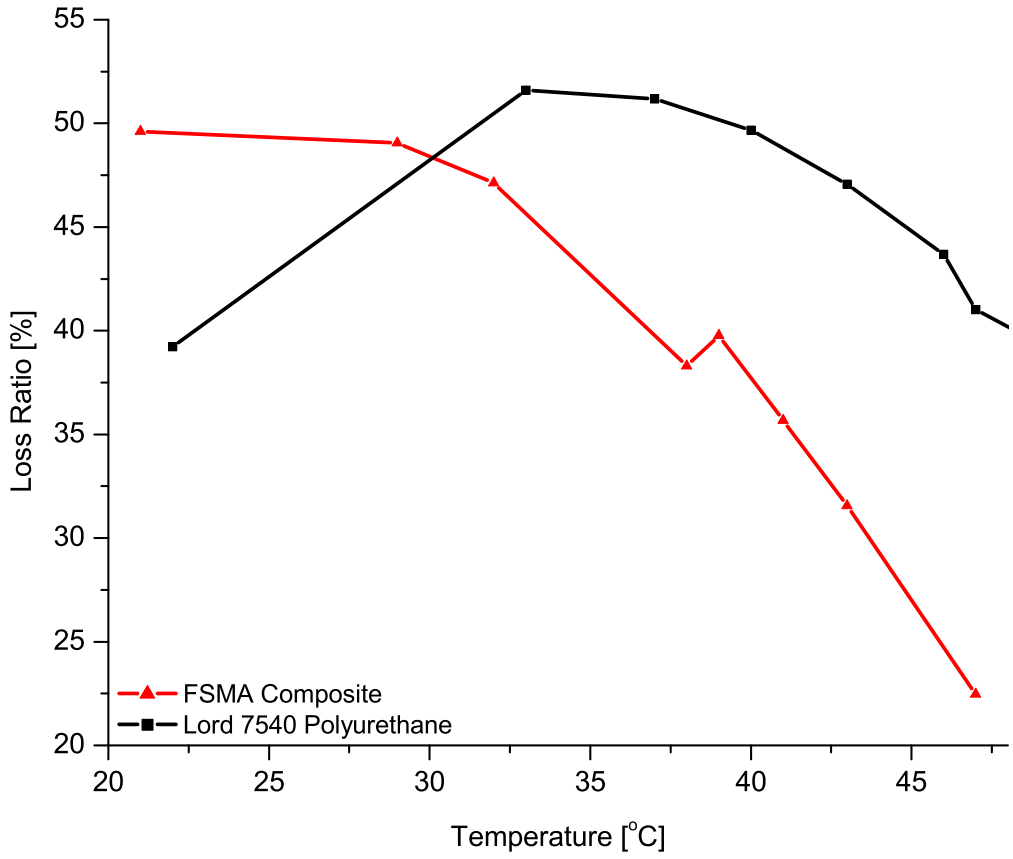

Figure 5-8: Loss ratio as a function of temperature for a Lord 7540 A/B sample and 20 vol. % FSMA in Lord 7540 A/B.

polyurethane is practically independent of the magnitude of the applied stress. The loss ratio for the FSMA loaded sample shows a strong dependance on the magnitude of the applied stress, increasing as the stress is increased. The loss for the FSMA loaded sample

is higher than the loss for the pure polyurethane at all stress amplitudes.

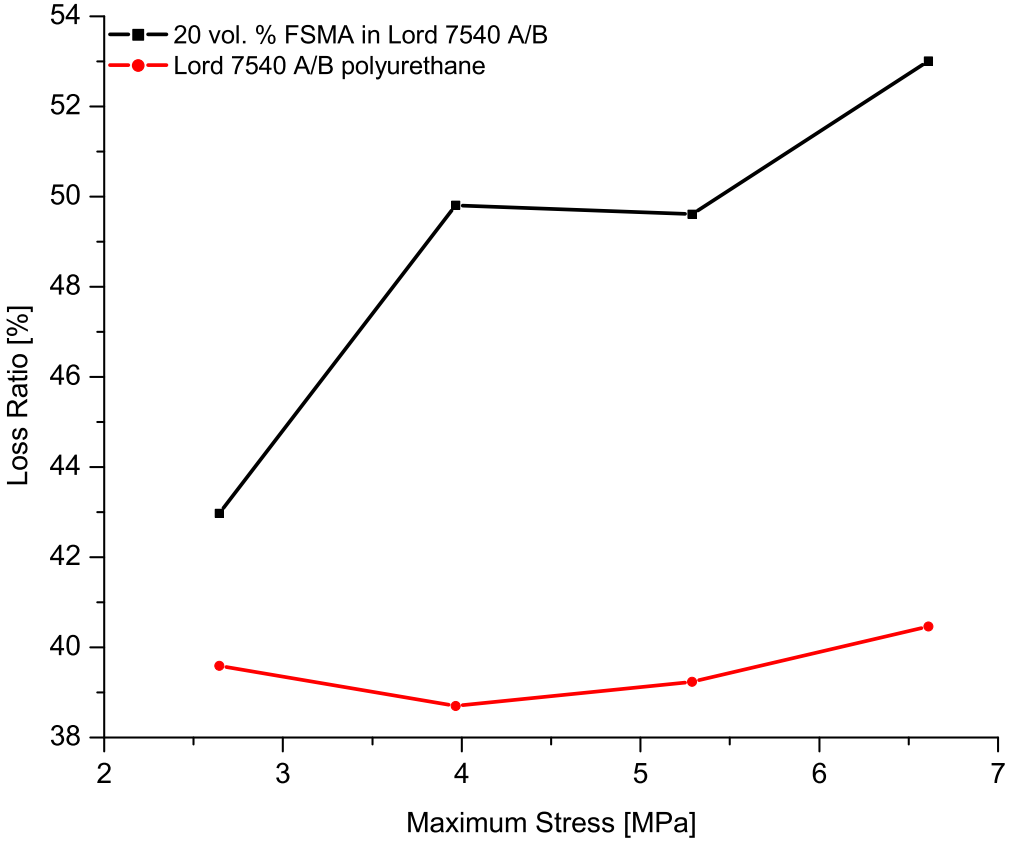

Figure 5-9: Loss ratio as a function of stress for a Lord 7540 A/B sample and 20 vol. % FSMA in Lord 7540 A/B at 22°C.

Figure 5-10 shows the loss ratio as a function of the applied stress at 47°C for the same samples shown in Figures 5-8 and 5-9. At this temperature both samples show a loss ratio that is mostly independent from the magnitude of the applied stress. In this Figure, the composite sample shows a lower loss ratio than the pure polyurethane sample.

Figure 5-11 shows a differential scanning calorimeter plot on heating for the two samples presented in Figures 5-8 – 5-10. In both traces a second-order transition can be seen in the range of -20°C to 30°C and in the FSMA loaded composite a first-order transformation peak can be seen between 40°C to 60°C.

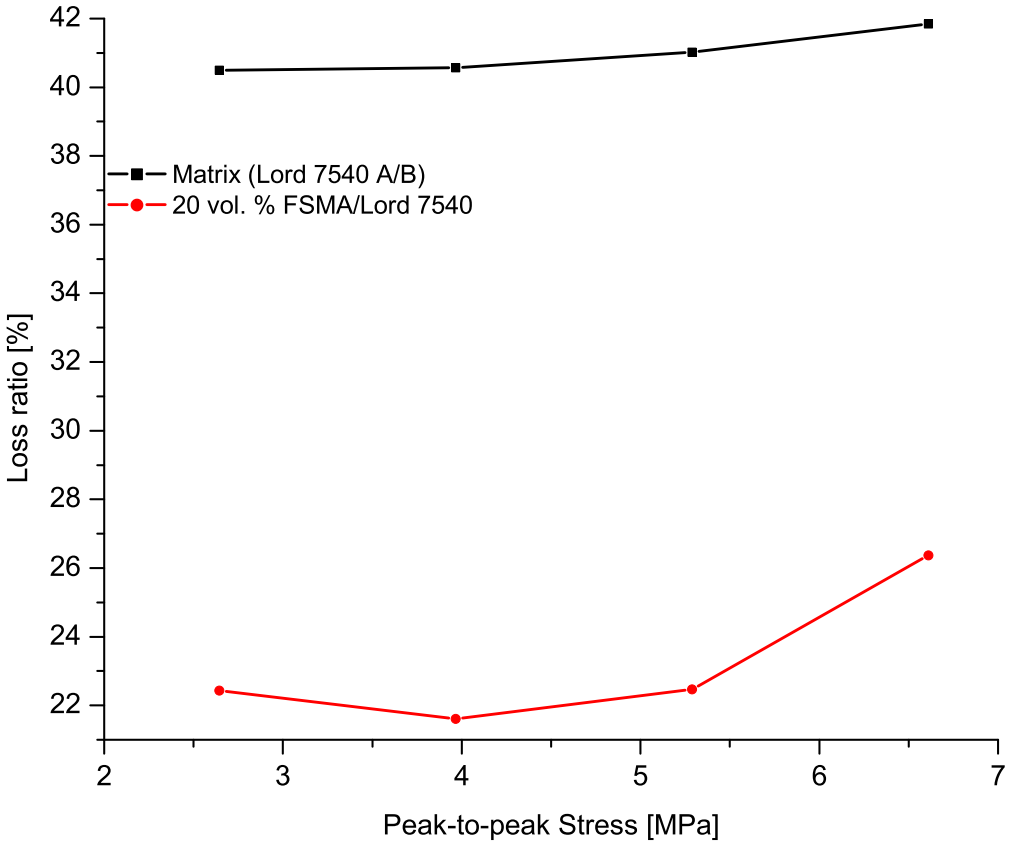

Figure 5-10: Loss ratio as a function of stress for a Lord 7540 A/B sample and 20 vol. % FSMA in Lord 7540 A/B at 47°C.

5.5 Discussion

5.5.1 Room-temperature measurements

Figure 5-4 shows the contribution of the matrix to the loss ratio of the composite. The shape of the loops does not change as a function of the peak-to-peak stress applied to the composite, this implies that the response of the material is linear. The same behavior was observed with the iron filled samples. The FSMA sample shown in Figure 5-5 shows a large change of the general shape of the loop as the amplitude of the stress imposed on the sample is increased. The strain of the composite is no longer a simple sine wave that lags the stress. The shape of the strain wave is highly distorted as it can be seen in Figure

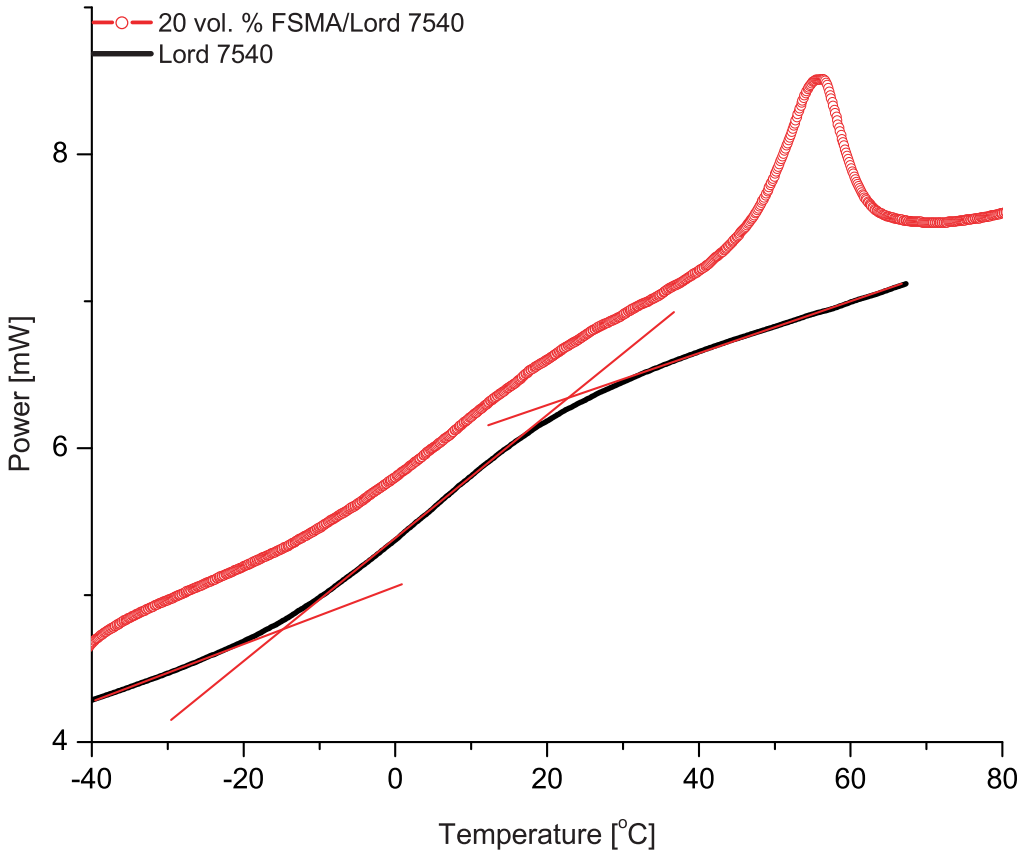

Figure 5-11: Differential scanning calorimeter scan for a pure Lord 7540 A/B sample and 20 vol. % FSMA in Lord 7540 A/B on heating.

5-6. The shape of the stress-strain loop is reminiscent of the stress-strain loops presented by Gans [36] for a single crystal of Ni–Mn–Ga in a full cycle of tension and compression. The loop shows a flat region on top and another, smaller, flat region near the bottom middle of the loop.

All the loops presented in Figures 5-4 and 5-5 consist of six full cycles plotted superimposed for each sample. In all cases they overlay each other quite well and almost no drift is observed. This indicates that the loss is most likely not an artifact of the particles delaminating, since it would diminish with each succeeding cycle and the loops would not overlap. The flat (low effective modulus) features in the loops are only observed in the Ni–Mn–Ga loaded samples and not in any of the control samples. This is a strong indication

that the additional loss mechanism is related to the FSMA particles.

Table 5.1 compares the loss in the different samples. The pure polyurethane sample shows the lowest loss ratio. The addition of iron increases the amount of energy dissipated, but the loops remain elliptical. As discussed by Feuchtwanger [42] the increase in the loss ratio for the iron-loaded sample could be simply due to the increase in the density of the material or dissipative mechanism at the particle-matrix interface.

For the FSMA loaded samples there is a clear increase in the loss ratio as a function of the amplitude of the applied stress, suggesting that the additional loss mechanism responsible for the increase in energy dissipated is stress dependent. This extra loss is consistent with the twin-boundary motion being responsible for the added loss in the composite material.

The use of $\tan\delta$ as a metric for the amount of energy dissipated by the composites is appropriate for elliptical stress-strain plots but not for the distorted stress-strain loops observed for FSMA-loaded samples. Figure 5-6 shows that the loss is not only due to a phase lag in the strain response of the system, but also due to a distortion of the strain response. Equation 1.6 shows why $\tan\delta$ can be used as a measure of the energy dissipated, but from the same equation it can also be seen that the definition is only valid if the real and the imaginary parts of the modulus are linear. For the FSMA-loaded samples the moduli are not linear making $\tan\delta$ an inappropriate measure of the energy dissipation. The use of the loss ratio is a more appropriate metric for FSMA-loaded samples, because its definition does not depend on the shape of the stress or strain loops. The loss ratio is simply the quotient of the energy dissipated by the system to the total mechanical energy given to the system, which can be obtained from any loop shape.

5.5.2 Temperature dependent measurements

In Figure 5-8 the FSMA-loaded composite shows the behavior that would be expected, as the material goes from martensite to austenite the loss in the composite material decreases. If the large loss in the FSMA-loaded sample is due to the motion of twin boundaries, then as the material becomes austenite the mechanism responsible for the additional loss

disappears and the loss ratio decreases.

The polyurethane matrix on the other hand showed a broad peak in the loss ratio near the glass transition of the polyurethane. The fact that the glass transition temperature of the polyurethane coincides closely with the the martensite/austenite transformation temperature is unfortunate. This increase in the loss of the matrix makes it difficult to observe the changes in the loss ratio due to the contribution of the FSMA particles as they undergo their phase transformation [54].

The glass transition temperature of the matrix material was overlooked when its selection was made, but its clear from these measurements that the glass transition temperature should be taken into account along with mechanical and curing properties when the matrix material is chosen.

Despite the issues that the glass transition of the matrix presented, the measurements of the loss ratio as a function of stress at the two temperature extremes of Figure 5-8 provide valuable information about the loss mechanisms in the composites. At the lower temperature (Figure 5-9) the FSMA/polymer composite shows a loss ratio that is dependent on the stress applied. This stress dependence disappears at the higher temperature (Figure 5-10), where the material is austenitic. This is consistent with the other evidence of twin boundaries causing the added loss to the system. Figure 5-11 shows how close the martensite/ausetenite transformation is to the glass transition temperature, and why there is such a large change in the loss ratio of the polymer matrix in the temperature range shown.

The loss ratio in the composite is lower than in the pure polymer at 47°C. At that temperature most of the loss is due to the polymer, but while the total volume of both samples is the same, the composite sample has only 80% of its volume consisting of polymer, so it can not dissipate as much energy.

5.6 Conclusions

The addition of Ni–Mn–Ga particles to the polyurethane matrix significantly increases the amount of energy that can be dissipated. The loss of the FSMA composites is much larger than the matrix material by itself and larger than in iron loaded control samples used. The

loss ratio in the FSMA loaded composites is stress dependent in a way that would be expected from a system with active twin boundaries. The stress-strain loops maintain the same elliptical shape for both control samples but for the FSMA-loaded samples they show a decrease in effective stiffness at higher stress amplitudes. This is a strong indication that active twin boundaries in the FSMA particles in the composites are responsible for the added loss.

The temperature-dependent data shows that the mechanism responsible for the added loss in the composites disappears above the martensite to austenite transformation temperature of the Ni–Mn–Ga particles added to the composite. This is additional evidence that the added loss is due to twin boundary motion.

When a matrix material is chosen, the glass transition temperature of the polymer should be taken into account. The glass transition temperature should be above the austenite finish temperature, ensuring that the polymer will have a relatively constant stiffness change over a moderate temperature range.

Chapter 6

Modeling

This chapter presents the results of two different types of modeling. First a finite-element model is used to study the stress distribution in the FSMA/polymer composites. Second a numerical model simulates the cyclic loading of the FSMA/polymer composites and is an early attempt at describing the non-elliptical loops presented in the previous chapter.

6.1 Description

6.1.1 Finite-element modeling

Finite-element analysis was used to determine the stress distribution in the FSMA–polymer composites. The finite-element analysis was done using OOF, a free program written at NIST. The following passage is the description from the program's web site[1]:

> *" OOF is designed to help materials scientists calculate macroscopic properties from images of real or simulated microstructures. It is composed of two cooperating parts: ppm2oof and oof. ppm2oof reads images in the ppm (Portable Pixel Map) format and assigns material properties to features in the image. oof conducts virtual experiments on the data structures created by ppm2oof to determine the macroscopic properties of the microstructure. Currently, the programs calculate stresses and strains, . . . "*

[1] http://www.ctcms.nist.gov/oof/

6.1.2 Cyclic stress-strain modeling

The modeling of the strain response of the composites to a cyclic stress was carried out in Wolfram's Mathematica®. The response was characterized using a *constant stress* and a *constant strain* approach. In each of the cases the stress (or the strain) was incremented in small steps and the strain (or stress) was calculated separately for the FSMA filler and for the polymer matrix. The stress or strain for each of the two parts were then added together, weighed by their volume fractions.

Constant-stress refers to the case where the FSMA and the polymer are assumed to be layered, and the stress is applied normal to the layers. The stress is constat through the layer and the strain is unique for each layer.

Constant-strain refers to the case where the FSMA and the polymer are assumed to be layered, and the stress is applied parallel to the layers. The strain is forced to be the same on all layers and the stress is the result of each layer being forced to stain a given amount.

6.2 Method

6.2.1 Finite-element modeling

For the finite-element modeling, simplified images of the composite cross-section were drawn because actual SEM micrographs were too complex and the program could not generate the mesh correctly. The images used to simulate the composites were drawn so that the two-dimensional picture would consist of projections of the three dimensional case, and the spacing of the particles would be that found in a composite with the desired FSMA volume fraction.

The FSMA particles where taken to be spheres, and to build the image of the composite the dimensions of a rectangular prism were calculated so that the ratio of the volume of the prism to the sphere would correspond to the volume fraction in the composite. In the projection the FSMA particles would look like circles in the center of a rectangle of dimensions $l_1 \times l_2$. The full image was created by stacking the rectangles with the circles in the center. The dimensions of the rectangular prisms were calculated for two different

assumptions; 1) the particles were evenly spaced in a square grid surrounded by polymer and 2) the particles formed unidimensional chains, where the particles touch only in one direction and are evenly spaced in the others.

For the evenly spaced case, if the particles of radius is r the volume V of the rectangular prism (a cube in this case) for a composite with a volume fraction of filler χ is given by:

$$V = \frac{4\pi r^3}{3\chi} \tag{6.1}$$

From the volume, the length of the cube side l can by calculated by:

$$l = \sqrt[3]{\frac{4\pi}{3\chi}}\, r \tag{6.2}$$

For the case where the particles are in chains, the volume of the prism is the same, but now there two of the lengths of the sides are the same and a the third one is different. The length of the prism's side along the chain direction is simply given by the diameter of the particles and is given by ($l_1 = 2r$). The dimensions of the two other sides ($l_2 = l_3$) are given by:

$$l_2 = l_3 = \sqrt{\frac{2\pi}{3\chi}}\, r \tag{6.3}$$

After the images were generated they where imported into OOF and mechanical properties were assigned to the polymer matrix and the FSMA particles. Once this was done the mesh was automatically generated.

Figure 6-1 shows the image used to simulate the case where the particles are evenly distributed in the polymer and account for 25 % of the volume in three dimensions. Figure 6-2 shows the image for the case where the particles take up 25 % of the volume and are aligned in chains with very small gaps between the particles.

For the last step, the desired distortion was applied to the newly generated mesh and the system was equilibrated.

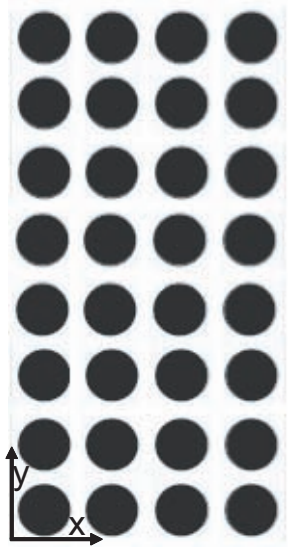

Figure 6-1: Two-dimensional projection for a composite with 25 vol % filler evenly distributed in the matrix.

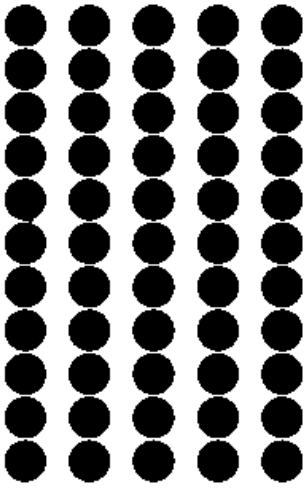

Figure 6-2: Two-dimensional projection for a composite with 25 vol % filler aligned in chains in the matrix.

6.2.2 Cyclic stress-strain modeling

To model the response of the composites to a cyclic strain, a numerical model was developed. The model generates the stress-strain loop for the polymeric matrix using a sinusoidal load and assuming the strain response also to be a sinusoidal, lagging by an angle δ. A stress-strain loop for the polymeric matrix is calculated for a full cycle and is then divided into small increments of stress and the corresponding strain increment. For the constant-stress approximation (FSMA and Polymer are in series), the stress increments are

used to calculate the strain increments in the FSMA, and then the total strain is the sum of the strains weighted by their volume fractions. Conversely for the constant strain approximation (FSMA and the polymer elements are in parallel), the strain increments from the polymer cycle are used to calculate the stress on the FSMA and the total stress is the sum of the stresses weighted by the volume fraction. The stress (or strain) on the FSMA is calculated by a segmental model that assigns a stiffness to the FSMA based on the stress amplitude, strain history and direction of the increment relative to the previous one. Thus the calculation permits the hysteretic behavior of the FSMA to be modeled if the increments are small enough.

6.3 Results

6.3.1 Finite-element modeling

The finite-element modeling was intended give an idea of the stress on the particles in the composite before the threshold stress for twin motion was reached. Figure 6-3 shows the xy shear stress distribution in a 25 vol % composite where the filler particles are placed on an evenly spaced square grid. The center-to-center spacing in the vertical and horizontal directions, relative to the particle radius is given by Equation 6.2. The matrix stiffness was set to 0.2 and the filler stiffness was set to 120. The Poisson ratios for the simulations were 0.33 and 0.46 respectively, These material parameters were used for all the simulations shown in the figures shown in this section, and they correspond to the properties of the the polyurethane and FSMA without twin boundary motion in the composites.

In Figure 6-3 a), the composite is subjected to a 3 % uniaxial compressive strain. The uniform color in the figure indicates there is no great difference in the stress between the particles and the matrix . At the edges of the particles, bright and dark spots can be seen, indicating higher values of stress at the edges of the particles.

Figure 6-3 b), shows the same composite as in Figure 6-3 subjected to a 3 % uniaxial tensile strain. The xy shear stress distribution in the composite is almost identical to the compressive case, and as in the case of the compressive stress, only small stress concentra-

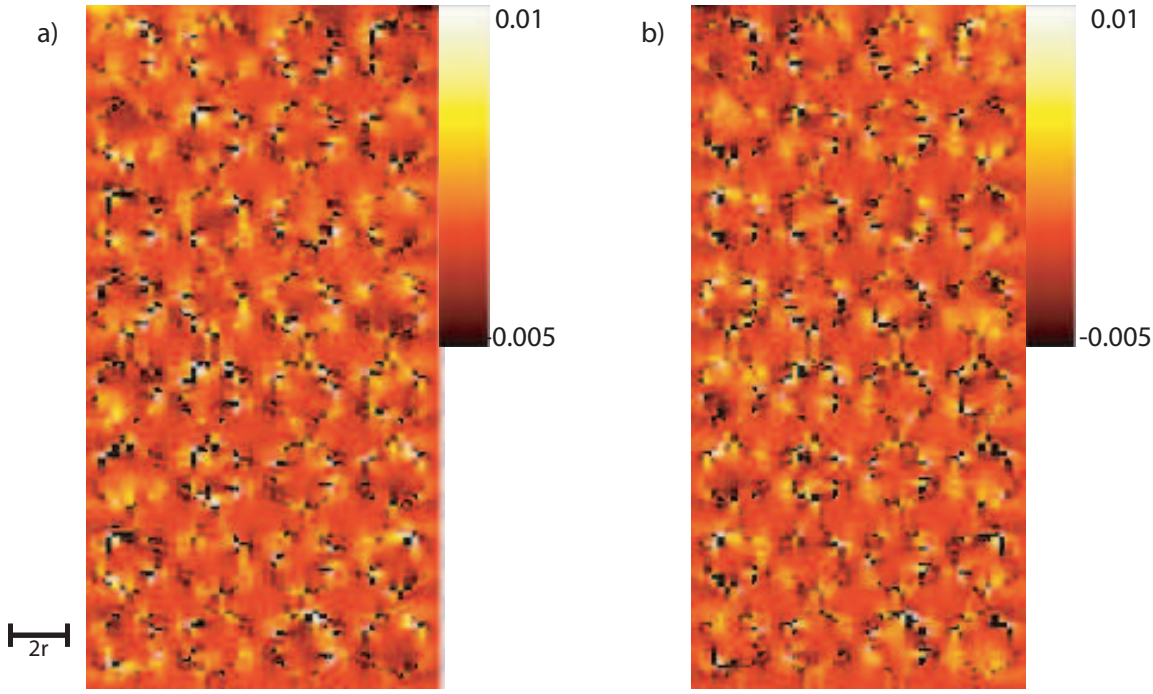

Figure 6-3: Simulation of the xy shear stress in a composite with 25 vol. % filler evenly distributed subjected to a) 3 % uniaxial compressive strain (strain along the vertical (y) direction), b) 3 % uniaxial tensile strain (strain along the vertical (y) direction). Note the similarity in stress states for both cases.

tion points at the edges of the particles, can be observed.

Figure 6-4 a), shows the shear stress distribution in a 25 vol. % composite in which the particles are arranged in chains along the strain direction. When subjected to a 3 % uniaxial compressive strain in the vertical direction, the composite shows a high shear stress concentration in the particles, much larger than in the evenly spaced particle case (Figure 6-3) a). The matrix shows almost no stress, while the stress in the particles corresponds to the extreme values on the scale. The stress distribution on the particles is divided in quarters, the diametrically opposed quarters having the same sign stress.

Figure 6-4 b) shows the effect of a vertical uniaxial tensile stress on the particle-chain composite. As in the case with the compressive stress the shear stress is concentrated mostly in the particles. The pattern of the stress on the particles is the same as when the composite was exposed to a compressive stress, but the signs of the stresses in the particles are reversed compared with the compressive case (Figure 6-4 a)).

To evaluate the effect of the difference of stiffnesses between the matrix and the FSMA

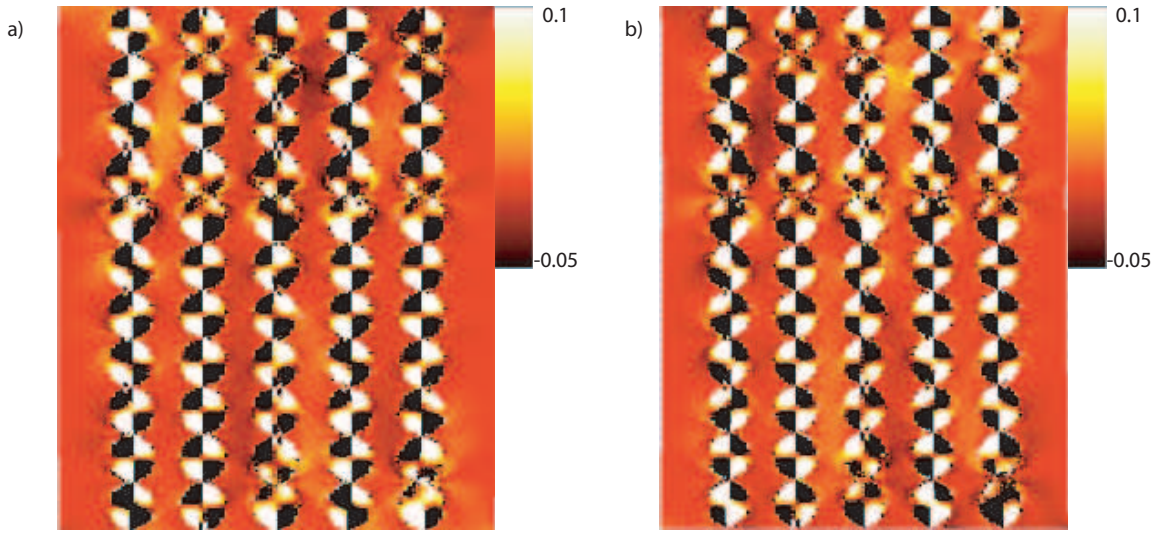

Figure 6-4: Simulation of the xy shear stress in a composite with 25 vol. % filler aligned in chains subjected to a) 3 % uniaxial compressive strain (strain along the vertical (y) direction), b) 3 % uniaxial tensile strain (strain along the vertical (y) direction). note reversal of stress directions between the two cases.

on the stress distribution in the the particles a series of simulations varying the ratios of the stiffnesses was carried out for the particle-chain case. When difference in the stifnesses was very large, and the matrix was much softer than the FSMA, as is the case in the real composites characterized experimentally in Chapter 5, the stress mostly concentrated on the particles. As the stiffnesses became more similar, less of the stress was concentrated at the particles. When the stiffnesses became equal for both components, the stress concentration was seen in the corners of the rectangular sample, along the diagonals, similarly to what was observed in the particles when the stiffness difference was very large.

The finite-element modeling shows that the alignment of the particles in chains concentrates the shear stress on the particles, while having them separated by polymer evenly in all directions does not concentrate the stress as much on the particles.

6.3.2 Cyclic stress-strain modeling

We turn now to the numerical simulation of the stress-strain loops. Figure 6-5 shows the simulated strain as a function of the stress increments for a) the polymer matrix, b) the FSMA and c) the resulting sum at constant-stress. For these loops the maximum stress

was assumed to be the same for each component. Physically this would mean that the polymer and the FSMA are in series. For these loops the phase angle for the polymer was set at 0.2 radians, this is close to the value measured for polyurethane in Figure 5-4. The threshold stress for twin motion in the FSMA was 2 MPa and the stress amplitude used for the simulation was 4 MPa. The volume fraction of FSMA in the polymer was set to 25 %. For all the simulated loops, the FSMA was set to be a single variant that would initially respond only to the positive (tensile) stress applied to the composite. The simulated loop for the polymer matrix (Figure 6-5 (a)) is an ellipse, much like the one seen in the stress-strain loops measured for polyurethane (Figure 5-4). The FSMA loops (Figure 6-5 (b)) look very similar to the loops reported for single crystals of Ni–Mn–Ga subjected a cycle of tension and compression [36]. The slope of the nearly vertical regions corresponds to the un-twinned modulus, and the nearly horizontal regions correspond to the modulus when twins are mobile.

The simulated loop for the composite (6-5 (c)) shows a large hysteresis and a slight rounding at the inflection points. Figure 6-5 (c) also shows small rounded protrusions at the end points, these correspond to the regions where the FSMA stiffness has returned to the high value in Figure 6-5 (b). It can be seen that the loop resulting from the convolution of the FSMA and the polyurethane loops is not centered about the origin, but rather shifted to the right. The simulated loops are symmetric about a point on the strain axis.

Figure 6-6 shows the evolution of the stress-strain loops simulated using the constant strain approximation, as the stress amplitude is increased. When the maximum stress applied is less than the threshold stress for twin-boundary motion, the resulting loop for the composite is a perfect ellipse (Figure 6-6 (a)). For a stress that is larger than the threshold stress for the twin motion, but not high enough to saturate the twin motion (6-6 (b)), the hysteresis becomes much larger than which was observed in Figure 6-6 (a), and discontinuities become apparent in the the loops. When the stress becomes large enough to saturate the motion of the twins (6-6 (c)), the loops start showing a second inflection point at the higher stress levels, leading to the small protrusions observed at the loop extremes.

Figure 6-7 shows the simulated stress-strain loops for the composite material using the constant strain approximation for three different maximum applied strain levels. Figure 6-7

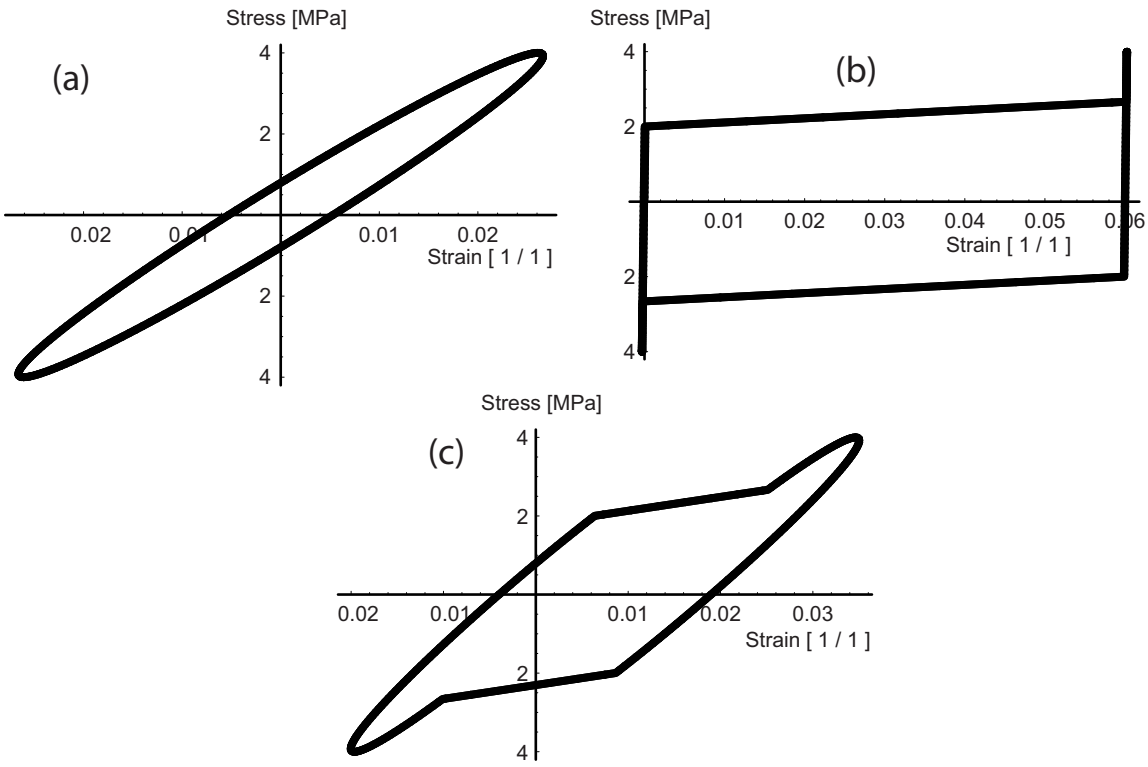

Figure 6-5: Simulated stress-strain loops for the constant-stress approximation for (a) the polymer matrix (b) the FSMA and (c) the convolution of (a) and (b) at 25 vol. % FSMA.

(a) shows a maximum strain level that is right at the onset of twin motion, The maximum strain is only 0.055%. The stress amplitudes are different in the positive and the negative half of the loop, in the negative half of the plot the stress is about four times that of the positive half of the loop. As the magnitude of the applied strain is increased, the plots become more and more asymmetric about the x-axis. In Figure 6-7 (b) the strain is not large enough to saturate the twin motion, and the difference in the stress magnitudes, between the positive and the negative sides is now about 50 times. Figure 6-7 (c) shows a strain of 6.1%, slightly larger than the saturation strain of the twins (6%). The difference in the strain amplitudes is now much smaller than before, because as soon as the twins saturate, the stress increases very rapidly on the positive half, but remains asymmetric.

The roundness of the loops is affected by the value of δ set in the polymer model. A higher value of the phase angle makes the loops look more rounded.

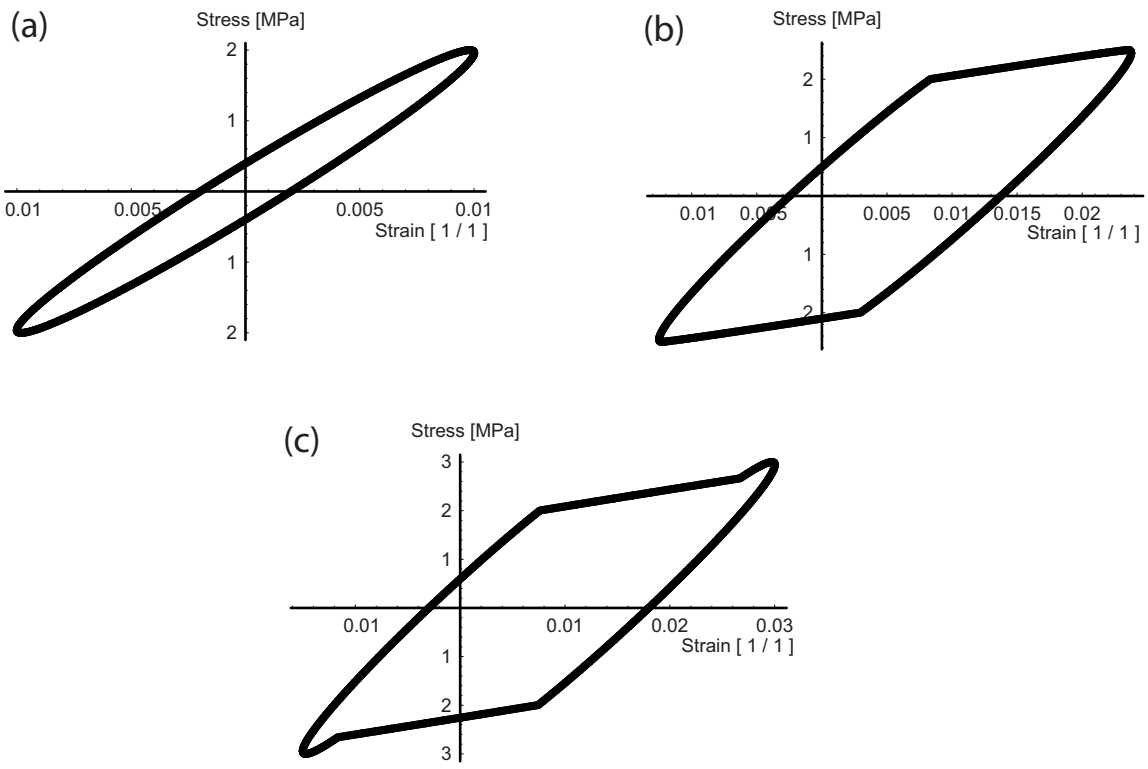

Figure 6-6: Simulated stress-strain loops for the composite under the constant-stress approximation for three maximum stress amplitudes: (a) 2 MPa (b) 2.5 MPa and (c) 3 MPa.

6.4 Discussion

6.4.1 Finite-element modeling

The finite-element simulation of the composites shows that the particles in the composites experience a much larger stress for the same applied deformation when they are aligned in chains than when they are evenly spaced in the matrix. The high concentration of shear stress on the particles means that the motion of twin boundaries will be favored, because twin boundaries move in response to a shear stress.

The stress distribution for the tensile and compressive simulations are similar, which suggests twin boundaries can be moved when the composite is under tensile and compressive loads.

When the particles are aligned in chains, there does not appear to be a high stress concentration at the FSMA/particle interface. This indicates that the particles are not likely to delaminate, since this is caused by the shear stress at the interface.

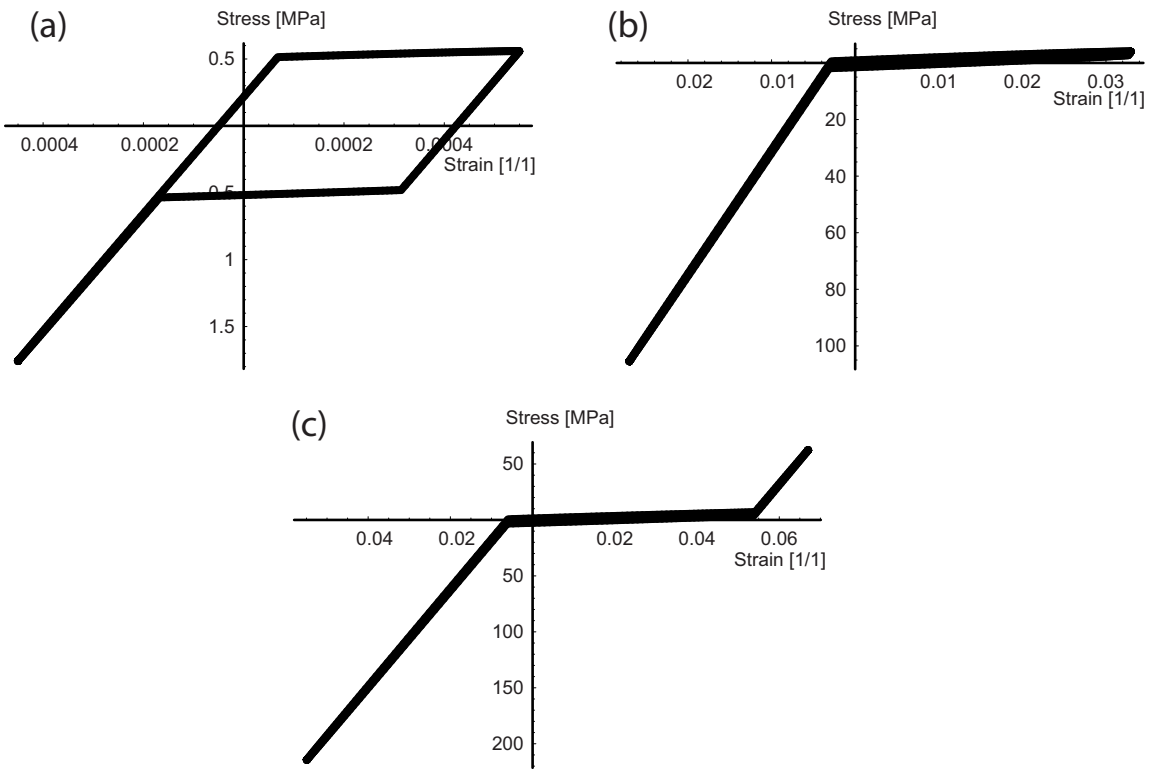

Figure 6-7: Simulated stress-strain loops for the composite under the constant strain approximation for three maximum strain amplitudes: (a) 0.0005 (b) 0.03 and (c) 0.061.

6.4.2 Cyclic stress-strain modeling

When the constant-stress approximation was used, the stress-strain plots derived from the numerical simulation were in agreement with the measured loops (Figure 5-5). The wide hysteresis, the inflection points and the flat (low stiffness) regions were reproduced by the model.

The constant-strain approximation does not resemble the measured loops as much, but that is probably due to the values of stress calculated for the composite. By forcing the FSMA to strain as much as the polymer would, the stress levels calculated are not physical. For example Figure 6-7 (c) shows the system deforming elastically 6.1% in the negative quadrant. Such a large elastic deformation can be expected from a polymer, but not from a metal, however when the maximum strain is kept low (Figure 6-7 (a)) the loops do resemble the experimental results to an extent.

It is important to notice that the model explains why the stress-strain loops for the com-

posite (Figure 5-5) are not symmetric about the origin. The left to right shift is accounted due to the initial variant distribution in the particles, and that shift shows up both in the constant-stress and the constant-strain approximations. The up and down shift in the loops is explained by the constant-strain model that shows that when the twins are not mobile the stress in the composite increases at a different rate than when they are mobile.

In reality, the composite cannot be accurately modeled by either the constant-stress or the constant-strain approximations individually. This is because they are not 2:2 (laminated) composites, but pseudo 3:1 composites that have regions where the polymer and the FSMA particles are in parallel and others where they are in series. The real response is more likely a combination of constant-stress and constant-strain elements.

The models do not take into account that in the real composite there is a large number of particles with slightly different threshold stresses. It is not hard to imagine that this distribution in threshold stresses in the particles due to composition variations and slight misalignment of the c-axis of the particles with respect to the load direction could cause the sharp inflections seen in the modeled loops to become softer and more rounded, resembling more the measured loops.

6.5 Conclusions

From the finite-element modeling it can be seen that the particle chain arrangement in the field-cured composites concentrates the stress on the particles. The stress is concentrated on the particles both under compression and in tension, favoring the motion of the twin boundaries in the composite since twins respond to a resolved shear stress.

When the stiffnesses of the matrix and the filler are the same, the stress distribution is uniform throughout the composite. Having a matrix that is less stiff than the un-twinned filler implies a concentration of the stress on the particles.

The features observed in the stress-strain loops presented in Chapter 5 can be explained by the incremental model presented in this chapter, including the inflections, the large hysteresis, and the loops offset. The simplified model can not exactly recreate the stress-strain loops, but it shows that the additional loss in the FSMA composites is very likely due

to twin-boundary motion and not other mechanisms.

Chapter 7

Engineering Issues

7.1 Heating

It was shown in Chapter 5 that the additional loss due to the motion of twin boundaries disappears when the Ni–Mn–Ga particles are heated into the austenite phase, because of this and the relatively low difference between room temperature and the austenite transformation temperature. Its important estimate the temperature increase in the sample due to the energy dissipated in the composite.

The heating of the particles in the composite can be estimated by calculating the amount of energy dissipated every cycle, by treating the composite as a viscoelastic material. The phase lag δ between stress and strain can be related to the loss ratio η by:

$$\eta = \frac{\Delta W}{W} = 2\pi \tan \delta \tag{7.1}$$

The amount of energy dissipated every cycles ΔW is given by:

$$\Delta W = \pi \sigma_0 \epsilon_0 \sin \delta \tag{7.2}$$

Combining Equations 7.1 and 7.2 the loss per cycle can be calculated as a function of the loss ratio, the peak strain ϵ_0 and the peak stress σ_0. This corresponds to the specific

damping capacity of the polymer D

$$\Delta W = \pi \sigma_0 \epsilon_0 \sin(\arctan \frac{\eta}{2\pi}) \tag{7.3}$$

The power per unit volume P dissipated at a given frequency f is given by:

$$P = \pi \sigma_0 \epsilon_0 \sin(\arctan \frac{\eta}{2\pi}) f \tag{7.4}$$

The rise in temperature of the sample is given by:

$$\frac{Q_{gen}}{V} = C_p \rho \Delta T \tag{7.5}$$

Where $\frac{Q}{V}$ is the heat per unit volume, m is the mass of the sample, C_p is the heat capacity of the particles and ΔT is the change in temperature of the particles. Equation 7.5 can be re-written as a function of time Δt to obtain:

$$\frac{Q_{gen}}{V \Delta t} = C_p \rho \frac{\Delta T}{\Delta t} \tag{7.6}$$

Combining Equations 7.4 and 7.6 we get:

$$\pi \sigma_0 \epsilon_0 \sin(\arctan \frac{\eta}{2\pi}) f = C_p \rho \frac{\Delta T}{\Delta t} \tag{7.7}$$

The change in temperature as a function of time for a given frequency will then be given by:

$$\Delta T = \pi \sigma_0 \epsilon_0 \sin(\arctan \frac{\eta}{2\pi}) \frac{1}{C_p \rho} f \Delta t \tag{7.8}$$

Using the values for the loss ratio and the peak stress and strain from Figure 5-5 ($\eta = 0.77$, $\epsilon_0 = 0.01$ and $\sigma_0 = 7$ MPa), the heat capacity of Ni–Mn–Ga is approximated by the the heat capacity of Ni ($C_p \rho = 3.960 \frac{\mathrm{MJ}}{\mathrm{K\ m^3}}$)[55], Equation 7.8 becomes:

$$\Delta T = 6.755 \cdot 10^{-3} f \Delta t \tag{7.9}$$

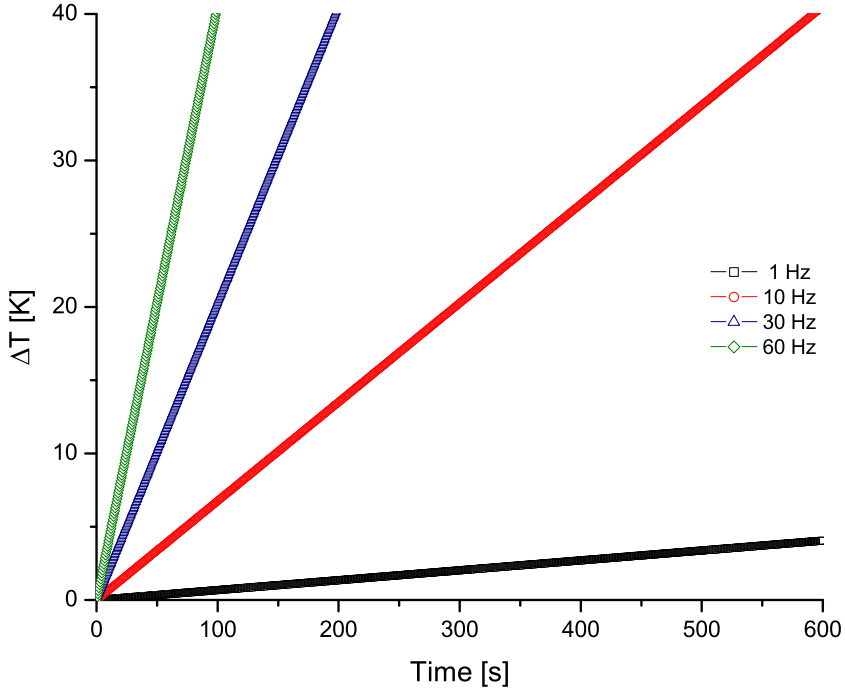

Figure 7-1: Calculated temperature increase (ΔT) for 1 Hz, 10 Hz, 30 Hz and 60 Hz.

Figure 7-1 shows the temperature increase for four different frequencies. This temperature increase is an upper bound for the temperature increase, because it assumes the system (a single powder particle) is perfectly isolated. The lower bound for the temperature increase can be obtained if the heat transfer to the medium is taken into account considering only a thin layer of insulating material in a concentric shell around a single particle of Ni–Mn–Ga.

The heat dissipated into the environment is given by:

$$\frac{Q_{dis}}{t} = \frac{\kappa A \Delta T}{d} \tag{7.10}$$

Where κ is the heat transfer coefficient, A is the surface area the heat is transferred across and d is the thickness of the insulating layer. The net heat causing the particles to heat up is given by the heat generated (Q_{gen}) minus the heat dissipated (Q_{dis}). The temperature

increase can be calculated by:

$$\pi\sigma_0\epsilon_0 \sin(\arctan\frac{\eta}{2\pi})Vf - \frac{\kappa A\Delta T}{d} = VC_p\rho\frac{\Delta T}{\Delta t} \tag{7.11}$$

For a 50 μm particle in 25 vol % composite, using the thermal conductivity of solid polyurethane ($\kappa = 0.220\frac{\mathrm{W}}{\mathrm{m\ K}}$) the corresponding surface area would be $A = 7.85\cdot 10^{-9}$ m^2. The thickness of the insulating layer is 17.75 μm. The temperature vs. time is shown in Figure 7-2 in the trace labeled "Thin insulating layer".

The previous two approaches to calculating the heating of the sample provide the upper and lower bounds for the heating of the sample as a function of time and frequency. The actual temperature of the sample as a function of time will fall between these two limits. A reasonable approximation to the actual particle temperature is to assume that the particles transfer heat to the matrix, but since there is a large collection of point heat sources in the polymer matrix, for the bulk of the sample no heat will be transferred to the outside. Figure 7-2 shows the increase in temperature as a function of time for a sample loaded at 60 Hz, the two extreme cases and the last approximation described.

The from Figure 7-2 we can see that sample heating might be an issue with the FSMA/ polymer composites. The time needed for the the sample to heat up on its own above the martensite transformation temperature under constant a constant 60 Hz drive will be in the order of minutes. The heating is a function of the frequency as can be seen in Figure 7-1. Thus these materials will be best suited for low duty cycle applications or low frequency applications.

7.2 Expected frequency dependence

Due to the low resonant frequency of the apparatus used to measure the mechanical response of the composites it was not possible to characterize the frequency dependence of the Ni–Mn–Ga loaded composites.

However, from the measurements presented in Chapter 5 it can be seen that at 1 Hz the loss in the FSMA loaded composites is higher than the loss in the iron filled sample and in

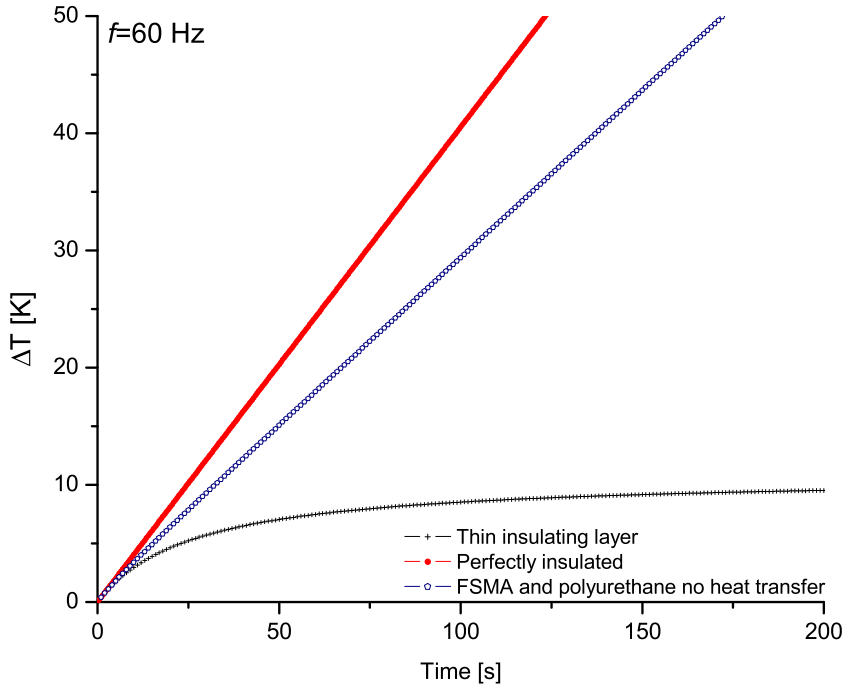

Figure 7-2: Calculated temperature increase (ΔT) at 60 Hz for the particles perfectly insulated, particles with a thin insulation layer transfering heat to the outside with a constant gradient and particles transfering heat to the matrix, but with no heat transfer to the outside

the polyurethane matrix material with no filler. This implies that a fair fraction of the loss in the composite is due to the motion of twin boundaries. Marioni [23] showed from his pulsed field experiments that twin boundaries can be moved at rates equivalent to 1.8 kHz. Loss due to twin motion is similar to loss due to plastic deformation, and that they would fall into the category of *Static hysteresis* described in Section 1.4.1.

The loss due to the matrix should increase as the frequency is increased and the polymer nears its resonant frequencies. For most polymers this peak is found at a few hundred Hertz [2], but it must be determined experimentally for the specific matrix polymer used.

As was shown in Chapter 6 the loss in the composite can be calculated by adding the loss due to the FSMA and the loss due to the polymer. Also, account must be taken of the enhanced loss in the polymer due to stress concentrations at the polymer/particle interface. This can be significant considering Equation 1.10. The loss due to the FSMA will be a constant value that is independent of the frequency and the loss due to the matrix

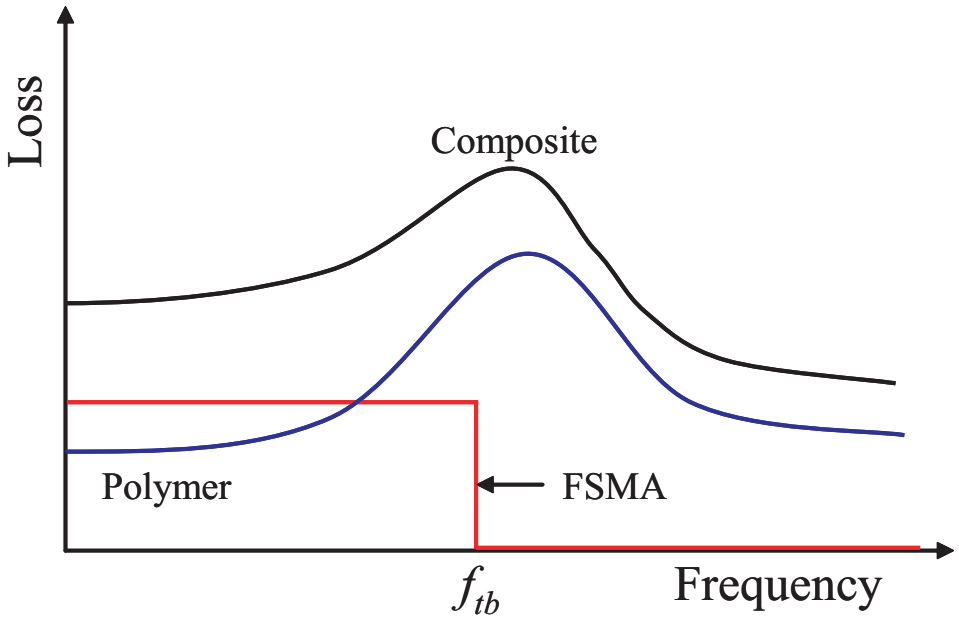

Figure 7-3: Schematic of the expected loss as a function of frequency for the FSMA, polymer matrix and the composite.

will have a strong frequency dependence, especially near the resonant peak. From this it should be expected that the loss versus frequency for the composite will look like the loss for the matrix material offset by a constant value for the frequencies below the maximum frequency for twin motion f_{tb} and will then drop, to a value higher than the pure matrix with no filler above f_{tb}. The values for the loss at frequencies higher than f_{tb} are higher than the matrix with no filler because the FSMA will act like a solid inclusion that will cause stress concentrations around the particles. For a circular hole in an infinite material under a uniaxial load, the maximum stress concentration around the hole is three times the applied load [56]. The stress distribution around a circular hole in a sheet of material subjected to an uniaxial tensile load is shown in Figure 7-4. Equation 1.10 shows that the energy dissipated by a viscoelastic material grows as the stress raised to the 2.4 power. Because of this the presence of stress concentrators increases the loss in the polymer. A schematic of the expected loss is shown in Figure 7-3.

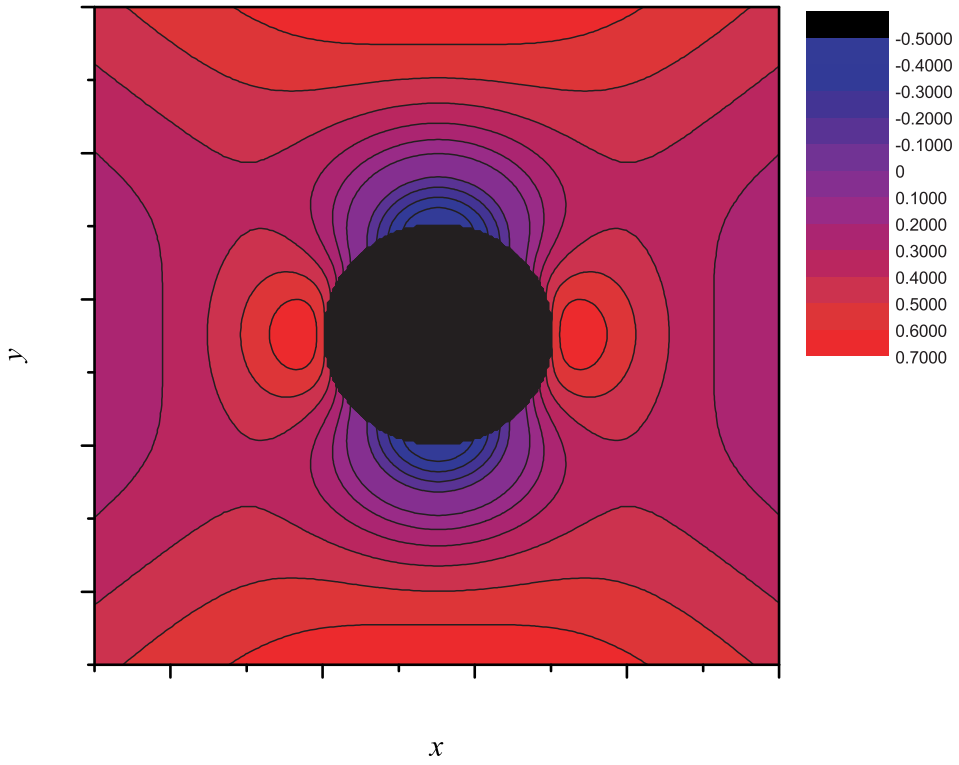

Figure 7-4: Stress distribution around a circular hole of radius one, subjected to an uniaxial tensile load.

7.3 Damping material selection

When selecting a damping material for a practical application a series of factors have to be taken into account. The damping energy of the material D has to match the vibrational energy to be absorbed. The stress on the damping material should be kept below the elastic limit of the material. The volume of damping material required is fixed by the amount of energy that has to be dissipated. The choice of the material also depends strongly on the geometry of the structure where the damping is required, this will set limits on the volume of damping material that can be used, and the relative displacement of the vibrating parts. As is the case with any engineering application, the cost will play an important role in the selection of the damping material to be used. Ni–Mn–Ga loaded composites are, by volume, more expensive than damping polymers, but they can absorb more energy for the same volume as the pure polymer. FSMA/ polymer composites will tend to be a more attractive material for damping in situations where there are constrains on the volume of damping material that can be used and where the cost of replacing the parts damaged by

the vibration would overshadow the cost of using the more expensive composite damping material.

Chapter 8

Summary, conclusions and future work

8.1 Summary

While a great deal of research has been carried out on single crystals of Ni–Mn–Ga because of their possible applications as actuators, little work has been done to explore their usefulness as active fillers in composites. From the stress-strain loops of Ni–Mn–Ga single crystals it was clear that large amounts of mechanical energy could be dissipated in them. However it was not clear that this could be done using small particles dispersed in a polymeric matrix.

For the particles to dissipate large amounts of energy in a composite a series of requirements had to be met. The particles would need to have twin boundaries, and they would have to be oriented so that they could be moved by an external stress. A large number of the twins in the composite would have to be properly aligned with respect to the applied stress to be mobile, and the matrix would have to transfer enough of the load to the particles, so that the stress on them would be larger than the threshold stress for twin boundary motion. Additionally twins would have to be mobile under both tensile and compressive loads, for them to be useful as vibration dampers.

Chapters 2 and 3 presented indirect evidence of the mobility of twin boundaries in the particles under stress. Magnetic properties are linked to the crystal structure of the alloy, therefore changes in the magnetic properties indirectly measure changes in the crystal structure. The mobility of the twin boundaries was inferred from the changes in the direction

of the easy axis of magnetization that is strongly coupled to the unique crystallographic axis of the tetragonal martensite. Any change in the direction of the magnetic easy axis implies a change in the direction of the unique axis in the martensite. When a stress was applied to the composite, the easy axis of magnetization rotated to match the direction of the applied compressive stress. The change in the direction of the easy axis did not occur until a threshold value was reached, after that the increase in the torque or the susceptibility, both measures of size of the magnetic moment along the direction of the applied stress, increased gradually.

The changes in torque and susceptibility observed in Chapters 2 and 3 were plastic, meaning that if the stress on the composite was removed, the change in the magnetic properties remained. The observed change in the direction of the easy axis could be reverted to its original direction by applying a stress normal to the one used to change the direction of the easy axis initially. The response of the composites was consistent with the response of single crystals of Ni–Mn-Ga to a stress. The magnetic measurements also showed that the particles used to make the composites where mostly comprised of a single variant when the composite was cured, and would transform into equivariant particles when heated into austenite and then cooled back into martensite.

Chapter 4 confirmed that the particles used in the composite were martensitic and when the composites were cured under a magnetic field, a high degree of crystallographic texturing could be observed in XRD. It was also observed in XRD that the stress applied to the composite could change the volume fraction of variants having their c-axes parallel to the direction of the applied compressive stress.

SEM images showed that the stress applied to the composites did not cause a noticeable plastic deformation of the particles in the composite, helping to rule this out as a cause of the increased anisotropy observed. If the change in magnetic anisotropy observed in the VSM measurements were due to shape anisotropy would require one of the axes of the sphere to be reduced to half the length of the others by the applied stress. No such large deformation is observed in the images taken after the composite is stressed.

The HRTEM images showed two kinds of twin boundaries in the the spark eroded particles. The first kind are due to the layering of the martensite, and are not expected to be

mechanically active. The second kind observed have the possibility of being active under stress, and are most likely responsible for the change in the direction of the c-axis observed in the VSM, torque and XRD measurements.

Chapter 5 describes the response of the FSMA composites to a cyclic load. The composites loaded with Ni–Mn–Ga particles show a higher loss than the pure polyurethane matrix material or the iron-loaded samples with the same volume fraction of filler material. The composites show loss ratios that are a function of the stress they are subjected to. As the stress amplitude on the FSMA composites increases, the loss increases. Stress-strain measurements as a function of temperature show that once the composites are heated above the austenite transformation temperature of the Ni–Mn–Ga particles, the loss ratio of the composites no longer depends on the stress amplitude. The increasing loss as a function of stress amplitude that disappears when the FSMA composites are heated into austenite phase, suggest that the extra loss observed in the composite is due to the motion of twin boundaries.

Chapter 6 shows that the particle-chain texture of the samples concentrates the stress on the particles making it very likely that the stress on the particles will reach the threshold for twin boundary motion.

The modeling of the response of the composites to a cyclic stress by convoluting the response of the polymeric matrix with the response of the FSMA can recreate the principal features of the measured stress-strain loops. This provides further evidence that a large fraction of the loss in the composites is due to the motion of twin boundaries.

Chapter 7 discussed the expected heating of the composites as a result of dissipating mechanical energy. The calculations presented in that chapter suggests that the particles in the composite will transform into austenite within a few seconds if the material is driven at 60 Hz, due to self heating. The expected frequency dependence of the loss in the composites is explored.

8.2 Conclusions

At the beginning of this work it was not known that FSMA composites could be used as vibration dampers. It was not clear that the FSMA particles in the composite would have twin boundaries that could be moved by a load applied to the composite. It was also not clear how the loss in the particles would add to the overall loss of the composite.

The VSM and torque magnetometry measurements showed indirectly that when the composites were exposed to an external stress the measured response was consistent with twin boundary motion. The change in the direction of the easy axis showed a threshold strain needed to be reached before the rotation of the easy axis would be observed. After the threshold was reached the increase in torque or susceptibility was gradual. This change is reversible only if an orthogonal reset stress is applied and the direction of the easy axis of magnetization is parallel to the direction of the applied compressive stress. All these features are consistent with the behavior of single crystals of Ni–Mn–Ga suggesting very strongly that the composites had mobile twin boundaries. Later the mobility of the twin boundaries was confirmed by x-ray diffraction. The measurements for samples subjected to uniaxial compressive stresses indicate that twin-boundary motion could be reversed.

High-resolution transmission electron micrographs showed the particles used had twin boundaries. The x-ray measurements showed that the particles in the composites cured in a magnetic field had a high degree of texture, and the magnetic measurements showed that the particles used were mostly single variant when the composite was made. The particles in the composite were properly oriented and aligned in the composite to respond to a load parallel to the chain axis.

The energy dissipated by the FSMA composites was larger than the loss in the matrix by itself or in a control sample with the same volume fraction of an inert magnetic filler. In the FSMA loaded composites the loss ratio was a function of the stress amplitude when the measurements were done at temperatures where the FSMA particles were martensitic. The stress dependance disappeared if the measurements were done at temperatures where the FSMA particles were austenitic. This temperature dependant change in the stress response of the composite indicates that twin boundaries are responsible for the additional loss in

the composites, since twins can only exist in the martensite.

Modeling then showed that the departure from ellipticity only observed in the Ni–Mn–Ga composites could be explained reasonably well by a simple addition of the stress-strain loops for the polymer matrix and the FSMA. This served as additional evidence that the extra loss was due to the twin variant redistribution in the particles.

The matrix had to cure below the austenite start temperature of the particles used, to ensure they would retain their preferred variant orientation in the composite. The volume change in the matrix has to be taken into account, as the response of the particles could be affected by the stress state on the particles due to the matrix expanding or contracting as it cures. A zero-volume-change matrix was favored to preserve the particles single variant state and allow twin boundary motion. The stiffness of the matrix relative to the two stiffnesses of the FSMA has to be taken into consideration. A matrix with a stiffness matched to the twin boundary stiffness of the FSMA (i.e when the twins are mobile) appears to be the best choice. The particles will support most of the external stress until the threshold stress is reached. Once the threshold was surpassed, the stress on the particles and the matrix would be roughly equal, because the stiffness of the particles would be similar to the stiffness of the matrix. In the stress region where the twins are mobile both the matrix and the FSMA would strain by the same amount for the same stress.

The glass transition temperature of the polymer used as the matrix also has to be taken into account. The glass transition temperature should be greater than the austenite finish temperature, so the matrix will not have drastic changes in stiffness or loss ratio near the transformation temperature of the FSMA particles.

The Composites appear to be best suited for use in low frequency applications, not due to the frequency dependence of the loss in the composites since it will vary less than the loss of the polymer matrix with no filler, but because of the self heating in the sample. They are well suited for use in higher frequency applications if the duty cycle is low.

8.3 Future work

The temperature dependent measurements presented in Chapter 5 showed that the choice of matrix made in these experiments complicated the separation of the loss as a function of temperature due to the FSMA and the matrix. A new matrix with similar mechanical properties to the one used should be found, but its glass transition temperature should be well above the austenite finish temperature. The new matrix will allow the response of the composites to be characterized around the martensite/austenite transformation temperatures, without the matrix severely interfering with the measurement. It has been reported that FSMAs show an increase in their internal friction near the transformation temperature [57]. For engineering applications, the glass transition temperature could be chosen so that the increase in loss due to the glass transition could extend the useful temperature range of the composites.

A matrix material that has a non-zero volume change while curing can be used to introduce a pre-load on the FSMA particles. This would make the composite more active under tension or compression depending on wether the change in volume while curing is positive or negative. The stress state on the particles could be calculated using the Eshelby method if the stiffnesses and the volume change are known [58].

The effect of the particle size on the loss ratio of the composite should be studied. Preliminary results suggest that the loss as a function of stress amplitude for the composites varies depending on the size of the particles used. These early results could not be corroborated and therefore were not presented, but indicate that further work in this area should be undertaken. As was described in the introduction, Hosoda has shown that the particle size has an effect on the thermoelastic response of the composites [31].

The frequency response of the composites could not be characterized beyond about 10 Hz because the resonant frequency of the tester built was around 10 Hz. In the case of the polymer matrix, the $\tan\delta$ has a strong dependence on the frequency of the load. There is nothing in the data that indicates that the response of the FSMA should have a strong frequency dependence. Henry [1] showed cyclic actuation of FSMAs up to 500 Hz and Marioni showed one-time pulsed actuation that would correspond to kilohertz range

actuation [23]. In Chapter 7 the frequency dependence of the composites was inferred based on the loss of the polymer, the FSMA and the loss due to the stress concentration in the particles, but further experiments should be conducted to confirm the proposed frequency dependence of the loss.

The possibility of controlling the stiffness of the FSMA particles with a magnetic field has been suggested. Preliminary results of measurements in which the composites where exposed to the field from two permanent magnets showed no effect on the loss. The field from the magnets was normal to the direction of the field applied during curing. The magnetic field applied to the composites during the mechanical measurements was in a plane of the composite that has no texture to it. The field applied during the measurements would not be as effective in controlling the stiffness, because only a fraction of the particles would be properly oriented to respond to the field. The geometry of the experiment does not allow the field to be applied axially where it would be properly aligned with most of the particles. A second alternating field could be applied to the composites while curing to try to remove the degree of freedom in orientation that the particle have, when composite is cured under a single magnetic field. Averaged over time the alternating field is zero, and would not affect the main variant orientation by the static field. The alternating field and the static field would define a plane and force the c-axes of the low volume fraction variants to lie in it. This multi-field technique has been shown to work in generating interesting magnetic particle structures inside a polymer matrix [59]; if this can be done the composites would be more likely to respond to an applied field by changing their stiffness.

The phenomenological model described was able to reproduced most of the features of the measured stress-strain loops, but did not fully match the loops. A more complete model that includes the threshold stress distribution and combines the constant stress and the constant strain approximations should be developed.

Appendix A

Loss ratio calculation script

This is the full script used to calculate the loss ratio of the stress-strain loops. The script was written in Mathematica 5.1.

The script reads a set of data files given by a file with the list of names. For each file the minimum and maximum values of stress and strain are found, the script removes the non-monotonic points and the loss ratio is calculated by integrating the load and unload paths.

```
dir = "C:\\Users\\feucht\\Brass clamps\\hp75um run2\\"
Off[General::spell1]
nl = Flatten[Import[dir <> "names.csv", "CSV"]]
ressize = Flatten[Dimensions[nl]]
res=Table[0,{i,ressize[[1]]},{j,3}] (For[icount = 1, icount
<((ressize[([1]\)] + 1)) fileandpath=dir <> nl[([icount])];
a=Import[fileandpath, "\<CSV\>"]; tmp = Flatten[a[([3])]];
description = tmp[([2])];
 b=Table[a[([i + 20])], {i, 3990}];
temp = Dimensions[b]; tpoints=temp[([1])];
strain=Table[(-(b[([i,5])]\/12.8))*100, {i, tpoints}];
stress=Table[(-(b[([i,
6])]\/(((.00533*.0053))*1000000))),{i,tpoints}];
f=Flatten[Position[stress, Min[stress]]]; ff=f[([1])];
avgdif=Abs[(stress[([ff - 1])] + stress[([ff + 1])])\/2] -
```

```
Abs[stress[([ff])]]; While[Abs[avgdif] >  .01, stress[([ff])] =
(stress[([ff - 1])] + stress[([ff + 1])])\/2;
f=Evaluate[Flatten[Position[stress, Min[stress]]]]; ff =f[([1])];
avgdif=Abs[(stress[([ff-1])]+stress[([ff+1])])/2]-Abs[stress[([ff])]]];
f =Flatten[Position[stress, Max[stress]]]; ff =f[([1])];
avgdif=Abs[(stress[([ff-1])]+stress[([ff+1])])/2]-Abs[stress[([ff])]];
While[Abs[avgdif] >  .01,
stress[([ff])]=(stress[([ff-1])]+stress[([ff + 1])])/2;
f=Evaluate[Flatten[Position[stress, Max[stress]]]]; ff =f[([1])];
avgdif=Abs[(stress[([ff-1])]+stress[([ff+1])])/2]-Abs[stress[([ff])]]];
e =Flatten[Position[strain, Min[strain]]]; If[e[([1])] > 2999,
posmin = e[([1])] - 1000, posmin = e[([1])]]; pphalfcy = 500;
strainshiftuh=Table[strain[([((posmin-1))+i])]-Min[strain],{i,pphalfcy}];
strainshiftlh=Table[strain[([((posmin-1+pphalfcy))+i])]-Min[strain],{i,pphalfcy}];
stressshiftuh=Table[stress[([((posmin-1))+i])]-Min[stress],{i,pphalfcy}];
stressshiftlh=Table[stress[([((posmin-1+pphalfcy))+i])]-Min[stress],{i,pphalfcy}];
lielem=Table[((strainshiftlh[([i+1])]-strainshiftlh[([i])]))*
   (stressshiftlh[([i])]+stressshiftlh[([i+1])])/2,{i,((pphalfcy-1))}];
uielem=Table[((strainshiftuh[([i+1])]-strainshiftuh[([i])]))*
   (stressshiftuh[([i])] + stressshiftuh[([i + 1])])\/2,{i,((pphalfcy-1))}];
upint=\[Sum]\+(i = 1)((pphalfcy-1))uielem[([i])];
lowint=\[Sum]\+(i=1)((pphalfcy-1))lielem[([i])];
lossratio=(upint+lowint)/upint*100;
res[([icount])]={description,Max[stress] - Min[stress], lossratio};
lhplot=Table[{strainshiftlh[([i])],stressshiftlh[([i])]},{i,pphalfcy}];
uhplot=Table[{strainshiftuh[([i])],stressshiftuh[([i])]},{i,pphalfcy}];
lplot = ListPlot[lhplot]; uplot = ListPlot[uhplot];
graphexp=Show[{lplot, uplot}, AxesLabel -> {"Strain", "Stress[Pa]"},
TextStyle -> {FontFamily -> "Times", FontSize -> 14}];
Export[dir<>"im"<>ToString[icount]<>".tif", graphexp, "TIFF"];
(icount++)] Export[dir <> "compilation.csv", res, "CSV>"]
MatrixForm[res])
```

Appendix B

Loss ratio calculation script

This is the full script used to calculate the stress strain loops under constant strain in Mathematica 5.1.

```
 This generates the stress and strain
tables for the polymer given  a sinusoidal stress nsteps = 15000;
angleinc = (2/1) (Pi))/nsteps; delta =  .2; strainpp =  .061;
stresspp = (2.87549*10^6)/ .01913*strainpp; stress = Table[0, {i,
nsteps}] ; strain = Table[0, {i, nsteps}] ; For[i = 1,    i <
((nsteps + 1)),
 stress[([i])] =N[stresspp*Sin[angleinc*i]];
strain[([i])] =N[strainpp*Sin[angleinc*i -  delta]]; (i++)] This
generates the stress and strain increments based on the  prev .
stresses and strains deltastress = Table[stress[[i +1]] -
stress[[i]], {i, (nsteps - 1)]; deltastrain =Table[strain[[i + 1]] -
strain[[i]], {i, (nsteps - 1)}]; slope =
Table[deltastress[[i]]/deltastrain[[i]], {i, (nsteps - 1)}]; The
material has to go back to the elastic(untwinned) modulus as soon as
the the stress increments change sign the material only changes
modulus if the sign of the treshold stress is the same as the sign
of the stress increment.
you have to keep track of the twininng strain and it has to be
between 0 and 6% for a tetragonal sample
stressfsma = Table[0, {i, nsteps}] ; strainfsma = Table[0,
{i,nsteps}]; debugdata = Table[0, {i, nsteps}]; elasticmod =17*10^9;
twinmod = 11*10^6; totalstress = 0; totalstrain = 0; twinstrain = 0;
stresstresh = 2*10^6; maxtwining = 0.06;
```

```
stressfsma[([1])]=deltastrain [([1])]*elasticmod; strainfsma[([1])]
= deltastrain[([1])];
 For[i = 2, i < ((nsteps)), If[Sign[deltastrain[[i])] == 1,
If [ totalstress > stresstresh, If[twinstrain <maxtwining, modulus =
twinmod, modulus = elasticmod], modulus = elasticmod], If
[(-1)*totalstress> stresstresh, If[twinstrain >  0, modulus =
twinmod, modulus = elasticmod], modulus = elasticmod]];
 If[Sign[deltastrain[[i])] == (-1)*Sign[deltastrain[[i - 1])],
 modulus = elasticmod];
stressfsma[[i]] = stressfsma[[i -1]] + deltastrain [[i]]*modulus;
strainfsma[[i]] = strainfsma[[i -1]] +  deltastrain[[i]];
temp=totalstress; totalstress = temp + deltastrain [[i]]*modulus;
temp1 = twinstrain;
If[modulus==twinmod,twinstrain=temp1+deltastrain[[i]]];
debugdata[[i]] = {twinstrain, modulus, totalstress}; (i++)];
polymerplot=Table[{strain[[i]], stress[[i]]}, {i, nsteps}];
fsmaplot=Table[{strainfsma[[i]],stressfsma[[i]]},{i,nsteps-1}];
check =Table[{strainfsma[[i]], stressfsma[[i]], debugdata[[ i]]},
{i,nsteps - 1}]; conststrain = Table[{(strainfsma[([i])]
+strain[([i])])/2, .25*stressfsma[([i])] + .75*stress[[i]]},
{i,nsteps - 1}];
ListPlot[polymerplot]
ListPlot[fsmaplot, PlotJoined
->True, PlotRange ->  {{(-0.07), 0.07}, {(-6)*10^6, 6*10^6}}])
ListPlot[conststrain, PlotJoined -> True, {AxesLabel ->
{"Strain","Stress"}, PlotStyle -> AbsoluteThickness[3], AxesStyle
->{AbsoluteThickness[1]}, ImageSize -> {500, 500}}]
```

This is the full script used to calculate the stress-strain loops under constant stress in Mathematica 5.1.

```
This generates the stress and strain tables for the polymer given  a
sinusoidal stress nsteps = 20000; angleinc = (4/1)(Pi))/nsteps;
delta =  .2; stresspp = 2*10^6;
strainpp=.01913/(2.87549*10^6)*stresspp; stress=Table[0,{i,nsteps}];
strain = Table[0, {i, nsteps}] ;
For[i=1,i<nsteps+1,stress[[i]]N[stresspp*Sin[angleinc*i]];
```

```
strain[[i]]=N[strainpp*Sin[angleinc*i - delta]]; (i++)];
 This generates the stress and strain increments based on the prev.
stresses and strains
deltastress=Table[stress[[i+1]]-stress[[i]],{i,(nsteps - 1)}];
deltastrain = Table[strain[[i + 1]]-strain[[i]],{i,(nsteps - 1)}];
slope = Table[deltastress[[i]]/deltastrain[[i]],{i,(nsteps-1)}];
 The material has to go back to the elastic(untwinned) modulus as soon as
the the stress increments change sign the material only changes
modulus if the sign of the treshold stress is the same as the sign
of the stress increment. you have to keep track of the twininng
strain and it has to be between 0 and 6% for a tetragonal sample
stressfsma = Table[0, {i, nsteps}] ;
 strainfsma=Table[0,{i,nsteps}];
debugdata = Table[0, {i, nsteps}] ;
 elasticmod = 17*10^9;
twinmod=11*10^6;)
 totalstress = 0;
  totalstrain = 0;
 twinstrain =0.0;
stresstresh = 2*10^6; maxtwining = 0.06;
stressfsma[[1]]=deltastress[[1)];
strainfsma[[1]]=eltastress[[1]]/elasticmod;
For[i=2,i<nsteps,If[Sign[deltastress[([i] )]] == 1,
If[totalstress>stresstresh, If[twinstrain<maxtwining,
modulus=twinmod, modulus=elasticmod], modulus=elasticmod],
If[(-1)*totalstress >stresstresh,If[twinstrain>0, modulus=twinmod,
modulus=elasticmod], modulus=elasticmod]];
If[Sign[deltastress[[i]]]==(-1)*Sign[deltastress[([i - 1])]],
modulus = elasticmod];
stressfsma[[i]]=stressfsma[[i-1]]+deltastress[[i]];
strainfsma[([i])] = strainfsma[([i - 1])] +
deltastress[([i])]/modulus;
temp=totalstress;
 totalstress = temp+deltastress[[i]];
 temp=twinstrain;
 If[modulus==twinmod,twinstrain=temp+deltastress[[i]]/modulus];(i++)];
```

```
polymerplot = Table[{strain[[i]], stress[[i]]}, {i, nsteps}];
fsmaplot = Table[{strainfsma[[i]], stressfsma[[i]]},{i,nsteps-1}];
conststress=Table[{0.25*strainfsma[[i]]+0.75*strain[[i]],
(stressfsma[([i])] + stress[([i])])/(2*10^6)}, {i, nsteps - 1}];
ListPlot[polymerplot] ListPlot[fsmaplot, PlotJoined -> True]
$TextStyle = {FontFamily -> "Arial", FontSize -> 16} expplot =
ListPlot[conststress, PlotJoined -> True, {AxesLabel -> {"Strain 1
1", "Stress MPa"}, PlotStyle -> AbsoluteThickness[3], AxesStyle ->
{AbsoluteThickness[1]}, ImageSize -> {500, 500}}]
```

Bibliography

[1] C. P. Henry. *Dynamic Actuation Properties of Ni–Mn–Ga Ferromagnetic Shape Memory Alloys*. PhD thesis, M.I.T., Cambridge, MA, May 2002.

[2] C. M. Harris ed. *Harris' Shock and Vibration Handbook*. McGraw-Hill, 5th edition, 2002.

[3] Y.C. Wang, M. Ludwigson, and R.S. Lakes. Deformation of extreme viscoelastic metals and composites. *Materials Science and Engineering A*, 370(1-2):41–49, 2004.

[4] R.C. O'Handley. *Modern Magnetic Materials*. Willey Inerscience, first edition, 2000.

[5] Jan Van Humbeeck. Shape memory alloys: A material and a technology. *Advanced Engineering Materials*, 3(11):837–850, 2001.

[6] K. Ullakko, J. K. Huang, V. V. Kokorin, and R. C. O'Handley. Magnetically controlled shape memory effect in Ni_2MnGa intermetallics. *Scripta Mater.*, 36:1133–1138, 1997.

[7] G. H. Wu, C. H. Yu, L. Q. Meng, F. M. Yang, S. R. Qi, W. S. Zhan, Z. Wang, Y. F. Zheng, and L. C. Zhao. Giant magnetic-field-induced strains in Heusler alloy NiMnGa with modified composition. *Appl. Phys. Lett.*, 75:2990–2992, 1999.

[8] R. Tickle, R. D. James, T. Shield, M. Wuttig, and V. V. Kokorin. Ferromagnetic shape memory in the nimnga system. *IEEE Magn. Trans.*, 35:4303–4310, 1999.

[9] R. D. James, R. Tickle, and M. Wuttig. Large field-induced strains in ferromagnetic shape memory materials. *Mat. Sci. Eng. A*, 273-275:320–325, 1999.

[10] O. Heczko, A. Sozinov, and K. Ullakko. Giant field-induced reversible strain in magnetic shape memory NiMnGa alloy. *IEEE Magn. Trans.*, 36:3266–3268, 2000.

[11] O. Heczko, A. Sozinov, and K. Ullakko. Giant field-induced reversible linear strain in magnetic shape memory nimnga at roomt temperature. In *INTERMAG 2000 Digest of Technical Papers. IEEE Trans. Mag.*, pages 617–617, Toronto, 2000.

[12] S. J. Murray, M. A. Marioni, A. M. Kukla, J. Robinson, R. C. O'Handley, and S. M. Allen. Large field-induced strain in single crystalline Ni–Mn–Ga ferromagnetic shape memory alloy. *J. Appl. Phys.*, 87:5774–5776, 2000.

[13] A. Sozinov, A. A. Likhachev, N. Lanska, K. Ullakko, and V. K. Lindroos. Crystal structure, magnetic anisotropy and mechanical properties of seven-layered martensite in Ni–Mn–Ga. In *Smart Structures and Materials*, volume Proceedings of SPIE Vol. 4699, pages 195 – 205, 2002.

[14] S. J. Murray. *Magneto-mechanical properties and applications of Ni–Mn–Ga ferromagnetic shape memory alloy*. PhD thesis, M.I.T., Cambridge, MA, January 2000.

[15] Michael J. Hoffmann and H. Kungl. High strain lead-based perovskite ferroelectrics. *Current Opinion in Solid State and Materials Science*, 8(1):51–57, January 2004.

[16] E.F. Prechtl and S.R. Hall. Design of a high efficiency, large stroke, electromechanical actuator. *Smart Materials and Structures*, 8(1):13–30, February 1999.

[17] P. J. Webster. Heusler alloys. *Contemp. Phys.*, 10:559–577, 1969.

[18] R. W. Overholser, M. Wuttig, and D. A. Neumann. Chemical ordering in Ni–Mn–Ga Heusler alloys. *Scripta Mater.*, 40:1095–1102, 1999.

[19] S. Wirth, A. Leithe-Jasper, A. N. Vasil'ev, and J. M. D. Coey. Structural and magnetic properties of $\mathrm{Ni_2MnGa}$. *J. Magn. Mag. Mat*, 167:L7–L11, 1997.

[20] V. A. Chernenko, A. Amengual, E. Cesari, V. V. Kokorin, and I. K. Zasimchuk. Thermal and magnetic properties of stress-induced martensites in Ni–Mn–Ga alloys. *J. de Physique IV*, 5 (C2):95–98, 1995.

[21] R. C. O'Handley, D. I. Paul, M. A. Marioni, C. P. Henry, M. Richard, P. G. Tello, and S. M. Allen. Field-induced strain in ferromagnetic shape memory actuators: from macroscopic to microscopic models. In *The Fourth Pacific Rim International Conference on Advanced Materials and Processing*, volume PRICM4, pages 2945–2948, 2001.

[22] S. J. Murray, M. A. Marioni, S. M. Allen, R. C. O'Handley, and T. A. Lograsso. 6% magnetic-field-induced strain by twin-boundary motion in ferromagnetic Ni–Mn–Ga. *Appl. Phys. Lett.*, 77:886–888, 2000.

[23] Miguel A Marioni. *Pulsed magnetic field-induced twin boundary motion on Ni-Mn-Ga*. PhD thesis, Massachusetts Institute of Technology, Cambridge, MA, May 2003.

[24] R. C. O'Handley. Model for strain and magnetization in magnetic shape-memory alloys. *J. Appl. Phys.*, 83:3263–3270, 1998.

[25] J. P. Teter, M. Wunfogle, A. E. Clark, and K. Mahoney. Anisotropic perpendicular axis magnetostriction in twinned $\mathrm{Tb}_x\mathrm{Dy}_{1-x}\mathrm{Fe}_{1.95}$. *Journal of Applied Physics*, 67(9):5004–5006, May 1990.

[26] A. E. Clark J. P. Teter, K. B. Hathaway. Zero field damping capacity in $(\mathrm{Tb}_x\mathrm{Dy}_{1-x})\mathrm{Fe}_y$. *Journal of Applied Physics*, 79(8):6213–6215, April 1996.

[27] K. B. Hathaway, A. E. Clark, and J. P. Teter. Magnetomechanical damping in giant magnetostriction alloys. *Metallurgical and materials transactions A-physical metallurgy and materials science*, 26(11):2797–2801, November 1995.

[28] T. A. Duenas and G.P. Carman. Large magnetostrictive response of Terfenol-D resin composites (invited). *Journal of Applied Physics*, 87(9):4696–4701, May 2000.

[29] Hideki Hosoda, Shinsuke Takeuchi, Tomonari Inamura, Kenji Wakashima, and Shuichi Miyazaki. Shape memory behavior of NiMnGa/epoxy smart composites. *Materials Science Forum*, 475-479:2067–2070, 2005.

[30] Hideki Hosoda, Shinsuke Takeuchib andTomonari Inamura, and Kenji Wakashima. Material design and shape memory properties of smart composites. *Science and Technology of Advanced Materials*, 5:503–509, May 2004.

[31] Hideki Hosoda, Shinsuke Takeuchi, Kenji Wakashima, and Shuichi Miyazaki. Fabrication of shape memory alloy powder/polymer smart composites. *Transactions of the materials research society of japan*, 28(3):647–650, march 2003.

[32] P. Wright and A. P. C. Cumming. *Solid Polyurethane Elastomers*. Gordon and Breach Science Publishers, New York, 1969.

[33] Bernard A. Dombrow. *Polyurethanes*. Reinhold Plastics Applications Series, New York, second edition, 1965.

[34] Roderic S. Lakes. *Viscoelastic Solids*. CRC Press, Boca Raton, Florida, 1999.

[35] David K. Roylance. Modules in mechanics of materials: Engineering viscoelasticity. October 2001.

[36] Eric Gans, Chris Henry, and Gregory P. Carman. High-energy absorption in bulk ferromagnetic shape memory alloys ($Ni_{50}Mn_{29}Ga_{21}$). In Dimitris C. Lagoudas, editor, *Proceedings of SPIE Smart Structures and Materials 2004: Active Materials: Behavior and Mechanics*, volume 5387, pages 177–185, July 2004.

[37] V. Novakc O. Heczko S.-P. Hannula V.K. Lindroos O. Soderberg, L. Straka. Tensile/compressive behaviour of non-layered tetragonal $\mathrm{Ni_{52.8}Mn_{25.7}Ga_{21.5}}alloy$. *Materials Science and Engineering A*, 386:27–33, 2004.

[38] David A. Ruggles, Eric Gansa, K. P. Mohanchandraa, Greg P. Carmana, E. Ngob, W. Nothwangb, and M. W. Cole. Damping of polycrystalline ni-mn-ga, bulk, pld, and sputtered thin film. In Dimitris C. Lagoudas, editor, *Proceedings of SPIE Smart Structures and Materials 2004: Active Materials: Behavior and Mechanics*, volume 5387, pages 156–163, Bellingham, WA, 2004), 2004. SPIE.

[39] J. Feuchtwanger, S. Michael, J. K. Huang, D. Bono, R. C. O'Handley, S. M. Allen, K. Jenkins, J. Goldie, and A. Berkowitz. Energy absorption in Ni–Mn–Ga polymer composites. *J. Appl. Phys.*, 93(10):in press, 2003.

[40] J. Feuchtwanger, K. Griffin, J. K. Huang, R. C. O'Handley, S. M. Allen, and D. Bono. Vibration damping in Ni–Mn–Ga-polymer composites. In *Smart Structures and Materials*, volume Proceedings of SPIE SS/NDA, page in press, 2003.

[41] J. Feuchtwanger, K. Griffin, J. K. Huang, D. Bono, R. C. O'Handley, and S. M. Allen. Mechanical energy absorption in Ni–Mn–Ga polymer composites. *J. Magn. Magn. Mat.*, 272-276(3):2038–2039, May 2004.

[42] Jorge Feuchtwanger, Marc L. Richard, Yun J. Tang, Ami E. Berkowitz, Robert C. O'Handley, and Samuel M. Allen. Large energy absorption in Ni–Mn–Ga/polymer composites. *J. Appl. Phys.*, 97(10M329), May 2005.

[43] J. Carrey, H. B. Radousky, and A. E. Berkowitz. Spark-eroded particles: Influence of processing parameters. *Journal of Applied Physics*, 95(3):823–829, February 2004.

[44] A.E. Berkowitz, M.F. Hansen, F.T. Parker, K.S. Vecchio, F.E. Spada, E.J. Lavernia, and R. Rodriguez. Amorphous soft magnetic particles produced by spark erosion. *Journal of Magnetism and Magnetic Materials*, 254(1-6 Sp. Iss. SI):January, 2003.

[45] G. P. McKnight and G. P. Carman. Energy absorption and damping in magnetostrictive composites. *Mat. Res. Soc. Symp Proc.*, 604:267–272, 2000.

[46] P. Muellner, V.A. Chernenko, M. Wollgarten, and G. Kostorz. Large cyclic deformation of a Ni–Mn–Ga shape memory alloy induced. *J. Appl. Phys.*, 92(11):6708–6713, December 2002.

[47] Ladislav Straka and Oleg Heczko. Magnetic anisotropy in Ni–Mn–Ga martensites. *Journal of Applied Physics*, 93(10):8636–8639, May 2003.

[48] Oleg Heczko and Ladislav Straka. Compositional dependence of structure, magnetization and magnetic anisotropy in Ni–Mn–Ga magnetic shape memory alloys. *Journal of Magnetism and Magnetic Materials*, 272-276:2045–2046, 2004.

[49] O. Hezcko. Private communication. 2005.

[50] David C. Bono. Private communication (co-founder of dms inc.), 2005.

[51] Virgil C. Solomon, Martha R. McCartney, and David J. Smith. Magnetic domain configurations in spark-eroded ferromagnetic shape memory ni-mn-ga particles. *Applied Physics Letters*, 86:192503, may 2005.

[52] Virgil C. Solomon, David J. Smith, YunJun Tang, Ami E. Berkowitz, and Robert C. O'Handley. Magnetic domain configurations in spark-eroded ferromagnetic shape memory alloy powders. *Journal of Applied Physics*, 95(11):9654–9656, January 2004.

[53] J. Pons, V. A. Chernenko, R. Santamarta, and E. Cesari. Crystal structure of martensitic phases in Ni–Mn–Ga shape memory alloys. *Acta Mater.*, 48:3027–3038, 2000.

[54] E. Cesari, V. A. Chernenko, V. V. Kokorin, J. Pons, and C. Seguí. Internal friction associated with the structural phase transformations in Ni–Mn–Ga alloys. *Acta Mater.*, 45:999–1004, 1997.

[55] David R. Lide, editor. *CRC Handbook of Chemistry and Physics.* CRC Press, LLC, 85th. edition, 2004.

[56] Walter D. Pilkey. *Peterson's stress concentration factors*. McGraw-Hill, 1997.

[57] Z.M Peng, X.J. Jin, Y.Z. Fan, Y.T. Hsu nd S.M. Allen, and R. C. O'Handley. Internal friction and modulus changes associated with martensitic and reverse transformations in a single crystal $\mathrm{Ni}_{48.5}\mathrm{Mn}_{31.4}\mathrm{Ga}_{20.1}$ alloy. *Journal of Applied Physics*, 95(11):6960–6962, June 2004.

[58] J. D. Eshelby. The determination of the elastic field of an ellipsoidal inclusion, and related problems. *Proceedings of the Royal Society of London, Series A*, 241(1226):376–396, August 1957.

[59] Janes E. Martin, Robert A. Anderson, and Rodney L. Williamson. Generating strange magnetic and dielectric interactions:classical molecules and particle foams. *Journal of Chemical Physics*, 118(3):1557–1571, January 2003.